The Normal Parameterization and its Application to Collision Detection

Ulrich J. Römer[a,*], Alexander Fidlin[a], Wolfgang Seemann[a]

[a] *Institute of Engineering Mechanics, Karlsruhe Institute of Technology, Kaiserstraße 10, 76131 Karlsruhe, Germany*

Abstract

Collision detection is a central task in the simulation of multibody systems. Depending on the description of the geometry, there are many efficient algorithms to address this need. A widespread approach is the common normal concept: potential contact points on opposing surfaces have antiparallel normal vectors. However, this approach leads to implicit equations that require iterative solutions when the geometries are described by implicit functions or the common parameterizations. We introduce the normal parameterization to describe the boundary of a strictly convex object as a function of the orientation of its normal vector. This parameterization depends on a scalar function, the so-called generating potential from which all properties are derived: points on the boundary, continuity/differentiability of the boundary, curvature, offset curves or surfaces. An explicit solution for collisions with a planar counterpart is derived and four iterative algorithms for collision detection between two arbitrary objects with the normal parametrization are compared. The application of this approach for collision detection in multibody models is illustrated in a case study with two ellipsoids and several planes.

Keywords: Collision detection, Contact kinematics, Geometry parameterization, Common normal concept, Offset curve/surface, Superellipsoid, Superquadric

1. Introduction

The representation of three-dimensional objects is required in many disciplines, such as computer graphics, computer vision, computer aided design (CAD) and the modeling of many physical systems. Because of the wide and diverse range of applications, there is no single representation of three-dimensional objects that meets the requirements of every problem. Therefore, depending on the respective representation, there are different approaches for collision detection—a central task in the simulation of mechanical systems with considerable influence on computation times and memory requirements.

Mathematical representations of three-dimensional objects can be categorized in two different ways [1, 2]: either volume-based vs. surface-based approaches or explicit parameterizations vs. implicit definitions. An object is a connected set $\Omega \subset \mathbb{R}^3$ with the boundary $\partial\Omega$. Volume-based approaches construct Ω via Boolean operations (union, intersection, and difference) from basic geometries (e.g. cuboids, quadrics, prisms, sweeps, etc.), whereas surface-based approaches construct $\partial\Omega$ as a union of independently constructed surface patches. Volume-based descriptions are widely used in CAD applications where gapless or overlap-free boundaries are required. Meanwhile, surface-based approaches are popular in computer graphics applications because of their greater flexibility [3]. Both approaches require representations of the respective elementary components either by means of explicit parameterizations (e.g. splines, NURBS, meshes) or by implicit definitions (level sets). Some basic geometries such as ellipsoids, superquadrics [4], superellipsoids [5] and superovoids [6] can be converted from an explicit parameterization to an implicit definition and vice versa—this is, however, not possible in general[1].

*Corresponding author

Email addresses: ulrich.roemer@kit.edu (Ulrich J. Römer), alexander.fidlin@kit.edu (Alexander Fidlin), wolfgang.seemann@kit.edu (Wolfgang Seemann)

[1] There is ongoing research regarding the problems of uniformization (finding a parameterization for an implicit representation) and implicitization (finding an implicit representation for a given parameterization). Existing approaches are limited to certain parameterizations [7, 8].

The suitability of different geometry representations for use in simulation models with multiple objects and possible collisions among them depends on the requirements and objectives of the respective task. In this context, considerable consequences result from the question of whether any object is modeled as elastic or all of them are rigid. Elastic objects are usually treated using finite element analysis (FEA), where the discretization of an object's volume naturally provides a mesh representation for its surface. Contact treatment has a long history in FEA [9], the current state of the art being mortar-based contact formulations [10]. For more details we refer to [11, Chapters 8–10]. An extensive literature review on contact treatment is given in [12]. Furthermore, recent advances in this area include improved geometry representation by isogeometric analysis (IGA) [13, 14] and its application to contact simulations [15]. Finite element models for elastic objects usually result in a large number of degrees of freedom which are required to achieve a desired accuracy; this is all the more true when contacts are involved and which may require strategies such as adaptive mesh refinement in the areas where contacts occur [16, 17]. The field of flexible multibody dynamics is concerned with the investigation of the dynamics of systems with several such elastic objects [18, 19, 20]. Since the objects' geometry representation is based on the requirements of the finite element models and an extension of the isogeometric analysis approach is very extensive, elastic objects are not further elaborated in the present manuscript.

On the other hand, rigid objects and contacts between them have been considered from the very beginning in the areas of multibody dynamics [21] and the Discrete Element Method (DEM) [22]. In this context, the task of collision detection requires the efficient identification of contacts between any two objects. Subsequently, interaction forces are introduced to prevent the objects from interpenetrating each other in the normal direction and to account for other interactions such as friction in the tangential direction. Meshes such as polyhedra can be used to approximate rigid objects and efficient collision detection algorithms exist for this description [23, 24, 25, 26, 27, 28]. However, since this approach is based on piecewise straight lines and flat surface patches, it usually requires a large number of vertices to achieve a good approximation to smooth surfaces. Therefore, high-resolution meshes require a lot of memory and lead to slow collision detection performance. Because of these limitations, this approach is not considered suitable for applications such as real-time models for control purposes or large discrete element models (DEM) [29].

One approach to improve calculation times and memory requirements is not to use polyhedra but smooth parametric surfaces, which are discretized in a pre-processing step [30]. An error-controlled discretization results in a minimum number of interpolation points between which a fast approximation of the smooth surface by interpolation is possible. These interpolation points are stored in lookup tables, which can be partially loaded into memory as required [31]. The lookup tables contain not only interpolation values for the surface, but also for the normal and tangential directions. Fast simulations and real-time applications are possible, but the necessary pre-processing calculations can be significant. An alternative approach is the approximation of object geometries by superquadrics [4], superellipsoids [5] or superovoids [6]. This can be realized either by a union of several of these simple objects [6] or by a piecewise approximation of the object's surface via patches of their boundary [32, 33]. Collision detection between smooth, rigid objects is usually performed based on the common normal concept: (potential) contact points on the opposite boundaries of two objects have antiparallel outer normal vectors. This problem is easy to solve for the collision detection between two spheres. However, so far there are no explicit solutions even for the collision detection problem with two ellipsoids [34, 35, 36]. The determination of such points during simulations therefore requires the iterative solution of implicit relations for most surfaces which is computationally more expensive and time consuming. Common algorithms are based on Newton-type methods with analytical Jacobians, which are cumbersome to implement for every combination of different objects[4, 5, 6]. To increase performance, currently proposed approaches [28] use a combination of several algorithms, first checking whether there is a collision (e.g. by using the GJK algorithm [23]) and then determining the common normal for these cases, which is needed for subsequent calculation of the interaction forces.

Solid objects cannot penetrate each other, which is ensured by an interaction force in the direction of the common normal at the contact point. In addition, DEM or multibody models usually consider friction forces that are perpendicular to the common normal in the respective tangent plane. Both normal and friction forces are associated with unilateral constraints. When formulating the system dynamics, these constraints can be met either exactly or via penalty terms that depend on (small) violations of the constraints. The first approach is pursued in the area of nonsmooth dynamics and leads to complementarity problems [37]. In the latter, the penalty terms are usually physically motivated. In this context, Hertzian contact theory [38] can be understood as a penalty method for satisfying the non-penetration condition: by assuming that the objects are elastic after all, but that significant deformations occur

only in a small vicinity around the points of initial contact, a force-displacement relationship is determined based on elastic half spaces [39]. This yields the behavior of a non-linear spring which, depending on the principal curvatures of the two surfaces at the points of maximum penetration[2], generates a restoring force which opposes the penetration of the undeformed object geometries. There are numerous extensions of this model where both dissipative effects due to local material deformation [40, 41, 42, 43, 44, 45, 46][3] and forces due to friction [49, 50, 51, 52, 53] are added. All these approaches require the common normal and the maximum penetration depth to determine the interaction forces. Given the common normal, an orthonormal basis for the tangent plane which is required when friction is present can be calculated, e.g. using the Householder transformation [4, 6].

For smooth objects, the common normal concept for collision detection already provides the common normal and thus allows easy calculation of all quantities required to determine the interaction forces. However, the solution of the collision detection problem is complex, since there are no explicit solutions even for collisions between objects with simple geometry [34, 35, 36]. Geometry representation by implicit functions already requires the iterative solutions to determine points on the object boundary. When using a parametric representation, all points on the surface and also the corresponding normal can be determined explicitly as functions of two coordinates. However, the inverse problem, i.e. determining the coordinates and the corresponding surface points for a given normal direction, can again only be solved implicitly if the usual parameterizations are used. As a result, the dynamics of such systems with rigid objects cannot be formulated in a set of minimum coordinates, because the implicit constraint equations cannot be eliminated, making it very difficult, if not impossible, to analytically study such models.

The aim of the present manuscript is to contribute to an improvement in the use of the common normal concept through a novel representation of three-dimensional objects: the *normal parameterization*. This approach is a generalization and simplification of the method the authors introduced in [54] for two-dimensional objects. It results in a parameterization of object boundaries as a function of the outer normal direction and is thus limited to strictly convex objects with a unique boundary point for any outer normal direction. In spite of this restriction, there are many possible applications for this representation such as granular particles in DEM-models [55], bounding volumes in robotic applications [56], rigid foot models in biomechanics and robotics [57, 58], or general models of rigid bodies as unions of strictly convex objects. For arbitrary, strictly convex geometries, the normal parameterization provides an explicit solution to the collision detection problem when the counterpart is a plane. For collision detection between two such objects, an iterative solution is still necessary, but due to the properties of the normal parameterization, it does not require a combination of several algorithms or a cumbersome implementation of analytical Jacobians. In addition, the normal parameterization allows a simple calculation of offset curves and surfaces for any such object. The focus of this manuscript is on the derivation of the normal parameterization and its properties (such as continuity/differentiability). A collision detection algorithm which is based on the common normal concept and does not require any derivatives is proposed and compared to approaches based on Newton methods with analytic Jacobians in terms of convergence and robustness. Its application for collision detection and the calculation of interaction forces is demonstrated in a case study with two ellipsoids and five planes. A computationally efficient implementation in an existing multibody or DEM software framework—or even a benchmark study as performed in [6]—are beyond the scope of the present manuscript and remain for future work.

The remainder of this paper is organized as follows. The general expressions and relationships of the normal parameterization for two- and three-dimensional objects are introduced in Sections 2 and 3, respectively. The derivation of the normal parameterization from basic principles of rigid body kinematics is presented in Section 4. Four algorithms for collision detection based on the common normal concept are introduced and compared in Section 5. The application in a multibody simulation is illustrated by a case study in Section 6. The capabilities and limitations of the normal parameterization and propositions for future work are discussed in Section 7. A summary and a conclusion are given in Section 8. Clarifications regarding the notation are summarized in Appendix A.

[2] Hertzian contact theory considers two elastic half-spaces that come into contact at one point in the undeformed state during contact initiation (non-conformal contact) [39, Chapter 4]. As the two half spaces are pressed together in the normal direction, elastic deformation takes place. The undeformed geometries penetrate each other, the initial contact points then being the points of maximum penetration.

[3] Since most of these approaches are based on Hertzian contact theory, their validity is based on the assumption of non-conformal contacts with small deformations; if this is not the case, parameters must be adjusted [47] or a different approach is required [48].

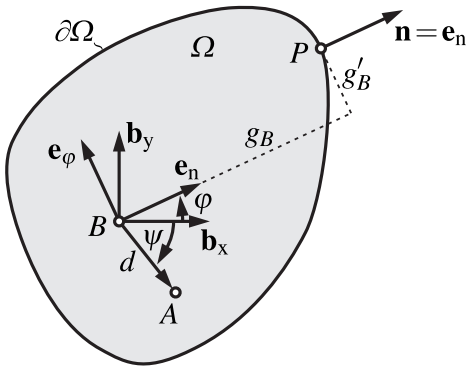

Figure 1: Normal parameterization of a strictly convex two-dimensional object Ω. Any point $P \in \partial\Omega$ is given by the generating potential g_B via Eq. (2) as a function of φ—the direction of the outer normal vector $\mathbf{n}$ at P in polar coordinates.

2. Normal parameterization for two-dimensional objects

The basic concept of the normal parameterization for two-dimensional objects is derived by the authors in [54]. Below, it is recapitulated, extended and summarized in a clearer and more precise form. The key idea is to find a parameterization of the boundary of a strictly convex object as a function of its outer normal vector's orientation. Since the object is strictly convex, there is a unique point on the boundary for any given normal direction. The continuity and curvature of the boundary are investigated and illustrated by selected examples. Based on these relationships, the normal parameterization is then generalized for three-dimensional objects in Section 3.

A strictly convex two-dimensional object as depicted in Fig. 1 is represented by a closed set $\Omega \subset \mathbb{R}^2$ which is identical to its convex hull: $\Omega = \mathrm{conv}(\Omega)$. The normal parameterization uses an arbitrary body-fixed reference point $B \in \mathbb{R}^2$ to describe any point $P \in \partial\Omega$ on the boundary $\partial\Omega = \mathrm{cl}(\Omega)$ as a function of the orientation of its outer normal vector $\mathbf{n} = \mathbf{e}_\mathrm{n}$ in the following way.

Proposition 1. Let $\Omega \subset \mathbb{R}^2$, $\Omega = \mathrm{conv}(\Omega)$ with boundary $\partial\Omega = \mathrm{cl}(\Omega)$. Introduce the body-fixed, orthonormal frame $\mathcal{B} = \{B, (\mathbf{b}_\mathrm{x}, \mathbf{b}_\mathrm{y})\}$ and a rotating orthonormal frame $\mathcal{E} = \{B, (\mathbf{e}_\mathrm{n}, \mathbf{e}_\varphi)\}$ with

$$\mathbf{e}_\mathrm{n} = \quad \cos\varphi\, \mathbf{b}_\mathrm{x} + \sin\varphi\, \mathbf{b}_\mathrm{y}\,, \tag{1a}$$

$$\mathbf{e}_\varphi = -\sin\varphi\, \mathbf{b}_\mathrm{x} + \cos\varphi\, \mathbf{b}_\mathrm{y}\,, \tag{1b}$$

cf. Fig. 1. Let the *generating potential for point B* $g_B : \mathbb{S}^1 \to \mathbb{R}, \varphi \mapsto g_B(\varphi)$ with $g_B \in C^k, k \geq 1$. Under these assumptions, the following statements are valid: the *normal parameterization* of $\partial\Omega$ relative to B as a function of the outer normal direction given by the angle φ is

$$\begin{aligned}\mathbf{r}_{BP}(\varphi) &= g_B(\varphi)\mathbf{e}_\mathrm{n} + g'_B(\varphi)\mathbf{e}_\varphi \\ &= \left(\cos\varphi\, g_B(\varphi) - \sin\varphi\, g'_B(\varphi)\right)\mathbf{b}_\mathrm{x} + \left(\sin\varphi\, g_B(\varphi) + \cos\varphi\, g'_B(\varphi)\right)\mathbf{b}_\mathrm{y}\end{aligned} \tag{2}$$

and the boundary's smoothness in terms of the geometric continuity is

(i) $\partial\Omega \in G^0$ if $g_B \in C^k, k \geq 1$;

(ii) $\partial\Omega \in G^1$ if $\partial\Omega \in G^0$, $g_B \in C^k, k \geq 2$ and

$$0 < g_B(\varphi) + g''_B(\varphi) \tag{3}$$

for all $\varphi \in \mathbb{S}$;

(iii) $\partial\Omega \in G^2$ if $\partial\Omega \in G^1$.

A derivation of Eq. (2) is given in [54]. Before we continue with the proof of Proposition 1, we take a closer look at the boundary's curvature and geometric continuity. Consider the following relationships. Let $g_B \in C^k, k \geq 1$ and $\mathbf{n}(\varphi) = \mathbf{e}_\mathrm{n}$, then Eq. (1a) directly yields the differential

$$\mathrm{d}\mathbf{n} = \frac{\partial \mathbf{e}_\mathrm{n}}{\partial \varphi}\,\mathrm{d}\varphi = \mathrm{d}\varphi\,\mathbf{e}_\varphi \tag{4}$$

which is perpendicular to the normal direction $\mathrm{d}\mathbf{n} \perp \mathbf{e}_\mathrm{n}$. Let $g_B \in C^k, k \geq 2$, then Eq. (2) directly yields the differential

$$\mathrm{d}\mathbf{r} = \frac{\partial \mathbf{r}_{BP}}{\partial \varphi}\,\mathrm{d}\varphi = \left(g_B(\varphi) + g_B''(\varphi)\right)\mathrm{d}\varphi\,\mathbf{e}_\varphi \tag{5}$$

which is perpendicular to the normal direction $\mathrm{d}\mathbf{r} \perp \mathbf{e}_\mathrm{n}$. Let $\mathrm{d}s = \sqrt{\mathrm{d}\mathbf{r}\cdot\mathrm{d}\mathbf{r}}$, then $s = \int \mathrm{d}s$ is the arc length of the curve which represents the boundary $\partial\Omega$. A unit tangent vector is given by $\mathbf{t} = \mathrm{d}\mathbf{r}/\mathrm{d}s = \mathbf{e}_\varphi$ and the curvature is determined by the following corollary.

Corollary 2. Let $g_B \in C^k, k \geq 2$, then the boundary's *curvature* is

$$\kappa(\varphi) = \left(g_B(\varphi) + g_B''(\varphi)\right)^{-1} \tag{6}$$

and the corresponding *curvature radius* is

$$R(\varphi) = \kappa^{-1}(\varphi) = g_B(\varphi) + g_B''(\varphi)\,. \tag{7}$$

Proof. By definition, the curvature is[4] $\mathrm{d}\mathbf{t}/\mathrm{d}s = -\kappa\,\mathbf{n} \Rightarrow \kappa = -\,\mathrm{d}\mathbf{t}/\mathrm{d}s \cdot \mathbf{n}$ and the corresponding curvature radius is $R = \kappa^{-1}$. Since $\mathbf{n}\cdot\mathbf{t} = 0$, this is equal to $\kappa(\varphi) = (\mathrm{d}\mathbf{r}/\mathrm{d}s)\cdot(\mathrm{d}\mathbf{n}/\mathrm{d}s) = (\mathrm{d}\mathbf{r}\cdot\mathrm{d}\mathbf{n})/(\mathrm{d}\mathbf{r}\cdot\mathrm{d}\mathbf{r}) = (g_B(\varphi) + g_B''(\varphi))^{-1}$. □

Remark 3. If $g_B \in C^k, k \geq 2$, then $\kappa(\varphi) > 0$ for all $\varphi \in \mathbb{S}^1$ is the necessary and sufficient condition for strict convexity of the boundary. $\kappa \neq 0$ implies that any set of three infinitesimally neighboring points on the boundary does not lie on a common straight line, since the radius of the osculating circle $R = \kappa^{-1}$ is finite everywhere. Since $\kappa > 0 \Rightarrow R > 0$, the center of the osculating circle is in direction of the inner normal. Therefore, all neighbors of any point $P \in \partial\Omega$ lie on the inner side (given by the direction $-\mathbf{n}$) of the tangent line at P.

The geometric continuity $G^k, k \geq 0$ of a curve is an invariant geometric property which is independent of any specific parameterization. Geometric continuity is of special interest for piecewise descriptions of curves via splines, B-splines, NURBS, etc. [59]. In the treatment of piecewise descriptions where a curve is constructed by connecting several curve segments, it is often presumed that k-th order parametric continuity C^k implies k-th order geometric continuity G^k within any segment and the focus is therefore on the transition points between the segments. This is not true for the normal parameterization, where it is easily possible to construct a C^ω parameterization[5] which is only G^0 continuous, cf. Example 4.

In this context, a plane curve $\mathbf{c} = x\,\mathbf{b}_\mathrm{x} + y\,\mathbf{b}_\mathrm{y}$ is said to be G^0-continuous iff there exists a C^0-continuous parameterization $\mathbf{c}(t) = x(t)\mathbf{b}_\mathrm{x} + y(t)\mathbf{b}_\mathrm{y}$ of the curve [59]. It is G^1-continuous iff there is a C^1-continuous parameterization $\mathbf{c}(t) = x(t)\mathbf{b}_\mathrm{x} + y(t)\mathbf{b}_\mathrm{y}$ of the curve with unit tangent vector $\mathbf{t}(t) \in C^0$. Without loss of generality use the arc length parameterization $t = s$ to see that this means that the tangent direction which is given by the unit tangent vector $\mathbf{t}(s)$ at any point $\mathbf{c}(s)$ is changing continuously between any two neighboring points on the curve. G^2 continuity makes the same demands on the curvature vector $\mathrm{d}\mathbf{t}/\mathrm{d}s \in C^0$. The peculiarities of the normal parameterization are best illustrated by an example.

Example 4. The general potential $g_B(\varphi)$ for the object in Fig. 2 is given by[6]

$$g_B(\varphi) = \sqrt{a^2\cos^2\varphi + b^2\sin^2\varphi} - \frac{b^2}{a} \tag{8}$$

[4] The negative sign in this definition is due to $\mathbf{n}$ being the outer normal vector. By this definition the center of the osculating circle is in direction of the inner normal vector $-\mathbf{n}$.

[5] C^ω means the parameterization is analytic.

[6] Equation (8) as the generating potential for a boundary curve which is equidistant to an ellipse follows from Eqs. (12) and (11) which are derived below.

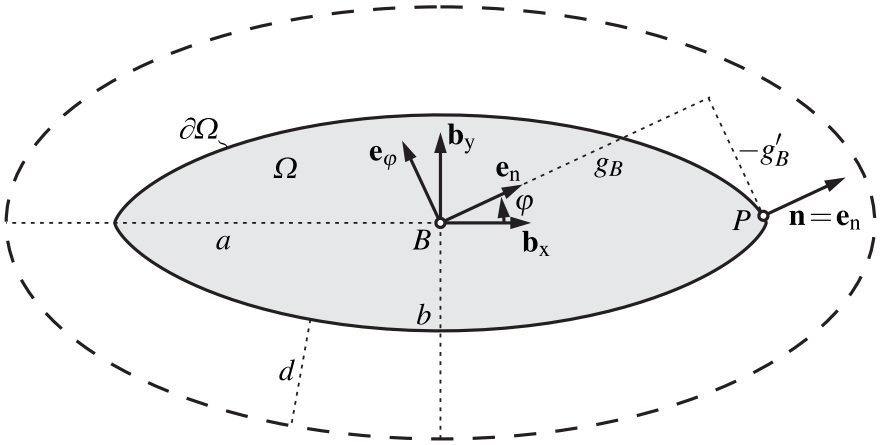

Figure 2: Normal parameterization of an object Ω with generating potential via Eq. (8) with $b/a = 1/2$. The boundary $\partial\Omega \in G^0$ has two kinks at $\varphi = 0$ and $\varphi = \pi$ and is equidistant (with distance $d = -b^2/a$) to an ellipse with semi-axes a, b (thick dashed line).

with $a, b \in \mathbb{R}$ and $a > b > 0$. The associated boundary curve $\partial\Omega$ is continuous, therefore $\partial\Omega \in G^0$. However $\partial\Omega \notin G^1$, although the generating potential is analytic $g_B \in C^\omega$. The depiction of this object shows two kinks in the boundary at $\varphi \in \{0, \pi\}$. Indeed, the curvature radius via Eq. (7) vanishes at those points

$$R(0) = R(\pi) = 0 \,. \tag{9}$$

The osculating circle with radius R touches the boundary curve in (at least) three infinitesimally neighboring points. This means the unit tangent vector $\mathbf{t}$ which touches the curve in two neighboring points changes its orientation by a finite angle although there is only an infinitesimal change in the arc length s when passing through one of these points.

This example shows that k-th order parametric continuity of $\mathbf{r}_{BP} \in C^k$ is not sufficient for k-th order geometric continuity of the boundary G^k. If there is any point $P(\varphi^*) \in \partial\Omega$ with $g_B(\varphi^*) + g''_B(\varphi^*) = 0$, the unit tangent vector $\mathbf{t}$ does not change continuously with the arc length s and $\partial\Omega \notin G^1$.

An equivalent statement can be obtained by studying the change of the normal vector $\mathbf{n}$. This is more consistent with the idea of the normal parameterization. Since $\mathbf{n} \perp \mathbf{t}$, the necessary and sufficient condition for G^1 continuity is that the normal vector at every point $P \in \partial\Omega$ is unique, which means $\mathrm{d}s(\mathrm{d}\varphi \neq 0) \neq 0$ or, equivalently, that $\mathrm{d}s^2 = \mathrm{d}\mathbf{r}\cdot\mathrm{d}\mathbf{r}$ is positive definite with respect to $\mathrm{d}\varphi$.

Proof of Proposition 1. Since $\mathrm{d}\mathbf{r} \perp \mathbf{e}_\mathrm{n}$ via Eq. (5), the normal parameterization via Eq. (2) indeed describes the boundary $\partial\Omega$ as a function of the outer normal direction $\varphi \mapsto \mathbf{n}(\varphi) = \mathbf{e}_\mathrm{n}$. The propositions with regard to the boundary's geometric continuity can be shown as follows:

(i) Since Eq. (2) directly yields $\mathbf{r}_{BP} \cdot \mathbf{b}_\mathrm{x} = (\cos\varphi\, g_B(\varphi) - \sin\varphi\, g'_B(\varphi))$ and $\mathbf{r}_{BP} \cdot \mathbf{b}_\mathrm{y} = (\sin\varphi\, g_B(\varphi) + \cos\varphi\, g'_B(\varphi))$, the boundary is continuous iff both g_B and g'_B are continuous. Therefore, $\partial\Omega \in G^0$ if $g_B \in C^k, k \geq 1$.

(ii) As shown with Example 4, $g_B(\varphi) + g''_B(\varphi) \neq 0$ for all $\varphi \in \mathbb{S}^2$ is a necessary condition for G^1 continuity. Since convexity of Ω requires the curvature radius via Eq. (7) to be non-negative, $R = g_B + g''_B \geq 0$ for all $\varphi \in \mathbb{S}$ is a sufficient condition. Therefore, $g_B(\varphi) + g''_B(\varphi) > 0$ for all $\varphi \in \mathbb{S}$ is necessary and sufficient for $\partial\Omega \in G^1$.

(iii) Let $\partial\Omega \in G^1$, then the curvature radius $R = \kappa^{-1}$ is the sum of g_B and g''_B. The curvature radius, and thus also the curvature vector, are continuous iff both g_B and g''_B are continuous. Since $\partial\Omega \in G^1$ implies $g_B \in C^k, k \geq 2$ and $\kappa > 0$, $\partial\Omega \in G^2$ if $\partial\Omega \in G^1$. □

Corollary 5. Given g_B, the generating potential for a different body-fixed point A at $\mathbf{r}_{BA} = d\cos\psi\,\mathbf{b}_\mathrm{x} - d\sin\psi\,\mathbf{b}_\mathrm{y}$, cf. Fig. 1, is

$$g_A(\varphi) = g_B(\varphi) - d\cos(\varphi + \psi) \,. \tag{10}$$

Proof. This relationship follows directly from $\mathbf{r}_{AP} = \mathbf{r}_{BP} - \mathbf{r}_{BA}$ and Eq. (2). □

Remark 6. Points $A, B \in \mathbb{R}^2$ are not required to be elements of Ω, as Eq. (10) is valid for all $d \in \mathbb{R}, \psi \in \mathbb{S}$. If $B \notin \Omega$, then $\min_\varphi g_B(\varphi) < 0$ as is evident from Fig. 1.

Corollary 7. Given the generating potential g_B and the associated normal parameterization of a boundary curve $\partial\Omega$, an equidistant curve $\partial\bar{\Omega}$ with distance d is given by the generating potential

$$\bar{g}_B(\varphi) = g_B(\varphi) + d \,. \tag{11}$$

Proof. This relationship follows directly from

$$\begin{aligned}\mathbf{r}_{B\bar{P}}(\varphi) &= \mathbf{r}_{BP}(\varphi) + d\,\mathbf{e}_\mathrm{n} \\ &= (g_B(\varphi) + d)\,\mathbf{e}_\mathrm{n} + g'_B(\varphi)\mathbf{e}_\varphi \\ &= \bar{g}_B(\varphi)\mathbf{e}_\mathrm{n} + \bar{g}'_B(\varphi)\mathbf{e}_\varphi\end{aligned}$$

where $\mathbf{r}_{B\bar{P}}(\varphi)$ is a normal parameterization for any point $\bar{P} \in \partial\bar{\Omega}$ with outer normal vector $\mathbf{n} = \mathbf{e}_\mathrm{n}$. □

Remark 8. The curvature radius $\bar{R}$ at any point $\bar{P}(\varphi^*) \in \partial\bar{\Omega}$ is equal to the curvature radius R of the original curve at the point with $P(\varphi^*) \in \partial\Omega$ the same outer normal vector $\bar{R}(\varphi) = R(\varphi) + d$. The proof of this relationship follows directly from Eq. (7). If the distance d of the equidistant curve $\partial\bar{\Omega}$ is negative, the offset is in direction of the inner normal vector $-\mathbf{n}$. If this distance is equal to the minimal curvature radius $d = -\min_{\varphi\in\mathbb{S}} R(\varphi)$, the resulting curve $\partial\bar{\Omega}$ has at least one point with vanishing curvature radius $\min_{\varphi\in\mathbb{S}} \bar{R}(\varphi) = 0$ and $\partial\bar{\Omega} \notin G^1$. A further decrease of the distance $d < -\min_{\varphi\in\mathbb{S}} R(\varphi)$ results in self-intersections of the boundary curve $\partial\bar{\Omega}$ and violates the convexity assumption $\Omega = \mathrm{conv}(\Omega)$. This case, although certainly of interest for some applications, will not be further elaborated here. The general problem of equidistant offset curves has been studied for several decades [60, 61, 62]. To study if and how the normal parameterization contributes to the solution of this problem is beyond the scope of the present manuscript.

The specific definition of the generating potential g_B is the core requirement for using the normal parameterization. In principle, any 2π-periodic function which satisfies all of the requirements above can be used to define arbitrary strictly convex objects. To determine the generating potential for a given geometry, we propose two approaches which both result in differential equations for g_B: either starting with a different parameterization and comparing coefficients with Eq. (2), or starting with an implicit definition $F(x, y) = 0$ of the boundary $\partial\Omega$ and substituting Eq. (2). However, solving the resulting differential equations is not easy as illustrated by the following example.

Example 9. Take an ellipse with semi-axes a in $\mathbf{b}_\mathrm{x}$- and b in $\mathbf{b}_\mathrm{y}$-direction. Substitution of Eq. (2) into the implicit definition of this ellipse gives the nonlinear differential equation

$$0 = F(x, y) = \left(\frac{x}{a}\right)^2 + \left(\frac{y}{b}\right)^2 - 1 = \left(\frac{\cos\varphi\, g_B(\varphi) - \sin\varphi\, g'_B(\varphi)}{a}\right)^2 + \left(\frac{\sin\varphi\, g_B(\varphi) + \cos\varphi\, g'_B(\varphi)}{b}\right)^2 - 1 \,.$$

Starting from the well known parametric representation of an ellipse and comparing coefficients to Eq. (2) gives the two equations

$$\begin{aligned} x = a\cos t &= \cos\varphi\, g_B(\varphi) - \sin\varphi\, g'_B(\varphi) \,, \\ y = b\sin t &= \sin\varphi\, g_B(\varphi) + \cos\varphi\, g'_B(\varphi) \,. \end{aligned}$$

The solution for the generating potential via either one of these approaches is

$$g_B(\varphi) = \sqrt{a^2\cos^2\varphi + b^2\sin^2\varphi} \,. \tag{12}$$

Remark 10. The generating potential of a superellipse is

$$g_B(\varphi) = \left(\left(a^2\cos^2\varphi\right)^{\frac{\epsilon}{2(\epsilon-1)}} + \left(b^2\sin^2\varphi\right)^{\frac{\epsilon}{2(\epsilon-1)}}\right)^{\frac{\epsilon-1}{\epsilon}} \tag{13}$$

with $\epsilon > 1$. It can be verified by substitution that this satisfies the implicit equation

$$\left(\left(\frac{x}{a}\right)^2\right)^{\frac{\epsilon}{2}} + \left(\left(\frac{z}{c}\right)^2\right)^{\frac{\epsilon}{2}} - 1 = \left(\left(\frac{\mathbf{r}_{BP}\cdot\mathbf{b}_x}{a}\right)^2\right)^{\frac{\epsilon}{2}} + \left(\left(\frac{\mathbf{r}_{BP}\cdot\mathbf{b}_z}{c}\right)^2\right)^{\frac{\epsilon}{2}} - 1 = 0\,.$$

Remark 11. An approximation of any strictly convex geometry is possible by specifying the generating potential g_B by piecewise defined functions like splines or NURBS. Once such a generating potential is specified, the corresponding boundary $\partial\Omega$ follows from Eq. (2). The coefficients of this ansatz can be fitted in such a way that the specified geometry is best approximated by the approach, e.g. by an optimization. The requirement of strict convexity can be checked via the curvature $\kappa > 0$ according to Eq. (6). An example of such a piecewise definition is given in [54, section 6.2] and will not be discussed further in the present manuscript.

3. Normal parameterization for three-dimensional objects

The normal parameterization for three-dimensional objects can be derived in a similar fashion as in the two-dimensional case. Before we proceed, we introduce the class of continuity on the sphere.

Definition 12. Let $f : \mathbb{S}^2 \to \mathbb{R}, (\varphi,\theta) \mapsto f(\varphi,\theta)$ be a mapping from spherical coordinates $\varphi \in [0,\pi]$ and $\theta \in \mathbb{S}^1$ to the real domain. The function f is defined to be of class SC^k if $f \in C^k$ for all $\varphi \in (0,\pi), \theta \in \mathbb{S}^1$ and $f \in C^{k+1}$ for $\varphi \in \{0,\pi\}, \theta \in \mathbb{S}^1$. The class of SC^k is referred to as *continuity on the sphere*.

Continuity on the sphere is equal to parametric continuity C^k in the whole domain of definition $(\varphi,\theta) \in \mathbb{S}^2$, with the additional requirement that the derivatives of order $(k+1)$ exist and are continuous in a neighborhood around the coordinate singularities $\varphi \in \{0,\pi\}$.

Consider now the strictly convex three-dimensional object as displayed in Fig. 3. It is represented by a closed set $\Omega \subset \mathbb{R}^3$ which is identical to its convex hull $\Omega = \mathrm{conv}(\Omega)$. The normal parameterization uses an arbitrary body-fixed reference point $B \in \mathbb{R}^3$ to describe any point $P \in \partial\Omega$ on the boundary $\partial\Omega = \mathrm{cl}(\Omega)$ as a function the orientation of its outer normal vector $\mathbf{n} = \mathbf{e}_n$ in the following way.

Proposition 13. Let $\Omega \subset \mathbb{R}^3$, $\Omega = \mathrm{conv}(\Omega)$ with boundary $\partial\Omega = \mathrm{cl}(\Omega)$. Introduce the body-fixed, orthonormal frame $\mathcal{B} = \{B, (\mathbf{b}_x, \mathbf{b}_y, \mathbf{b}_z)\}$ and a rotating orthonormal frame $\mathcal{E} = \{B, (\mathbf{e}_\varphi, \mathbf{e}_\theta, \mathbf{e}_n)\}$ with

$$\mathbf{e}_\varphi = \cos\varphi\,\cos\theta\,\mathbf{b}_x + \cos\varphi\,\sin\theta\,\mathbf{b}_y - \sin\varphi\,\mathbf{b}_z\,, \tag{14a}$$

$$\mathbf{e}_\theta = \quad -\sin\theta\,\mathbf{b}_x + \quad \cos\theta\,\mathbf{b}_y\,, \tag{14b}$$

$$\mathbf{e}_n = \sin\varphi\,\cos\theta\,\mathbf{b}_x + \sin\varphi\,\sin\theta\,\mathbf{b}_y + \cos\varphi\,\mathbf{b}_z \tag{14c}$$

cf. Fig. 3. The direction of $\mathbf{n}$ is given in spherical coordinates $\mathbf{n} : \mathbb{S}^2 \to \mathbb{R}^3, (\varphi,\theta) \mapsto \mathbf{n}(\varphi,\theta)$ with $\varphi \in [0,\pi]$ and $\theta \in \mathbb{S}^1$. Introduce the *generating potential* $g_B : \mathbb{S}^2 \to \mathbb{R}, (\varphi,\theta) \mapsto g_B(\varphi,\theta)$ with $g_B \in SC^k, k \geq 1$ and

$$\partial_\theta g_B(\varphi,\theta)|_{\varphi\in\{0,\pi\}} = 0 \quad \text{for all} \quad \theta \in \mathbb{S}^1\,. \tag{15}$$

Under these assumptions, the following statements are valid: the *normal parameterization* of $\partial\Omega$ relative to B as a function of the outer normal direction given by (φ,θ) is

$$\mathbf{r}_{BP}(\varphi,\theta) = \begin{cases} \partial_\varphi g_B(\varphi,\theta)\,\mathbf{e}_\varphi + (\sin\varphi)^{-1}\,\partial_\theta g_B(\varphi,\theta)\,\mathbf{e}_\theta + g_B(\varphi,\theta)\,\mathbf{e}_n\,, & \text{if } \varphi \in (0,\pi)\,, \\ \partial_\varphi g_B(\varphi,\theta)\,\mathbf{e}_\varphi + (\cos\varphi)^{-1}\,\partial_\varphi\partial_\theta g_B(\varphi,\theta)\,\mathbf{e}_\theta + g_B(\varphi,\theta)\,\mathbf{e}_n\,, & \text{if } \varphi \in \{0,\pi\}\,. \end{cases} \tag{16}$$

and the boundary's smoothness in terms of the geometric continuity is

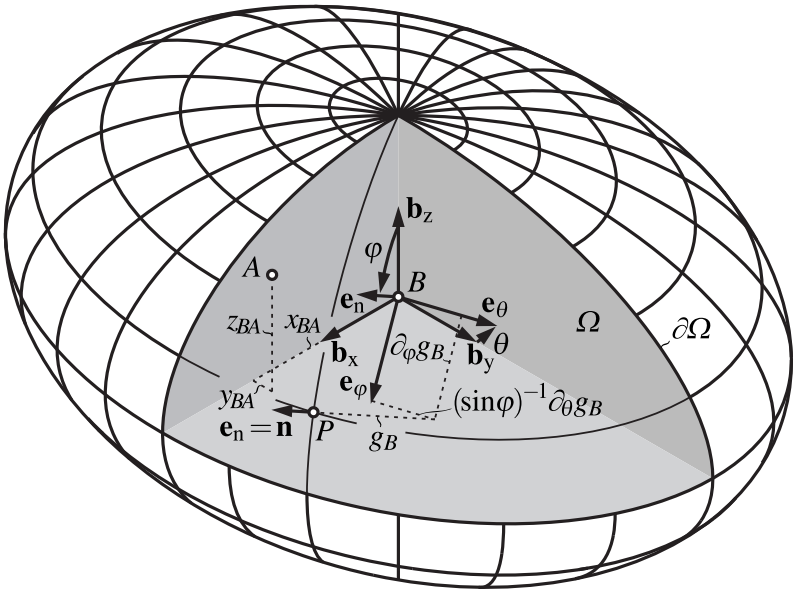

Figure 3: Normal parameterization of a strictly convex three-dimensional object Ω. Any point $P \in \partial\Omega$ is given by the generating potential g_B via Eq. (16) as a function of (φ, θ)—the direction of the outer normal vector $\mathbf{n}$ at P in spherical coordinates.

(i) $\partial\Omega \in G^0$ if the following conditions are true: $g_B \in SC^k, k \geq 1$ and

$$\partial_\varphi g_B(\varphi,\theta)\big|_{\varphi=0} = x_{BP,0}\cos\theta + y_{BP,0}\sin\theta\,, \quad \partial_\varphi g_B(\varphi,\theta)\big|_{\varphi=\pi} = x_{BP,\pi}\cos\theta - y_{BP,\pi}\sin\theta \tag{17}$$

with constants $x_{BP,0}, y_{BP,0}, x_{BP,\pi}, y_{BP,\pi} \in \mathbb{R}$;

(ii) $\partial\Omega \in G^1$ if the following conditions are true: $\partial\Omega \in G^0$, $g_B \in SC^k, k \geq 2$,

$$\begin{cases} e_0(\theta) = g_B(0,\theta) + \partial_\varphi^2 g_B(\varphi,\theta)\big|_{\varphi=0} = \kappa_{1,0}^{-1}\cos^2(\theta+\theta_0) + \kappa_{2,0}^{-1}\sin^2(\theta+\theta_0)\,, \\ e_\pi(\theta) = g_B(\pi,\theta) + \partial_\varphi^2 g_B(\varphi,\theta)\big|_{\varphi=\pi} = \kappa_{1,\pi}^{-1}\cos^2(\theta+\theta_\pi) + \kappa_{2,\pi}^{-1}\sin^2(\theta+\theta_\pi) \end{cases} \tag{18}$$

with constants $\{\kappa_{1,0}, \kappa_{2,0}, \kappa_{1,\pi}, \kappa_{2,\pi} \in \mathbb{R} \mid \kappa_{1,0} \geq \kappa_{2,0} > 0, \kappa_{1,\pi} \geq \kappa_{2,\pi} > 0\}$, $\theta_0, \theta_\pi \in \mathbb{S}^1$ and

$$0 < eg - f^2 \tag{19}$$

for all $\varphi \in (0,\pi), \theta \in \mathbb{S}^1$, with e, f, and g as defined in Eq. (21);

(iii) $\partial\Omega \in G^2$ if $\partial\Omega \in G^1$.

Remark 14. Let $g_B \in SC^k$ and $m, n \in \mathbb{N}$, $m + n \leq k + 1$, then

$$\partial_\varphi^m \partial_\theta^n g_B(\varphi,\theta)\big|_{\varphi=0} = \partial_\theta^n\left(\partial_\varphi^m g_B(\varphi,\theta)\big|_{\varphi=0}\right) \quad \text{and} \quad \partial_\varphi^m \partial_\theta^n g_B(\varphi,\theta)\big|_{\varphi=\pi} = \partial_\theta^n\left(\partial_\varphi^m g_B(\varphi,\theta)\big|_{\varphi=\pi}\right). \tag{20}$$

This follows directly from the required differentiability with $g(\varphi,\theta) = \partial_\varphi^m \partial_\theta^{n-1} g_B(\varphi,\theta)$, $g \in SC^1$ and

$$\partial_\theta\left(\lim_{\varphi\to0} g(\varphi,\theta)\right) = \lim_{h\to0}\frac{\lim\limits_{\varphi\to0} g(\varphi,\theta+h) - \lim\limits_{\varphi\to0} g(\varphi,\theta)}{h} = \lim_{h\to0}\frac{g(0,\theta+h) - g(0,\theta)}{h} = \partial_\theta g(0,\theta) = \lim_{\varphi\to0}\partial_\theta g(\varphi,\theta)\,.$$

A derivation of Eq. (16) on the basis of rigid body kinematics is given in Section 4. Before we continue with the proof of Proposition 13, introduce the abbreviations[7]

$$c = \cos\varphi\,, \tag{21a}$$
$$s = \sin\varphi\,, \tag{21b}$$
$$e = g_B(\varphi,\theta) + \partial_\varphi^2 g_B(\varphi,\theta)\,, \tag{21c}$$
$$f = \partial_\varphi\partial_\theta g_B(\varphi,\theta) - cs^{-1}\partial_\theta g_B(\varphi,\theta)\,, \tag{21d}$$
$$g = s^2 g_B(\varphi,\theta) + cs\,\partial_\varphi g_B(\varphi,\theta) + \partial_\theta^2 g_B(\varphi,\theta)\,, \tag{21e}$$
$$\tilde{f} = \tfrac{1}{2}c^{-1}\partial_\varphi^2\partial_\theta g_B(\varphi,\theta)\,, \tag{21f}$$
$$\tilde{g} = c\partial_\varphi g_B(\varphi,\theta) + c^{-1}\partial_\varphi\partial_\theta^2 g_B(\varphi,\theta)\,. \tag{21g}$$

Notice that

$$\tilde{f}\,\big|_{\varphi=0} = \tfrac{1}{2}\partial_\theta e|_{\varphi=0}\,, \quad \tilde{f}\,\big|_{\varphi=\pi} = -\tfrac{1}{2}\partial_\theta e|_{\varphi=\pi} \tag{22a}$$
$$\tilde{g}|_{\varphi=0} = 0\,, \qquad \tilde{g}|_{\varphi=\pi} = 0 \tag{22b}$$

due to Eqs. (15), (17) and (20) and consider the following relationships. Since $\mathbf{n}(\varphi,\theta) = \mathbf{e}_\mathrm{n}$, Eq. (14c) directly yields the differential

$$\mathrm{d}\mathbf{n} = \frac{\partial\mathbf{e}_\mathrm{n}}{\partial\varphi}\,\mathrm{d}\varphi + \frac{\partial\mathbf{e}_\mathrm{n}}{\partial\theta}\,\mathrm{d}\theta = \mathrm{d}\varphi\,\mathbf{e}_\varphi + \sin\varphi\,\mathrm{d}\theta\,\mathbf{e}_\theta\,. \tag{23}$$

Let $g_B \in SC^k, k \geq 2$, then Eqs. (16) and (22) give the differential

$$\mathrm{d}\mathbf{r} = \frac{\partial\mathbf{r}_{BP}}{\partial\varphi}\,\mathrm{d}\varphi + \frac{\partial\mathbf{r}_{BP}}{\partial\theta}\,\mathrm{d}\theta = \begin{cases} (e\,\mathrm{d}\varphi + f\,\mathrm{d}\theta)\,\mathbf{e}_\varphi + s^{-1}\,(f\,\mathrm{d}\varphi + g\,\mathrm{d}\theta)\,\mathbf{e}_\theta & \text{if } \varphi \in (0,\pi)\,, \\ e\,\mathrm{d}\varphi\,\mathbf{e}_\varphi + \left(\tilde{f}\,\mathrm{d}\varphi + \tilde{g}\,\mathrm{d}\theta\right)\mathbf{e}_\theta\,, & \text{if } \varphi \in \{0,\pi\} \end{cases} \tag{24}$$

$$= \begin{cases} (e\,\mathrm{d}\varphi + f\,\mathrm{d}\theta)\,\mathbf{e}_\varphi + s^{-1}\,(f\,\mathrm{d}\varphi + g\,\mathrm{d}\theta)\,\mathbf{e}_\theta & \text{if } \varphi \in (0,\pi)\,, \\ \left(e_0(\theta)\cos\theta - \frac{1}{2}e_0'(\theta)\sin\theta\right)\mathrm{d}\varphi\,\mathbf{b}_\mathrm{x} + \left(e_0(\theta)\sin\theta + \frac{1}{2}e_0'(\theta)\cos\theta\right)\mathrm{d}\varphi\,\mathbf{b}_\mathrm{y}\,, & \text{if } \varphi = 0\,, \\ -\left(e_\pi(\theta)\cos\theta - \frac{1}{2}e_\pi'(\theta)\sin\theta\right)\mathrm{d}\varphi\,\mathbf{b}_\mathrm{x} - \left(e_\pi(\theta)\sin\theta + \frac{1}{2}e_\pi'(\theta)\cos\theta\right)\mathrm{d}\varphi\,\mathbf{b}_\mathrm{y}\,, & \text{if } \varphi = \pi\,, \end{cases} \tag{25}$$

with $e_0(\theta), e_\pi(\theta)$ via Eq. (18). The principal curvatures are as follows.

Corollary 15. Let $\partial\Omega \in G^0$, $g_B \in SC^k, k \geq 2$, e, f, g, s via Eq. (21) and $\kappa_{1,0}$, $\kappa_{2,0}$, $\kappa_{1,\pi}$, $\kappa_{2,\pi}$, θ_0, θ_π via Eq. (18), then the boundary's *principal curvatures* are

$$\begin{cases} \kappa_1 = 1/e\,, \quad \kappa_2 = s^2/g\,, & \text{if } \varphi \in (0,\pi) \text{ and } f = 0\,, \\ \kappa_1 = \kappa_2 = \kappa = 1/(2e)\,, & \text{if } \varphi \in (0,\pi) \text{ and } g = s^2 e = \pm sf\,, \\ \kappa_{1/2} = \dfrac{(s^2e+g) \pm \sqrt{(s^2e-g)^2 + 4s^2f^2}}{2(eg-f^2)}\,, & \text{if } \varphi \in (0,\pi)\,,\ f \neq 0 \text{ and } (g \neq s^2e \text{ or } g \neq \pm sf)\,, \\ \kappa_1 = \kappa_{1,0}\,, \quad \kappa_2 = \kappa_{2,0}\,, & \text{if } \varphi = 0\,, \\ \kappa_1 = \kappa_{1,\pi}\,, \quad \kappa_2 = \kappa_{2,\pi}\,, & \text{if } \varphi = \pi\,, \end{cases} \tag{26}$$

[7] The abbreviations e, f and g are labeled consistently with the notation in [63]; $g, \tilde{g}$ are not to be confused with the generating potentials $g_B, \bar{g}_B$.

with the corresponding *curvature directions*

$$\begin{cases} \mathbf{c}_1 = \mathbf{e}_\varphi\,, \quad \mathbf{c}_2 = \mathbf{e}_\theta\,, & \text{if } \varphi \in (0,\pi) \text{ and } f = 0\,, \\ \mathbf{c}_1, \mathbf{c}_2 \perp \mathbf{e}_\mathrm{n}\,, & \text{if } \varphi \in (0,\pi) \text{ and } g = s^2 e = \pm sf\,, \\ \mathbf{c}_{1/2} = \dfrac{sf}{\sqrt{s^2f^2 + \left(g - (eg - f^2)\kappa_{1/2}\right)^2}}\mathbf{e}_\varphi + \dfrac{g - (eg - f^2)\kappa_{1/2}}{\sqrt{s^2f^2 + \left(g - (eg - f^2)\kappa_{1/2}\right)^2}}\mathbf{e}_\theta\,, & \text{if } \varphi \in (0,\pi)\,,\ f \neq 0 \\ & \quad \text{and } (g \neq s^2 e \text{ or } g \neq \pm sf)\,, \\ \mathbf{c}_1 = \cos\theta_0\,\mathbf{b}_\mathrm{x} + \sin\theta_0 \mathbf{b}_\mathrm{y}\,, \quad \mathbf{c}_2 = -\sin\theta_0\,\mathbf{b}_\mathrm{x} + \cos\theta_0\,\mathbf{b}_\mathrm{y} & \text{if } \varphi = 0\,, \\ \mathbf{c}_1 = \cos\theta_\pi\,\mathbf{b}_\mathrm{x} + \sin\theta_\pi \mathbf{b}_\mathrm{y}\,, \quad \mathbf{c}_2 = -\sin\theta_\pi\,\mathbf{b}_\mathrm{x} + \cos\theta_\pi\,\mathbf{b}_\mathrm{y} & \text{if } \varphi = \pi\,. \end{cases} \tag{27}$$

Proof. We first treat the regular case $\varphi \in (0,\pi)$ by the approach described in [63, Chapter 2]. The curvature can be derived from the differentials d$\mathbf{n}$ and d$\mathbf{r}$ in Eqs. (23) and (25). The first and the second fundamental form are[8]

$$\mathrm{I} \;= \mathrm{d}\mathbf{r}\cdot\mathrm{d}\mathbf{r} =: E\,\mathrm{d}\varphi^2 + 2F\,\mathrm{d}\varphi\,\mathrm{d}\theta + G\,\mathrm{d}\theta^2 = \left(e^2 + \frac{f^2}{s^2}\right)\mathrm{d}\varphi^2 + 2f\left(e + \frac{g}{s^2}\right)\mathrm{d}\varphi\,\mathrm{d}\theta + \left(f^2 + \frac{g^2}{s^2}\right)\mathrm{d}\theta^2\,, \tag{28a}$$

$$\mathrm{II} = \mathrm{d}\mathbf{r}\cdot\mathrm{d}\mathbf{n} = e\,\mathrm{d}\varphi^2 + 2f\,\mathrm{d}\varphi\,\mathrm{d}\theta + g\,\mathrm{d}\theta^2 \tag{28b}$$

and the normal curvature in direction $\lambda = \mathrm{d}\theta/\mathrm{d}\varphi$ is given by

$$\kappa(\lambda) = \frac{\mathrm{II}}{\mathrm{I}} = \frac{e + 2f\lambda + g\lambda^2}{E + 2F\lambda + G\lambda^2} = \frac{e + 2f\lambda + g\lambda^2}{\left(e^2 + \frac{f^2}{s^2}\right) + 2f\left(e + \frac{g}{s^2}\right)\lambda + \left(f^2 + \frac{g^2}{s^2}\right)\lambda^2}\,. \tag{29}$$

The two extrema of Eq. (29) are the principal curvatures $\kappa_{1/2}$ with the corresponding curvature directions $\mathbf{c}_{1/2} = \mathrm{d}\mathbf{r}_{1/2}/\sqrt{\mathrm{d}\mathbf{r}_{1/2}\cdot\mathrm{d}\mathbf{r}_{1/2}}$. If $f = 0$ then also $F = 0$ and the parametric lines are lines of curvature. The principle curvatures are then

$$\kappa_1 = 1/e\,, \quad \kappa_2 = s^2/g \tag{30}$$

with curvature directions

$$\mathbf{c}_1 = \mathbf{e}_\varphi\,, \quad \mathbf{c}_2 = \mathbf{e}_\theta\,. \tag{31}$$

If $g = s^2 e = \pm sf$, the first and the second fundamental form are proportional and the point is an *umbilic* (a navel point) with constant curvature

$$\kappa = 1/(2e) \tag{32}$$

in every tangent direction. In the general case, the extrema of Eq. (29) follow from

$$\frac{\mathrm{d}\kappa}{\mathrm{d}\lambda} = 0 \quad \Rightarrow \quad s^2\lambda(e + f\lambda) - (f + g\lambda) = s^2 f\lambda^2 + (s^2 e - g)\lambda - f = 0 \tag{33}$$

with the solutions

$$\lambda_{1/2} = \frac{-(s^2 e - g) \mp \sqrt{(s^2 e - g)^2 + 4s^2 f^2}}{2s^2 f}\,. \tag{34}$$

Substitution into Eq. (29) yields the principal curvatures

$$\kappa_{1/2} = \frac{(s^2 e + g) \pm \sqrt{(s^2 e - g)^2 + 4s^2 f^2}}{2(eg - f^2)} \tag{35}$$

[8] Compared to [63, (5-8)], the sign of the second fundamental form has to be changed due to the use of the outer normal vector $\mathbf{n}$ instead of the inner normal vector; cf. [63, p. 86, Chapter 2-8, 1.].

and the corresponding curvature directions

$$\begin{aligned}
\mathbf{c}_{1/2} &= \frac{s(e+f\lambda_{1/2})}{\sqrt{s^2(e+f\lambda_{1/2})^2+(f+g\lambda_{1/2})^2}}\mathbf{e}_\varphi + \frac{f+g\lambda_{1/2}}{\sqrt{s^2(e+f\lambda_{1/2})^2+(f+g\lambda_{1/2})^2}}\mathbf{e}_\theta \\
&= \frac{s(e+f\lambda_{1/2})}{\sqrt{s^2(e+f\lambda_{1/2})^2+s^4\lambda_{1/2}^2(e+f\lambda_{1/2})^2}}\mathbf{e}_\varphi + \frac{s^2\lambda_{1/2}(e+f\lambda_{1/2})}{\sqrt{s^2(e+f\lambda_{1/2})^2+s^4\lambda_{1/2}^2(e+f\lambda_{1/2})^2}}\mathbf{e}_\theta \\
&= \frac{sf}{\sqrt{s^2f^2+s^4f^2\lambda_{1/2}^2}}\mathbf{e}_\varphi + \frac{s^2f\lambda_{1/2}}{\sqrt{s^2f^2+s^4f^2\lambda_{1/2}^2}}\mathbf{e}_\theta \\
&= \frac{sf}{\sqrt{s^2f^2+\left(g-(eg-f^2)\kappa_{1/2}\right)^2}}\mathbf{e}_\varphi + \frac{g-(eg-f^2)\kappa_{1/2}}{\sqrt{s^2f^2+\left(g-(eg-f^2)\kappa_{1/2}\right)^2}}\mathbf{e}_\theta\,. \qquad (36)
\end{aligned}$$

In the first simplification step $(f+g\lambda_{1/2}) = s^2\lambda_{1/2}(e+f\lambda_{1/2})$ via Eq. (33) is substituted.

In the singular cases $\varphi \in \{0,\pi\}$ the singular points P_0 and P_π with respect to the body-fixed reference frame $\mathcal{B}$ are given by $\varphi = 0$ and $\varphi = \pi$, cf. Eq. (46). $\mathbf{r}_{BP}|_{\varphi\in\{0,\pi\}}$ is independent of $\theta \in \mathbb{S}^1$ which only determines the orientation of reference frame $\mathcal{E}$. Any smooth curve on the boundary surface which passes through one of the singular points P_0 or P_π can be decomposed into two curve segments, each starting at the singular point with antiparallel tangent vectors $\mathbf{t}$.

To derive the normal curvature from any curve which starts at a singular point with a certain tangent direction $\mathbf{t}$, consider the first and second fundamental forms

$$\mathrm{I}_0 = \left((e_0(\theta))^2 + \left(\tfrac{1}{2}e_0'(\theta)\right)^2\right)\mathrm{d}\varphi^2\,, \quad \mathrm{I}_\pi = \left((e_\pi(\theta))^2 + \left(\tfrac{1}{2}e_\pi'(\theta)\right)^2\right)\mathrm{d}\varphi^2\,, \qquad (37a)$$

$$\mathrm{II}_0 = e_0(\theta)\,\mathrm{d}\varphi^2\,, \qquad \mathrm{II}_\pi = e_\pi(\theta)\,\mathrm{d}\varphi^2 \qquad (37b)$$

which are functions of θ. The normal curvatures are then

$$\kappa_0(\theta) = \frac{\mathrm{II}_0}{\mathrm{I}_0} = \frac{e_0(\theta)}{(e_0(\theta))^2 + \left(\tfrac{1}{2}e_0'(\theta)\right)^2}\,, \quad \kappa_\pi(\theta) = \frac{\mathrm{II}_\pi}{\mathrm{I}_\pi} = \frac{e_\pi(\theta)}{(e_\pi(\theta))^2 + \left(\tfrac{1}{2}e_\pi'(\theta)\right)^2} \qquad (38)$$

in directions

$$\mathbf{t}_0 = \cos(\theta+\psi_0(\theta))\,\mathbf{b}_\mathrm{x} + \sin(\theta+\psi_0(\theta))\,\mathbf{b}_\mathrm{y}\,, \quad \mathbf{t}_\pi = -\cos(\theta+\psi_\pi(\theta))\,\mathbf{b}_\mathrm{x} - \sin(\theta+\psi_\pi(\theta))\,\mathbf{b}_\mathrm{y} \qquad (39)$$

with

$$\cos(\psi_0) = \frac{e_0(\theta)}{\sqrt{(e_0(\theta))^2 + \left(\tfrac{1}{2}e_0'(\theta)\right)^2}}\,, \quad \sin(\psi_0) = \frac{\tfrac{1}{2}e_0'(\theta)}{\sqrt{(e_0(\theta))^2 + \left(\tfrac{1}{2}e_0'(\theta)\right)^2}}\,, \qquad (40a)$$

$$\cos(\psi_\pi) = \frac{e_\pi(\theta)}{\sqrt{(e_\pi(\theta))^2 + \left(\tfrac{1}{2}e_\pi'(\theta)\right)^2}}\,, \quad \sin(\psi_\pi) = \frac{\tfrac{1}{2}e_\pi'(\theta)}{\sqrt{(e_\pi(\theta))^2 + \left(\tfrac{1}{2}e_\pi'(\theta)\right)^2}}\,. \qquad (40b)$$

The necessary and sufficient conditions for continuous normal curvature in all directions are

$$e_0(\theta) = e_0(\theta\pm\pi)\,, \quad e_\pi(\theta) = e_\pi(\theta\pm\pi)\,, \quad \text{for all } \theta \in \mathbb{S}^1\,, \qquad (41)$$

which are satisfied by the requirements of Eq. (18). Substitution of the relationships Eq. (18) into (38) yields

$$
\begin{aligned}
\kappa_0(\theta) &= \frac{e_0(\theta)}{(e_0(\theta))^2 + \left(\frac{1}{2}e_0'(\theta)\right)^2} \\
&= \frac{\kappa_{1,0}^{-1}\cos^2(\theta+\theta_0) + \kappa_{2,0}^{-1}\sin^2(\theta+\theta_0)}{(e_0(\theta))^2 + \left(\frac{1}{2}e_0'(\theta)\right)^2} \\
&= \frac{\left(\kappa_{1,0}^{-1}\cos^2(\theta+\theta_0) + \kappa_{2,0}^{-1}\sin^2(\theta+\theta_0)\right)\left(\cos^2(\theta+\theta_0) + \sin^2(\theta+\theta_0)\right)^2}{(e_0(\theta))^2 + \left(\frac{1}{2}e_0'(\theta)\right)^2} \\
&= \frac{\kappa_{1,0}^{-1}\left(\cos^3(\theta+\theta_0) + \cos(\theta+\theta_0)\sin^2(\theta+\theta_0)\right)^2}{(e_0(\theta))^2 + \left(\frac{1}{2}e_0'(\theta)\right)^2} + \frac{\kappa_{2,0}^{-1}\left(\sin(\theta+\theta_0)\cos^2(\theta+\theta_0) + \sin^3(\theta+\theta_0)\right)^2}{(e_0(\theta))^2 + \left(\frac{1}{2}e_0'(\theta)\right)^2} \\
&= \frac{\kappa_{1,0}\left(\cos(\theta+\theta_0)\left(\kappa_{1,0}^{-1}\cos^2(\theta+\theta_0) + \kappa_{2,0}^{-1}\sin^2(\theta+\theta_0)\right) - \frac{1}{2}\sin(\theta+\theta_0)\left(2(\kappa_{2,0}^{-1} - \kappa_{1,0}^{-1})\sin(\theta+\theta_0)\cos(\theta+\theta_0)\right)\right)^2}{(e_0(\theta))^2 + \left(\frac{1}{2}e_0'(\theta)\right)^2} \\
&\quad + \frac{\kappa_{2,0}\left(\sin(\theta+\theta_0)\left(\kappa_{1,0}^{-1}\cos^2(\theta+\theta_0) + \kappa_{2,0}^{-1}\sin^2(\theta+\theta_0)\right) + \frac{1}{2}\cos(\theta+\theta_0)\left(2(\kappa_{2,0}^{-1} - \kappa_{1,0}^{-1})\sin(\theta+\theta_0)\cos(\theta+\theta_0)\right)\right)^2}{(e_0(\theta))^2 + \left(\frac{1}{2}e_0'(\theta)\right)^2} \\
&= \kappa_{1,0}\frac{\left(e_0(\theta)\cos(\theta+\theta_0) - \frac{1}{2}e_0'(\theta)\sin(\theta+\theta_0)\right)^2}{(e_0(\theta))^2 + \left(\frac{1}{2}e_0'(\theta)\right)^2} + \kappa_{2,0}\frac{\left(e_0(\theta)\sin(\theta+\theta_0) + \frac{1}{2}e_0'(\theta)\cos(\theta+\theta_0)\right)^2}{(e_0(\theta))^2 + \left(\frac{1}{2}e_0'(\theta)\right)^2} \\
&= \kappa_{1,0}\cos^2(\theta+\theta_0+\psi_0) + \kappa_{2,0}\sin^2(\theta+\theta_0+\psi_0)\,.
\end{aligned}
$$

Using the angles $\tilde{\theta}_0 = \theta + \theta_0 + \psi_0$ and $\tilde{\theta}_\pi = \theta + \theta_\pi + \psi_\pi$, the curvatures in directions

$$
\mathbf{t}_0 = \cos(\tilde{\theta}_0 - \theta_0)\,\mathbf{b}_\mathrm{x} + \sin(\tilde{\theta}_0 - \theta_0)\,\mathbf{b}_\mathrm{y}\,, \quad \mathbf{t}_\pi = -\cos(\tilde{\theta}_\pi - \theta_\pi)\,\mathbf{b}_\mathrm{x} - \sin(\tilde{\theta}_\pi - \theta_\pi)\,\mathbf{b}_\mathrm{y} \tag{42}
$$

are

$$
\kappa_0(\tilde{\theta}_0) = \kappa_{1,0}\cos^2(\tilde{\theta}_0) + \kappa_{2,0}\sin^2(\tilde{\theta}_0)\,, \quad \kappa_\pi(\tilde{\theta}_\pi) = \kappa_{1,\pi}\cos^2(\tilde{\theta}_\pi) + \kappa_{2,\pi}\sin^2(\tilde{\theta}_\pi) \tag{43}
$$

which shows that Euler's theorem [63, p. 81] holds at the singular points due to the requirements via Eq. (18).[9] The principal curvatures are therefore $\kappa_{1,0}, \kappa_{2,0}$ and $\kappa_{1,\pi}, \kappa_{2,\pi}$ with corresponding curvature directions

$$
\begin{cases}
\mathbf{c}_1 = \cos\theta_0\,\mathbf{b}_\mathrm{x} + \sin\theta_0\mathbf{b}_\mathrm{y}\,, \quad \mathbf{c}_2 = -\sin\theta_0\,\mathbf{b}_\mathrm{x} + \cos\theta_0\,\mathbf{b}_\mathrm{y} & \text{if } \varphi = 0\,, \\
\mathbf{c}_1 = \cos\theta_\pi\,\mathbf{b}_\mathrm{x} + \sin\theta_\pi\mathbf{b}_\mathrm{y}\,, \quad \mathbf{c}_2 = -\sin\theta_\pi\,\mathbf{b}_\mathrm{x} + \cos\theta_\pi\,\mathbf{b}_\mathrm{y} & \text{if } \varphi = \pi\,.
\end{cases} \tag{44}
$$

If $e_0(\theta) = \kappa_{1,0}^{-1} = \kappa_{2,0}^{-1} = \kappa_0^{-1}$ or $e_\pi(\theta) = \kappa_{1,\pi}^{-1} = \kappa_{2,\pi}^{-1} = \kappa_\pi^{-1}$ are constant, the normal curvature at the respective singular point is equal in every direction and the singular point is an umbilic (a navel point). Then all tangent directions are curvature directions and θ_0 or θ_π are arbitrary. □

Proof of Proposition 13. The differential $\mathrm{d}\mathbf{r} \perp \mathbf{e}_\mathrm{n}$ via Eq. (25) proofs that the normal parameterization via Eq. (16) indeed describes the boundary $\partial\Omega$ as a function of the outer normal direction $(\varphi, \theta) \mapsto \mathbf{n}(\varphi, \theta) = \mathbf{e}_\mathrm{n}$. The tangent plane is spanned by $\{\mathbf{e}_\varphi, \mathbf{e}_\theta\}$. In the singular cases $\varphi \in \{0, \pi\}$, the limits

$$
\lim_{\varphi \to \{0,\pi\}} \frac{\partial_\theta g_B(\varphi, \theta)}{\sin\varphi} = \left.\frac{\partial_\varphi \partial_\theta g_B(\varphi, \theta)}{\cos\varphi}\right|_{\varphi \in \{0,\pi\}} \tag{45}
$$

[9] Since the coordinate singularities arise purely due to the choice of the reference frame $\mathcal{B}$ and not due to any property of the boundary $\partial\Omega$, Eq. (18) is introduced so that Euler's theorem is valid at the singular points.

follow from the regular case via L'Hôpital's rule since $\partial_\theta g_B(\varphi,\theta)|_{\varphi\in\{0,\pi\}} = 0$ via Eq. (15). The normal parameterization via Eq. (16) is valid for any point $P \in \partial\Omega$.

The propositions with regard to the boundary's geometric continuity can be shown as follows.

(i) In the regular case $\varphi \in (0,\pi)$, the functions $\mathbf{r}_{BP}\cdot\mathbf{b}_\mathrm{x}, \mathbf{r}_{BP}\cdot\mathbf{b}_\mathrm{y}, \mathbf{r}_{BP}\cdot\mathbf{b}_\mathrm{z}$ via Eqs. (14) and (16) are continuous iff g_B, $\partial_\varphi g_B$ and $\partial_\theta g_B$ are continuous.

In the singular cases $\varphi \in \{0,\pi\}$, the normal direction $\mathbf{e}_\mathrm{n}$ is constant via Eq. (14c) and therefore consistency requires a unique point $P \in \partial\Omega$ to be associated with each singular case. Therefore,

$$\mathbf{r}_{BP}(\varphi,\theta) = \begin{cases} x_{BP,0}\,\mathbf{b}_\mathrm{x} + y_{BP,0}\,\mathbf{b}_\mathrm{y} + g_B(\varphi,\theta)\,\mathbf{b}_\mathrm{z} = \partial_\varphi g_B(\varphi,\theta)\,\mathbf{e}_\varphi + \partial_\theta\partial_\varphi g_B(\varphi,\theta)\,\mathbf{e}_\theta + g_B(\varphi,\theta)\,\mathbf{e}_\mathrm{n}\,, & \text{if } \varphi = 0\,, \\ x_{BP,\pi}\,\mathbf{b}_\mathrm{x} + y_{BP,\pi}\,\mathbf{b}_\mathrm{y} - g_B(\varphi,\theta)\,\mathbf{b}_\mathrm{z} = \partial_\varphi g_B(\varphi,\theta)\,\mathbf{e}_\varphi - \partial_\theta\partial_\varphi g_B(\varphi,\theta)\,\mathbf{e}_\theta + g_B(\varphi,\theta)\,\mathbf{e}_\mathrm{n}\,, & \text{if } \varphi = \pi \end{cases} \tag{46}$$

must be constant in the body-fixed frame $\mathcal{B}$. Substitution of Eqs. (14) and a comparison of coefficients directly yields Eqs. (17). Continuity in the regular case, consistency of both singular cases and the limit characteristic (45) imply $\partial\Omega \in G^0$ if $g_B \in SC^k, k \geq 1$.

(ii) $\partial\Omega \in G^1$ iff the outer normal vector $\mathbf{n}$ is unique at every point $P \in \partial\Omega$ on the boundary. In the regular case $\varphi \in (0,\pi)$, positive definiteness of the first fundamental form I is the necessary and sufficient condition for this requirement, analogously to the two-dimensional case in Section 2. The first fundamental form I is positive definite iff $EG - F^2 > 0$, which directly yields Eq. (19) after substitution of the abbreviations given by Eq. (21). The second fundamental form II is then also positive definite.

In the singular cases $\varphi \in \{0,\pi\}$, the normal vector at the respective singular point is unique iff the curvature radii $R_0(\theta) = (\kappa_0(\theta))^{-1} > 0$ and $R_\pi(\theta) = (\kappa_\pi(\theta))^{-1} > 0$ for all $\theta \in \mathbb{S}^1$ which is true via Eq. (43) since $\kappa_{1,0}, \kappa_{2,0}, \kappa_{1,\pi}, \kappa_{2,\pi} > 0$.

(iii) Let $\partial\Omega \in G^1$, then the principal curvatures via Eq. (26) and the curvature directions via Eq. (27) are continuous functions of (φ,θ) which implies $\partial\Omega \in G^2$. □

Corollary 16. Given the generating potential g_B for point B, the generating potential for a different point A at $\mathbf{r}_{BA} = x_{BA}\mathbf{b}_\mathrm{x} + y_{BA}\mathbf{b}_\mathrm{y} + z_{BA}\mathbf{b}_\mathrm{z}$ (cf. Fig. 3) is

$$g_A(\varphi,\theta) = g_B(\varphi,\theta) - (x_{BA}\sin\varphi\,\cos\theta + y_{BA}\sin\varphi\,\sin\theta + z_{BA}\cos\varphi)\ . \tag{47}$$

Proof. This relationship follows directly from $\mathbf{r}_{AP} = \mathbf{r}_{BP} - \mathbf{r}_{BA}$ and Eq. (16). □

Remark 17. Since Eq. (47) holds for all $\mathbf{r}_{BA} \in \mathbb{R}^3$, point A (and therefore also point B) may lie outside the object Ω. Then $\min_{(\varphi,\theta)\in\mathbb{S}^2} g_A < 0$.

Remark 18. Changing the orientation of the body-fixed reference frame requires a nonlinear coordinate change $(\varphi,\theta) \mapsto (\bar\varphi,\bar\theta)$ and also changes the coordinate singularities. Due to the excessive length of this procedure, this has not been investigated further.

Corollary 19. Given $\partial\Omega \in G^2$ via g_B, then the normal parameterization $\bar g_B$ of any equidistant boundary surface $\partial\bar\Omega$ with constant distance $d \in \mathbb{R}$ is

$$\bar g_B(\varphi,\theta) = g_B(\varphi,\theta) + d\ . \tag{48}$$

Proof. This relationship follows directly from

$$\begin{aligned} \mathbf{r}_{B\bar P}(\varphi,\theta) &= \mathbf{r}_{BP}(\varphi,\theta) + d\,\mathbf{e}_\mathrm{n} \\ &= \begin{cases} \partial_\varphi g_B(\varphi,\theta)\,\mathbf{e}_\varphi + (\sin\varphi)^{-1}\,\partial_\theta g_B(\varphi,\theta)\,\mathbf{e}_\theta + (g_B(\varphi,\theta)+d)\,\mathbf{e}_\mathrm{n}\,, & \text{if } \varphi \in (0,\pi)\,, \\ \partial_\varphi g_B(\varphi,\theta)\,\mathbf{e}_\varphi + (\cos\varphi)^{-1}\,\partial_\varphi\partial_\theta g_B(\varphi,\theta)\,\mathbf{e}_\theta + (g_B(\varphi,\theta)+d)\,\mathbf{e}_\mathrm{n}\,, & \text{if } \varphi \in \{0,\pi\} \end{cases} \\ &= \begin{cases} \partial_\varphi \bar g_B(\varphi,\theta)\,\mathbf{e}_\varphi + (\sin\varphi)^{-1}\,\partial_\theta \bar g_B(\varphi,\theta)\,\mathbf{e}_\theta + \bar g_B(\varphi,\theta)\,\mathbf{e}_\mathrm{n}\,, & \text{if } \varphi \in (0,\pi)\,, \\ \partial_\varphi \bar g_B(\varphi,\theta)\,\mathbf{e}_\varphi + (\cos\varphi)^{-1}\,\partial_\varphi\partial_\theta \bar g_B(\varphi,\theta)\,\mathbf{e}_\theta + \bar g_B(\varphi,\theta)\,\mathbf{e}_\mathrm{n}\,, & \text{if } \varphi \in \{0,\pi\} \end{cases} \end{aligned}$$

where $\mathbf{r}_{B\bar P}(\varphi)$ is a normal parameterization for any point $\bar P \in \partial\bar\Omega$ with outer normal vector $\mathbf{n} = \mathbf{e}_\mathrm{n}$. □

Remark 20. Analogously to the discussion of the two-dimensional case in Remark 8, there is a minimum value for d below which the object enclosed by the equidistant boundary surface is not convex any more. To determine this minimum value, both the regular and the singular cases have to be evaluated. In the regular case $\varphi \in (0, \pi)$, positive definiteness of the first fundamental form of the equidistant boundary surface is determined by the necessary and sufficient condition

$$\bar{e}\bar{g} - \bar{f}^2 = (e + d)(g + s^2 d) - f^2 = s^2 d^2 + (s^2 e + g)d + (eg - f^2) > 0 \tag{49}$$

via Eqs. (19), (21) and (48). If Eq. (49) becomes equal to zero, positive definiteness is lost; if the expression becomes negative, convexity is lost. This gives a quadratic equation for d with two negative solutions (assuming $eg - f^2 > 0$). The smallest absolute value of the solution $(\sqrt{(s^2 e + g)^2 - 4s^2 f^2} - (s^2 e + g))/(2s^2)$ for any $\varphi \in (0, \pi)$, $\theta \in \mathbb{S}^1$ is the lower bound for d in this case. In the singular cases $\varphi \in \{0, \pi\}$, the according condition is vanishing of the curvature radius $R = \kappa^{-1}$ in any direction. Eqs. (18) and (43) give the lower bounds $-\kappa_{1,0}^{-1}$ and $-\kappa_{1,\pi}^{-1}$ for these cases. Therefore, the minimum value of d is

$$d_{\min} = \max \left\{ -\kappa_{1,0}^{-1}, -\kappa_{1,\pi}^{-1}, \max_{\varphi \in (0,\pi), \theta \in \mathbb{S}^1} \frac{\sqrt{(s^2 e + g)^2 - 4s^2 f^2} - (s^2 e + g)}{2s^2} \right\} . \tag{50}$$

Remark 21. The generating potential of a sphere with respect to its center is constant (its radius). The generating potential of an ellipsoid with respect to its center is

$$g_B(\varphi, \theta) = \sqrt{a^2 \sin^2 \varphi \cos^2 \theta + b^2 \sin^2 \varphi \sin^2 \theta + c^2 \cos^2 \varphi} \tag{51}$$

with semi-axes a, b and c. By expressing $\mathbf{r}_{BP}(\varphi, \theta)$ via Eq. (16) and substitution of Eq. (51) it can be verified that the implicit equation

$$\left(\frac{x}{a}\right)^2 + \left(\frac{y}{b}\right)^2 + \left(\frac{z}{c}\right)^2 - 1 = \left(\frac{\mathbf{r}_{BP} \cdot \mathbf{b}_\mathrm{x}}{a}\right)^2 + \left(\frac{\mathbf{r}_{BP} \cdot \mathbf{b}_\mathrm{y}}{b}\right)^2 + \left(\frac{\mathbf{r}_{BP} \cdot \mathbf{b}_\mathrm{z}}{c}\right)^2 - 1 = 0$$

is satisfied. Even more general, the generating potential

$$g_B(\varphi, \theta) = \left(\left(a^2 \sin^2 \varphi \cos^2 \theta \right)^{\frac{\delta}{2(\delta-1)}} + \left(b^2 \sin^2 \varphi \sin^2 \theta \right)^{\frac{\delta}{2(\delta-1)}} \right)^{\frac{\epsilon(\delta-1)}{\delta(\epsilon-1)}} + \left(c^2 \cos^2 \varphi \right)^{\frac{\epsilon}{2(\epsilon-1)}} \Bigg)^{\frac{\epsilon-1}{\epsilon}} \tag{52}$$

with $\delta, \epsilon > 1$ fulfills the implicit equation

$$\left(\left(\left(\frac{x}{a} \right)^2 \right)^{\frac{\delta}{2}} + \left(\left(\frac{y}{b} \right)^2 \right)^{\frac{\delta}{2}} \right)^{\frac{\epsilon}{\delta}} + \left(\left(\frac{z}{c} \right)^2 \right)^{\frac{\epsilon}{2}} - 1 = \left(\left(\left(\frac{\mathbf{r}_{BP} \cdot \mathbf{b}_\mathrm{x}}{a} \right)^2 \right)^{\frac{\delta}{2}} + \left(\left(\frac{\mathbf{r}_{BP} \cdot \mathbf{b}_\mathrm{y}}{b} \right)^2 \right)^{\frac{\delta}{2}} \right)^{\frac{\epsilon}{\delta}} + \left(\left(\frac{\mathbf{r}_{BP} \cdot \mathbf{b}_\mathrm{z}}{c} \right)^2 \right)^{\frac{\epsilon}{2}} - 1 = 0$$

of a superellipsoid. With $\delta = \epsilon$ this includes superquadrics as a special case.

Remark 22. Analogous to the proposal for the two-dimensional case in Remark 11, an approximation to any strictly convex geometry is possible by specifying the generating potential g_B by piecewise defined functions like splines or NURBS. Once such a generating potential is specified, the corresponding boundary $\partial\Omega$ follows from Eq. (16) and the coefficients of the ansatz can be fitted approximate the given geometry. Proposition 13 gives all prerequisites for this approach to achieve a desired geometric continuity. This approach will not be discussed further in the present manuscript.

4. Derivation of the normal parameterization

The normal parameterization Eq. (16) can be derived from basic rigid body kinematics; an approach which has not been proposed in any literature we are aware of. This offers another perspective which originates in mechanics rather than geometry. The basic approach is used in [54] to derive the normal parameterization for two-dimensional objects from the kinematics of a rolling contact with a straight line. This can be regarded as a special case of a three-dimensional object which is rolling on a plane where the axis of rotation is fixed and parallel to the plane. The key concepts of the two-dimensional approach in this light are recalled in Section 4.1 and subsequently generalized to the general three-dimensional rolling contact between any strictly convex object and a plane in Section 4.2.

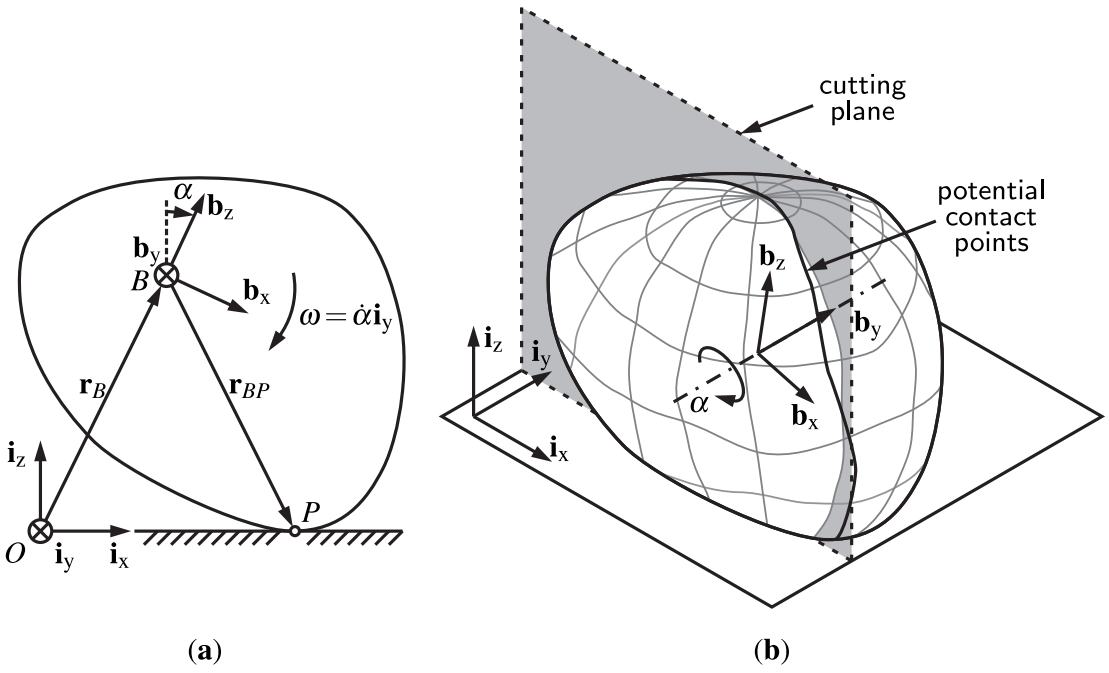

Figure 4: Approach for two-dimensional contact problem (from [54]): (**a**) contact between a two-dimensional convex object and a straight line; rotation around the body-fixed axis $\mathbf{b}_y$ as introduced in [54]. This is interpreted as a special case of (**b**) the contact between a three-dimensional convex object and a plane with the same restrictions: no translation in $\mathbf{b}_y$-direction and rotation only around this axis. Perspective view with an additional cutting plane (gray, perpendicular to $\mathbf{b}_y$). A full rotation around the axis $\mathbf{b}_y$ produces a line of potential contact points on the object's boundary (black); in general these points do not lie in a common cutting plane. However, their projection along $\mathbf{b}_y$ produces the boundary of the two-dimensional object in (**a**).

4.1. Rolling contact between a strictly convex two-dimensional object and a straight line

The two-dimensional contact detection problem between a strictly convex object and a straight line from [54] can be interpreted as a special case of the three-dimensional contact between a convex object and a plane: the object is rotating around a body-fixed axis which is parallel to the plane (denoted $\mathbf{b}_y$ in [54]) and any translation is perpendicular to said axis, cf. Fig. 4a. The rotation of the three-dimensional object around the body-fixed axis by an angle α produces a continuous set of potential contact points on the body's boundary, as depicted in Fig. 4b. In general, these points do not lie in a common plane, however, their projection onto the cutting plane that is perpendicular to the axis of rotation gives the boundary of the two-dimensional object. In this special case, the distance of any body-fixed reference point B from the contact plane is a function of α. As derived in [54, Section 4], it follows that

$$\mathbf{r}_B = x_B(\alpha)\,\mathbf{i}_x + z_P(\alpha)\,\mathbf{i}_z\,, \tag{53}$$

$$\mathbf{r}_P = x_P(\alpha)\,\mathbf{i}_x\,, \tag{54}$$

$$\begin{aligned}\mathbf{r}_{BP} &= \mathbf{r}_P - \mathbf{r}_B \\ &= x_{BP}(\alpha)\,\mathbf{i}_x + z_{BP}(\alpha)\,\mathbf{i}_z\,,\end{aligned} \tag{55}$$

and

$$z_B(\alpha) = g_B(\alpha)\,, \tag{56}$$

$$z_{BP}(\alpha) = -g_B(\alpha)\,, \tag{57}$$

where $g_B(\alpha)$ is the generating potential as is shown below. The dependency of $x_{BP}(\alpha)$ on $g_B(\alpha)$ follows from the velocity of P for an arbitrary angular velocity $\boldsymbol{\omega} = \dot{\alpha}\,\mathbf{i}_y$ which can be derived in two ways: differentiation of the position yields [54, Eq. (20)]

$$\mathbf{v}_B = \dot{\mathbf{r}}_B = \dot{x}_B(\alpha)\,\mathbf{i}_x + \dot{z}_B(\alpha)\,\mathbf{i}_z = x'_B(\alpha)\dot{\alpha}\,\mathbf{i}_x + g'_B(\alpha)\dot{\alpha}\,\mathbf{i}_z\,, \tag{58}$$

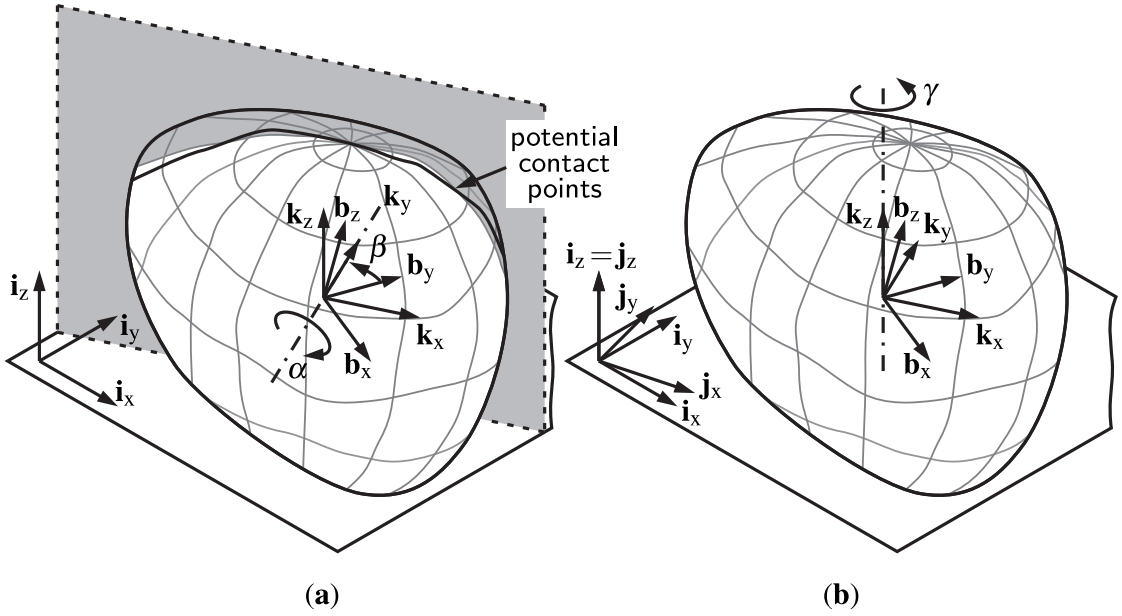

(**a**) (**b**)

Figure 5: Generalization to three-dimensional contact problem: (**a**) Rotation of the object (the body-fixed frame $\mathcal{B}$) around a body-fixed axis $\mathbf{k}_y$ which is parallel to the plane. The direction of $\mathbf{k}_y$ in the $\{\mathbf{b}_x, \mathbf{b}_y\}$-plane is defined by the angle β. A full rotation around the fixed axis $\mathbf{k}_y$ produces a line of potential contact points on the object's boundary (black), cf. Fig. 4b. (**b**) Second (subsequent) rotation of the object around $\mathbf{i}_z$ by the angle γ. This drilling motion does not change the contact point as seen by an observer which is rotating with the object. The intermediate reference frame $\mathcal{J}$ is used below to properly define this rotation, cf. Fig. 6.

and the rolling condition

$$\dot{\mathbf{r}}_P = \mathbf{v}_P = \mathbf{0} \tag{59}$$

results in [54, Eq. (22)]

$$\mathbf{v}_B = \mathbf{v}_P + \boldsymbol{\omega} \times \mathbf{r}_{PB} = g_B(\alpha)\dot{\alpha}\,\mathbf{i}_x + x_{BP}(\alpha)\dot{\alpha}\,\mathbf{i}_z \,. \tag{60}$$

Comparison of the coefficients in Eqs. (58) and (60) yields

$$x_{BP}(\alpha) = g_B'(\alpha) \,, \tag{61}$$

$$\mathbf{r}_{BP}(\alpha) = g_B'(\alpha)\,\mathbf{i}_x + g_B(\alpha)\,\mathbf{i}_z \tag{62}$$

which just equals Eq. (2) with $\mathbf{e}_n = -\mathbf{i}_z$ and $\mathbf{e}_\varphi = \mathbf{i}_x$.

These observations motivate a straightforward approach for the generalization of the solution of the two-dimensional contact detection problem: every body-fixed axis of rotation which is parallel to the contact plane produces a (slightly different) two-dimensional contact problem; the combination of all these two-dimensional solutions yields the desired solution for the three-dimensional problem.

For any body-fixed axis of rotation which is parallel to the plane, the body-fixed frame $\mathcal{B}$ aligns with $\mathcal{I}$ in the initial configuration $\alpha = 0$. This means that the axis of rotation is always perpendicular to $\mathbf{b}_z$ and $\mathbf{i}_z$, hence it is simultaneously part of the $\{\mathbf{b}_x, \mathbf{b}_y\}$-plane and of the $\{\mathbf{i}_x, \mathbf{i}_y\}$-plane. For the sake of clarity, an intermediate reference frame $\mathcal{K}$ is introduced in the following way: the (body-fixed) axis of rotation is given by $\mathbf{k}_y$ and $\mathbf{k}_z \equiv \mathbf{i}_z$. The orientation of $\mathbf{k}_y$ in the $\{\mathbf{b}_x, \mathbf{b}_y\}$-plane is described by the angle β, cf. Fig. 5a. The special case $\beta = 0$ results in $\mathbf{i}_y = \mathbf{k}_y = \mathbf{b}_y$ which is depicted in Fig. 4.

Any body-fixed axis $\mathbf{k}_y$ which is given by some constant value of β produces a corresponding line of potential contact points on the object's boundary. Any point of this line can be turned into the actual contact point by a corresponding value for the angle α. Furthermore, an infinitesimal change from β to $\beta + \mathrm{d}\beta$ produces a different, but

infinitesimally close line of potential contact points. Assuming sufficient smoothness, these lines of potential contact points cover the whole boundary of the object. The described procedure produces a set of spherical coordinates $(\alpha, \beta) \in \mathbb{S}^2$ which can be used to parameterize the object's boundary in dependence of the normal direction at any point (by the common normal concept, the outer normal vector at the actual contact point has to be anti-parallel to $\mathbf{i}_z$, the contact plane's outer normal vector). Any point on the object's boundary can be turned into the actual contact point by specific values of α and β.

However, this approach is still incomplete because it lacks the ability to rotate the object into an arbitrary orientation with respect to the inertial frame $\mathcal{I}$. A subsequent, second rotation is necessary to complete the proposed approach. Firstly, a certain point on the object's boundary is turned into the actual contact point by the procedure described above. The object is then rotated around $\mathbf{i}_z$ by a third angle γ until the desired orientation is reached. This drilling motion does not change the body-fixed contact point $P(\alpha, \beta)$ as seen by an observer which is rotating with the object. Another intermediate reference frame $\mathcal{J}$ is introduced below to properly define both active rotations of the object. The first rotation via α and β is then performed with respect to this intermediate frame instead of the reference frame. The second rotation of the object is achieved by the rotation of frame $\mathcal{J}$ with respect to $\mathcal{I}$.

4.2. Rolling contact between a strictly convex three-dimensional object and a plane

The contact point on the object's boundary as a function of its orientation relative to the plane can be derived as a function of the angles $(\alpha, \beta) \in \mathbb{S}^1$ and the assumption of strict convexity. The first step in this endeavor is the derivation of transformation matrices which define the orientation of the body-fixed reference frame $\mathcal{B}$ as well as the two intermediate frames $\mathcal{J}$ and $\mathcal{K}$ with respect to the inertial frame $\mathcal{I}$ and to each other. The angular velocity of the object can be expressed in term of the three angles α, β and γ and their time derivatives and follows directly from the transformation matrix which describes $\mathcal{B}$ with respect to $\mathcal{I}$. The next step in the following derivation assumes that the position of the potential contact point P with respect to a body-fixed reference point B is a function of α and β only, as motivated above. Analogously to [54], the special case of rolling without slipping is used to derive the kinematic relationships for the position of P.

The orientations of all four reference frames relative to each other for arbitrary angles α, β and γ are displayed in Fig. 6. Without loss of generality, let the plane be fixed in the inertial frame $\mathcal{I}$ with the origin O somewhere on the plane. The tangential vectors of the plane are $\mathbf{i}_x$ and $\mathbf{i}_y$, the normal vector is $\mathbf{i}_z$. The body-fixed reference frame $\mathcal{B}$ is attached to the convex object at point B. In the initial configuration, all four frames are aligned as displayed in Fig. 6a. The object's translation is described by the position of B. Its orientation follows from one passive[10] rotation of frame $\mathcal{K}$ and two active rotations of frame $\mathcal{B}$ with respect to $\mathcal{I}$. The passive rotation of $\mathcal{K}$ with respect to $\mathcal{J}$ by the angle β around $\mathbf{j}_z$ defines the axis of rotation for the subsequent active rotation, cf. Fig. 6b. The first active transformation rotates $\mathcal{B}$ relative to $\mathcal{J}$ around $\mathbf{k}_y$ by the angle α as displayed in Fig. 6c. The second active transformation rotates $\mathcal{J}$—and $\mathcal{K}$, $\mathcal{B}$ which are defined relative to $\mathcal{J}$—around $\mathbf{i}_z$ by the angle γ, cf. Fig. 6d.

The transformation $\mathrm{Q}^{\mathcal{IB}}(\alpha, \beta, \gamma)$ from the initial orientation in Fig. 6a to the final orientation in Fig. 6d is thus put together as follows. The rotation of $\mathcal{K}$ relative to $\mathcal{J}$ around the $\mathbf{j}_z$-axis is displayed in Fig. 6b and results in the rotation matrix

$$\mathrm{Q}^{\mathcal{JK}}(\beta) = \begin{bmatrix} \cos(\beta) & -\sin(\beta) & 0 \\ \sin(\beta) & \cos(\beta) & 0 \\ 0 & 0 & 1 \end{bmatrix}, \tag{63}$$

the rotation of $\mathcal{B}$ relative to $\mathcal{J}$ around the $\mathbf{k}_y$-axis is displayed in Fig. 6c and results in the transformation matrix

$$\mathrm{Q}^{\mathcal{JB}}(\alpha, \beta) = \begin{bmatrix} 1 - 2\sin^2\left(\frac{\alpha}{2}\right)\cos^2(\beta) & -\sin^2\left(\frac{\alpha}{2}\right)\sin(2\beta) & \sin(\alpha)\cos(\beta) \\ -\sin^2\left(\frac{\alpha}{2}\right)\sin(2\beta) & 1 - 2\sin^2\left(\frac{\alpha}{2}\right)\sin^2(\beta) & \sin(\alpha)\sin(\beta) \\ -\sin(\alpha)\cos(\beta) & -\sin(\alpha)\sin(\beta) & \cos(\alpha) \end{bmatrix}, \tag{64}$$

[10] An active rotation changes the orientation of the object, whereas a passive rotation changes only the orientation of some reference frame relative to the object.

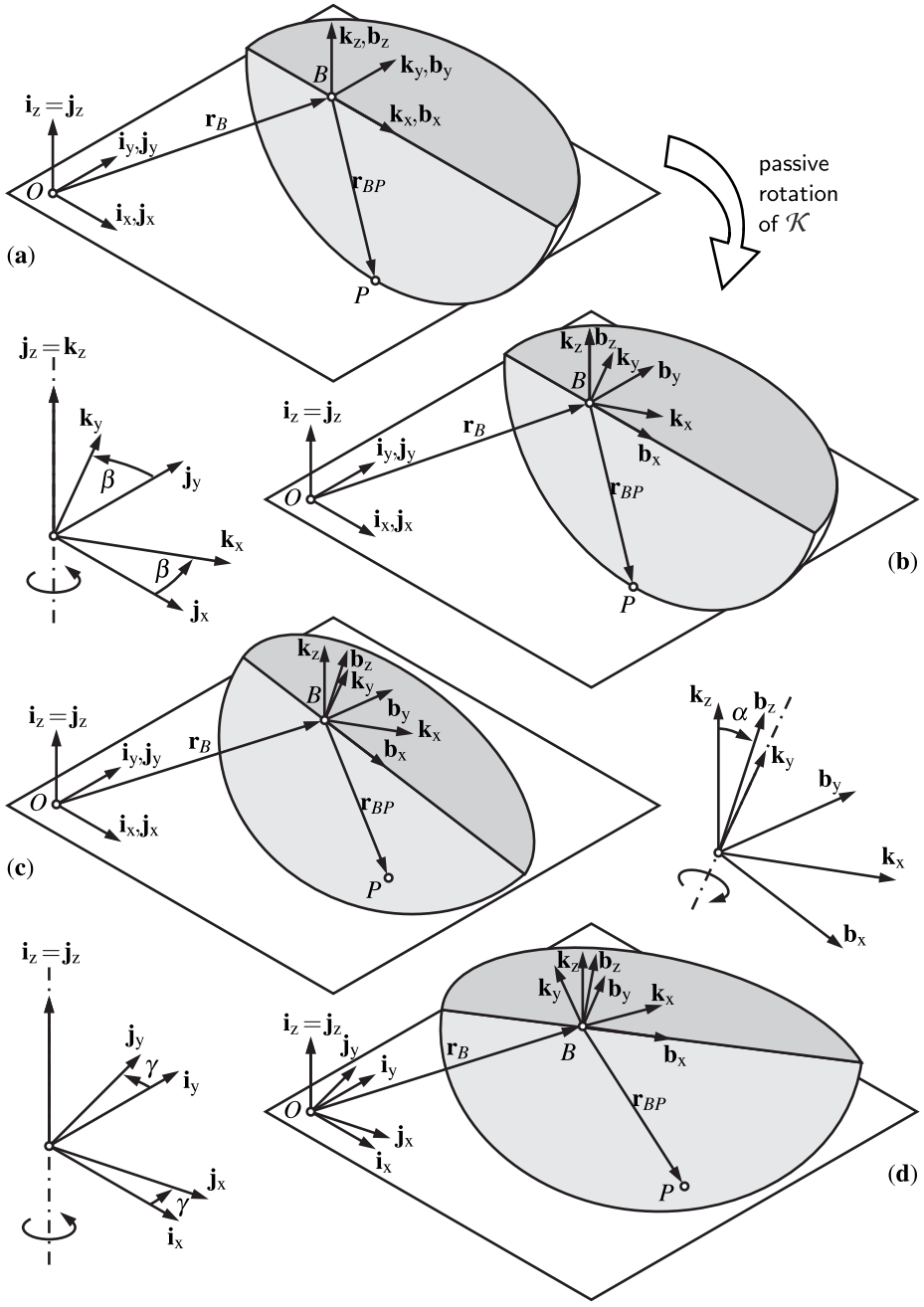

Figure 6: Position and orientation of the object (only partially visualized, slice planes in gray) relative to the plane. The object's position is described by $\mathbf{r}_B$ relative to the origin O. The contact point $P = P(\alpha, \beta, \gamma)$ depends on the object's orientation and is displayed accordingly. The orientation of the body-fixed frame $\mathcal{B}$ relative to the inertial frame $\mathcal{I}$ follows from two consecutive (active) rotations:
(**a**) Initial configuration with equal alignment of $\mathcal{I}$, $\mathcal{J}$, $\mathcal{K}$ and $\mathcal{B}$. (**b**) A passive rotation of $\mathcal{K}$ relative to $\mathcal{J}$ by the angle β around $\mathbf{j}_z$ (no change of the object's orientation). (**c**) First active rotation of $\mathcal{B}$ relative to $\mathcal{J}$ by the angle α around $\mathbf{k}_y$. (**d**) Second active rotation of $\mathcal{J}$—and $\mathcal{K}$, $\mathcal{B}$ which are defined relative to $\mathcal{J}$—by the angle γ around $\mathbf{i}_z$. This results in the final orientation (P is concealed by the object in Figs. (**c**) and (**d**)).

and the rotation of $\mathcal{J}$ relative to $\mathcal{I}$ around the $\mathbf{i}_z$-axis is displayed in Fig. 6d and results in the transformation matrix

$$\mathrm{Q}^{\mathcal{IJ}}(\gamma) = \begin{bmatrix} \cos(\gamma) & -\sin(\gamma) & 0 \\ \sin(\gamma) & \cos(\gamma) & 0 \\ 0 & 0 & 1 \end{bmatrix} . \tag{65}$$

The object's orientation relative to $\mathcal{I}$ is thus

$$\begin{aligned} \mathrm{Q}^{\mathcal{IB}}(\alpha,\beta,\gamma) &= \mathrm{Q}^{\mathcal{IJ}}(\gamma)\, \mathrm{Q}^{\mathcal{JB}}(\alpha,\beta) \\ &= \begin{bmatrix} \cos^2\!\left(\frac{\alpha}{2}\right)\cos(\gamma) - \sin^2\!\left(\frac{\alpha}{2}\right)\cos(2\beta+\gamma) & -\cos^2\!\left(\frac{\alpha}{2}\right)\sin(\gamma) - \sin^2\!\left(\frac{\alpha}{2}\right)\sin(2\beta+\gamma) & \sin(\alpha)\cos(\beta+\gamma) \\ \cos^2\!\left(\frac{\alpha}{2}\right)\sin(\gamma) - \sin^2\!\left(\frac{\alpha}{2}\right)\sin(2\beta+\gamma) & \cos^2\!\left(\frac{\alpha}{2}\right)\cos(\gamma) + \sin^2\!\left(\frac{\alpha}{2}\right)\cos(2\beta+\gamma) & \sin(\alpha)\sin(\beta+\gamma) \\ -\sin(\alpha)\cos(\beta) & -\sin(\alpha)\sin(\beta) & \cos(\alpha) \end{bmatrix} \end{aligned} \tag{66}$$

and its six degrees of freedom are described by the generalized coordinates $\mathbf{q} = \left[x_B^{\mathcal{I}}(t), y_B^{\mathcal{I}}(t), z_B^{\mathcal{I}}(t), \alpha(t), \beta(t), \gamma(t)\right]^T$. A proof for the completeness of this definition, meaning that the transformation to any three-dimensional orientation is possible, is given in Appendix B. The object's angular velocity relative to the inertial frame is

$$\boldsymbol{\omega}^{\mathcal{IB}} = \underbrace{\left(-\sin(\alpha)\dot{\beta}\right)}_{\omega_x^{\mathcal{K}}} \mathbf{k}_x + \underbrace{\dot{\alpha}}_{\omega_y^{\mathcal{K}}} \mathbf{k}_y + \underbrace{\left((1-\cos(\alpha))\dot{\beta} + \dot{\gamma}\right)}_{\omega_z^{\mathcal{K}}} \mathbf{k}_z , \tag{67}$$

which can be derived from $\mathrm{Q}^{\mathcal{IB}}(\alpha,\beta,\gamma)$.

As is evident from Fig. 6, the position of the potential contact point P relative to B depends only on the orientations α, β and γ. Assuming that P is unique, this relative position $\mathbf{r}_{BP}(\alpha,\beta,\gamma)$ follows from a scalar function $g_B : \mathbb{S}^2 \to \mathbb{R}$. The function $g_B(\alpha,\beta)$ with the spherical coordinates $\alpha \in [0,\pi]$ and $\beta \in [0,2\pi)$ is a parameterization of the distance between B and P in the direction of the plane's normal $\mathbf{i}_z$ (cf. Eq. (72)). It is independent of γ which corresponds to a rotation of the object around $\mathbf{i}_z$ and its specific form depends on the shape of the object's boundary which must be 2π-periodic with respect to β. There are two coordinate singularities at $\alpha = 0$ and $\alpha = \pi$, which correspond to the two poles of the spherical coordinates $\{\alpha,\beta\}$. P being unique means that there are no straight line segments anywhere on the boundary meaning its curvature in any direction is non-zero everywhere.

Analogously to the approach in [54], the dependency of $\mathbf{r}_{BP}(\alpha,\beta,\gamma)$ on $g_B(\alpha,\beta)$ can be derived from the special case of a rolling contact between the object and the plane. The system is then reduced to three degrees of freedom as the translation of the contact point P is prevented by the rolling conditions. The positions of B and P become

$$\mathbf{r}_B = x_B^{\mathcal{K}} \mathbf{k}_x + y_B^{\mathcal{K}} \mathbf{k}_y + z_B^{\mathcal{K}} \mathbf{k}_z , \tag{68}$$

$$\mathbf{r}_P = x_P^{\mathcal{K}} \mathbf{k}_x + y_P^{\mathcal{K}} \mathbf{k}_y , \tag{69}$$

$$\begin{aligned} \mathbf{r}_{BP} &= \mathbf{r}_P - \mathbf{r}_B \\ &= x_{BP}^{\mathcal{K}} \mathbf{k}_x + y_{BP}^{\mathcal{K}} \mathbf{k}_y + z_{BP}^{\mathcal{K}} \mathbf{k}_z , \end{aligned} \tag{70}$$

and thus

$$z_{BP}^{\mathcal{K}} = -z_B^{\mathcal{K}} . \tag{71}$$

The definition of

$$z_B^{\mathcal{K}}(\alpha,\beta) := g_B(\alpha,\beta) \tag{72}$$

for the special case of rolling yields

$$z_{BP}^{\mathcal{K}}(\alpha,\beta) = -g_B(\alpha,\beta) . \tag{73}$$

The dependency of $x_{BP}^{\mathcal{K}}(\alpha,\beta)$ and $y_{BP}^{\mathcal{K}}(\alpha,\beta)$ on $g_B(\alpha,\beta)$ follows from the velocity of B for an arbitrary angular velocity $\boldsymbol{\omega}^{\mathcal{IB}}$. In general, the velocity is[11]

$$\begin{aligned}\mathbf{v}_B &= \dot{x}_B^{\mathcal{K}}\,\mathbf{k}_\mathrm{x} + \dot{y}_B^{\mathcal{K}}\,\mathbf{k}_\mathrm{y} + \dot{z}_B^{\mathcal{K}}(\alpha,\beta)\,\mathbf{k}_\mathrm{z}\\ &= \dot{x}_B^{\mathcal{K}}\,\mathbf{k}_\mathrm{x} + \dot{y}_B^{\mathcal{K}}\,\mathbf{k}_\mathrm{y} + \left(\partial_\alpha z_B^{\mathcal{K}}(\alpha,\beta)\dot{\alpha} + \partial_\beta z_B^{\mathcal{K}}(\alpha,\beta)\dot{\beta}\right)\mathbf{k}_\mathrm{z}\\ &= \dot{x}_B^{\mathcal{K}}\,\mathbf{k}_\mathrm{x} + \dot{y}_B^{\mathcal{K}}\,\mathbf{k}_\mathrm{y} + \left(\partial_\alpha g_B(\alpha,\beta)\dot{\alpha} + \partial_\beta g_B(\alpha,\beta)\dot{\beta}\right)\mathbf{k}_\mathrm{z}\,,\end{aligned} \tag{74}$$

and the rolling condition

$$\dot{\mathbf{r}}_P =: \mathbf{v}_P = \mathbf{0} \tag{75}$$

results in

$$\begin{aligned}\mathbf{v}_B &= \mathbf{v}_P + \boldsymbol{\omega}^{\mathcal{IB}} \times \mathbf{r}_{PB}\\ &= \mathbf{r}_{BP} \times \boldsymbol{\omega}^{\mathcal{IB}}\\ &= \left(g_B(\alpha,\beta)\dot{\alpha} + (1-\cos(\alpha))\,y_{BP}^{\mathcal{K}}\dot{\beta} + y_{BP}^{\mathcal{K}}\dot{\gamma}\right)\mathbf{k}_\mathrm{x}\\ &\quad + \left(\left(g_B(\alpha,\beta)\sin(\alpha) - (1-\cos(\alpha))\,x_{BP}^{\mathcal{K}}\right)\dot{\beta} - x_{BP}^{\mathcal{K}}\dot{\gamma}\right)\mathbf{k}_\mathrm{y}\\ &\quad + \left(x_{BP}^{\mathcal{K}}\dot{\alpha} + \sin(\alpha)y_{BP}^{\mathcal{K}}\dot{\beta}\right)\mathbf{k}_\mathrm{z}\,.\end{aligned} \tag{76}$$

The comparison of the coefficient in $\mathbf{k}_\mathrm{z}$-direction in Eqs. (74) and (76) yields

$$\mathbf{r}_{BP} = \partial_\alpha g_B(\alpha,\beta)\,\mathbf{k}_\mathrm{x} + (\sin(\alpha))^{-1}\,\partial_\beta g_B(\alpha,\beta)\,\mathbf{k}_\mathrm{y} - g_B(\alpha,\beta)\,\mathbf{k}_\mathrm{z}\,. \tag{77}$$

Defining $\varphi = -\alpha$, $\theta = \beta$, $\mathbf{e}_\varphi = -\mathbf{k}_\mathrm{x}$, $\mathbf{e}_\theta = \mathbf{k}_\mathrm{y}$ and $\mathbf{e}_\mathrm{n} = -\mathbf{k}_\mathrm{z}$ shows that Eq. (77) is equal to the regular case of the normal parameterization in Eq. (16).

5. Collision detection

As the derivation of the normal parameterization from basic rigid body kinematics in the previous section shows, it allows an explicit collision detection between an object and a planar counterpart. Since the normal vector at the potential contact point on the object is antiparallel to that of the plane according to the common normal concept, only the corresponding angles (φ,θ) have to be determined to evaluate Eq. (16). However, the common normal between two general objects is not known a priori and we have not found any explicit solution to this problem, which is why an iterative calculation is required. The same situation arises in the case of surface representation via implicit functions or via different parameterizations, where common algorithms rely on Newton methods with analytical Jacobians for an efficient solution [4, 6]. However, the specific properties of the normal parameterization allow further, derivative-free approaches. This is demonstrated by a comparison of four different algorithms which are compared in terms of implementation effort, robustness and rate of convergence.

The algorithms I and II are based on a Newton method with an analytical Jacobian for the concept of closest points or on the common normal concept, respectively. Since the respective Jacobians depend on the parameterization of the particular objects, e. g. two ellipsoids, the implementation effort for both approaches is considered to be high. As investigated below, the rate of convergence of both algorithms is quadratic and therefore an accurate solution can be determined very fast. However, the robustness, meaning the convergence to the correct solution, is worse than for the other two algorithms.

To lower the implementation effort, algorithm III is proposed as an alternative approach based on a fixed-point iteration that does not require any derivatives. This algorithm also shows fast convergence, albeit slower than the Newton methods with analytical gradients. However, it is more robust, meaning it converges to the correct solution more often than algorithms I and II. Finally, algorithm IV combines algorithms III and II, which results in a method with very high robustness and fast convergence. However, the implementation effort is also very high, since both methods have to be implemented.

[11] Here, $\dot{x}_B^{\mathcal{K}}$ and $\dot{y}_B^{\mathcal{K}}$ do not represent the time derivatives of $x_B^{\mathcal{K}}$ and $y_B^{\mathcal{K}}$, because $\mathcal{K}$ is not an inertial reference frame. Instead, the two variables express the respective component of the velocity of B relative to the inertial frame after proper transformation to $\mathcal{K}$.

5.1. Collision detection algorithms

All four algorithms are derived for collision detection between two objects. One object is designated as the master object with reference point and base $\mathcal{M} = \{M, (\mathbf{m}_\mathrm{x}, \mathbf{m}_\mathrm{y}, \mathbf{m}_\mathrm{z})\}$; the second object is introduced as slave with reference point and base $\mathcal{S} = \{S, (\mathbf{s}_\mathrm{x}, \mathbf{s}_\mathrm{y}, \mathbf{s}_\mathrm{z})\}$. The relative distance and orientation are given by $\mathbf{r}_{MS}$ and $\mathrm{Q}^{\mathcal{MS}}$ and the corresponding generating potentials are $g_M(\varphi_M, \theta_M)$ and $g_S(\varphi_S, \theta_S)$. The master object's outer normal vector is

$$\mathbf{n}_M(\varphi_M, \theta_M) = \sin\varphi_M \cos\theta_M \, \mathbf{m}_\mathrm{x} + \sin\varphi_M \sin\theta_M \, \mathbf{m}_\mathrm{y} + \cos\varphi_M \, \mathbf{m}_\mathrm{z} \tag{78}$$

and the slave variables are

$$\varphi_S = \arccos(-\mathbf{n}_M \cdot \mathbf{s}_\mathrm{z}) \,, \tag{79a}$$

$$\theta_S = \operatorname{arctan2}(-\mathbf{n}_M \cdot \mathbf{s}_\mathrm{y}, -\mathbf{n}_M \cdot \mathbf{s}_\mathrm{x}) \tag{79b}$$

since the outer normal vectors are antiparallel at the potential contact point (arctan2 is defined in Appendix A). Therefore, any direction given by $(\varphi_M, \theta_M) \mapsto \mathbf{n}_M(\varphi_M, \theta_M)$ defines a point P given by $\mathbf{r}_{MP}(\varphi_M, \theta_M)$ on the boundary of the master object via Eq. (16) and a corresponding point Q given by $\mathbf{r}_{SQ}(\varphi_S, \theta_S)$ on the slave object. The connection of both points is

$$\mathbf{r}_{PQ}(\varphi_M, \theta_M) = \mathbf{r}_{MS} - \mathbf{r}_{MP}(\varphi_M, \theta_M) + \mathbf{r}_{SQ}(\varphi_S(\varphi_M, \theta_M), \theta_S(\varphi_M, \theta_M)) \,. \tag{80}$$

Algorithm I is based on the concept of closest points with the (squared) distance functional

$$\Phi_\mathrm{I}(\varphi_M, \theta_M) = \frac{1}{2} \left(\mathbf{r}_{PQ} \cdot \mathbf{r}_{PQ} \right) \,. \tag{81}$$

The optimization problem

$$\min_{(\varphi_M, \theta_M) \in \mathbb{S}^2} \Phi_\mathrm{I}(\varphi_M, \theta_M) \tag{82}$$

yields the Newton iteration

$$\begin{bmatrix} \varphi_{M,i+1} \\ \theta_{M,i+1} \end{bmatrix} = \begin{bmatrix} \varphi_{M,i} \\ \theta_{M,i} \end{bmatrix} - \begin{bmatrix} \partial^2_{\varphi_M} \Phi_\mathrm{I}(\varphi_{M,i}, \theta_{M,i}) & \partial_{\varphi_M} \partial_{\theta_M} \Phi_\mathrm{I}(\varphi_{M,i}, \theta_{M,i}) \\ \partial_{\theta_M} \partial_{\varphi_M} \Phi_\mathrm{I}(\varphi_{M,i}, \theta_{M,i}) & \partial^2_{\theta_M} \Phi_\mathrm{I}(\varphi_{M,i}, \theta_{M,i}) \end{bmatrix}^{-1} \begin{bmatrix} \partial_{\varphi_M} \Phi_\mathrm{I}(\varphi_{M,i}, \theta_{M,i}) \\ \partial_{\theta_M} \Phi_\mathrm{I}(\varphi_{M,i}, \theta_{M,i}) \end{bmatrix} \,. \tag{83}$$

Algorithm II is adapted from [6, Eq. (18)] and based on the common normal concept that requires $\mathbf{n}_M(\varphi_M, \theta_M)$ and $\mathbf{r}_{PQ}(\varphi_M, \theta_M)$ to be parallel. Consequently, the tangential components

$$\mathbf{\Phi}_\mathrm{II}(\varphi_M, \theta_M) = \begin{bmatrix} \mathbf{r}_{PQ} \cdot \mathbf{e}_{\varphi_\mathrm{M}} \\ \mathbf{r}_{PQ} \cdot \mathbf{e}_{\theta_\mathrm{M}} \end{bmatrix} \tag{84}$$

must vanish yielding the Newton iteration

$$\begin{bmatrix} \varphi_{M,i+1} \\ \theta_{M,i+1} \end{bmatrix} = \begin{bmatrix} \varphi_{M,i} \\ \theta_{M,i} \end{bmatrix} - \begin{bmatrix} \partial_{\varphi_M} \mathbf{\Phi}_\mathrm{II}(\varphi_{M,i}, \theta_{M,i}) & \partial_{\theta_M} \mathbf{\Phi}_\mathrm{II}(\varphi_{M,i}, \theta_{M,i}) \end{bmatrix}^{-1} \mathbf{\Phi}_\mathrm{II}(\varphi_{M,i}, \theta_{M,i}) \,. \tag{85}$$

The necessary derivatives for both algorithms I and II are quite cumbersome to calculate and are therefore not explicitly given. Due to this fact, however, a fixed-point iteration is developed that does not require any derivatives. An intuitive choice for this fixed-point iteration is the variant shown in Fig 7a. Starting from the normal vector $\mathbf{n}_{M,i}$, the connection $\mathbf{r}_{PQ}(\varphi_{M,i}, \theta_{M,i})$ is normalized and assigned as $\mathbf{n}_{M,i+1} = \mathbf{r}_{PQ,i} / \|\mathbf{r}_{PQ,i}\|_2$ for the next iteration step. The common normal at the points with the closest points is a fixed point of this iteration rule. However, the iteration rule itself proves to be unstable, which can also be observed in Fig 7a. Here, the connection of the reference points $\mathbf{r}_{MS}$ is selected as initialization $\mathbf{n}_{M,0} = \mathbf{r}_{MS} / \|\mathbf{r}_{MS}\|_2$. According to the iteration rule, $\mathbf{n}_{M,1}$ and the corresponding points P_1 and Q_1 are determined. However, the direction of $\mathbf{r}_{PQ,1}$ (not depicted) differs more from $\mathbf{n}_{M,1}$ than the initialization $\mathbf{n}_{M,0}$. The iteration rule diverges, although it was initialized close to the fixed point. It is therefore not suitable to determine the common normal vector.

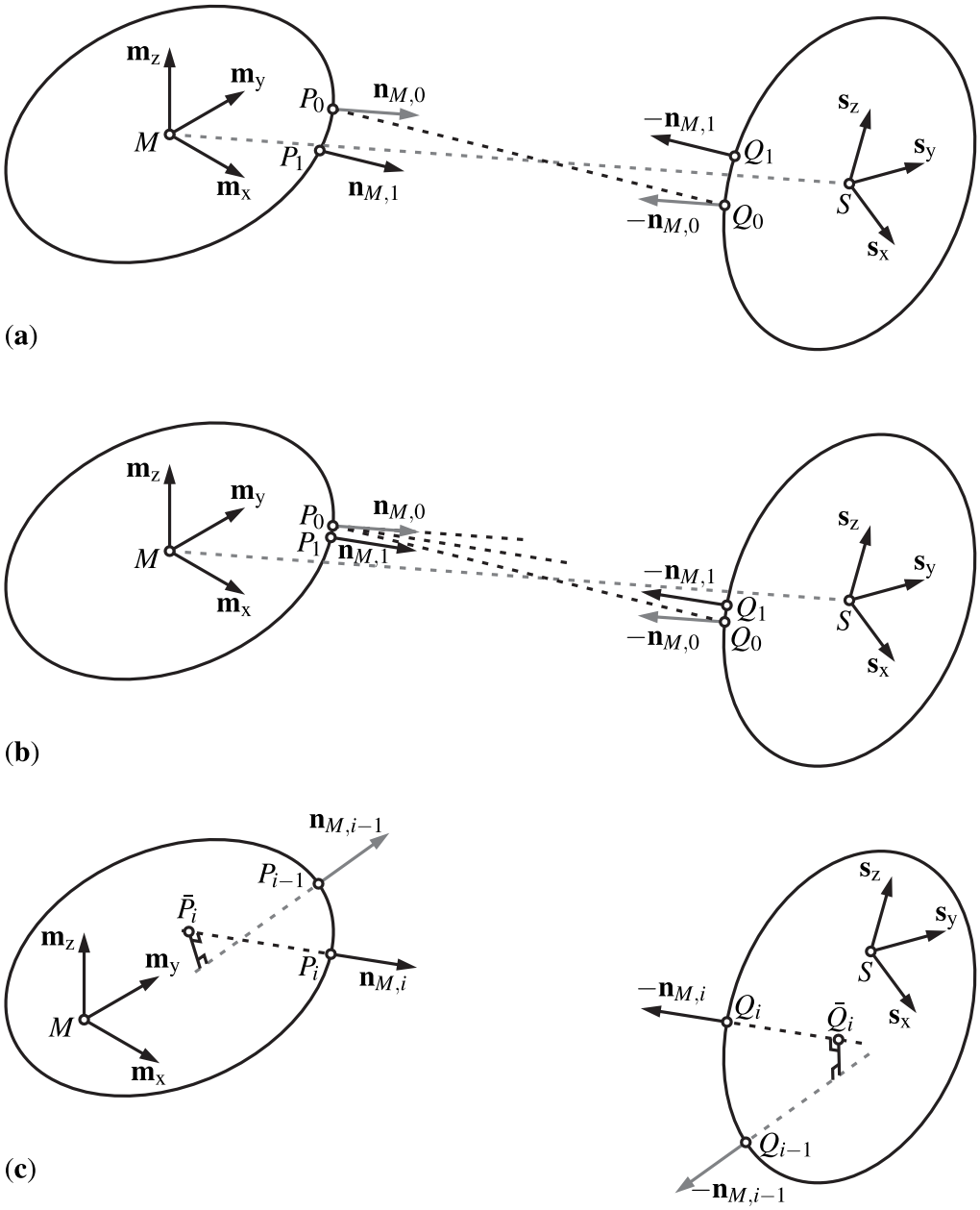

Figure 7: Three fixed-point iteration schemes: **(a)** unstable scheme where $\mathbf{n}_{M,i+1}$ is parallel to $\mathbf{r}_{PQ,i}$. **(b)** slow, mostly stable scheme where $\mathbf{n}_{M,i+1}$ is the mean direction between $\mathbf{n}_{M,i}$ and $\mathbf{r}_{PQ,i}$. **(c)** fast, stable scheme where $\mathbf{n}_{M,i+1}$ is parallel to $\mathbf{r}_{\bar{P}\bar{Q},i}$.

A modification with which the fixed-point iteration can be improved is shown in Fig 7b. Instead of just using the connection $\mathbf{r}_{PQ,i}$ to determine $\mathbf{n}_{M,i+1}$, the mean value

$$\mathbf{n}_{M,i+1} = \frac{\mathbf{n}_{M,i} + (\mathbf{r}_{PQ,i}/\|\mathbf{r}_{PQ,i}\|_2)}{\left\|\mathbf{n}_{M,i} + (\mathbf{r}_{PQ,i}/\|\mathbf{r}_{PQ,i}\|_2)\right\|_2} \tag{86}$$

is used. This iteration rule also has the common normal vector as a fixed point. It has been observed that this iteration rule does converge, yet very slowly and not very reliably. It is therefore unsuitable for the desired application.

These observations motivate the development of algorithm III as follows: given the current and previous iteration for the normal vector $\mathbf{n}_{M,i}$, $\mathbf{n}_{M,i-1}$ and the points P_i, P_{i-1}, $\bar{P}_i$ is determined as the point on the line $a_i \in \mathbb{R} \mapsto \mathbf{r}_{MP,i}+a_i\mathbf{n}_{M,i}$ which is closest to the line $a_{i-1} \in \mathbb{R} \mapsto \mathbf{r}_{MP,i-1} + a_{i-1}\mathbf{n}_{M,i-1}$; $\bar{Q}_i$ is defined analogously. Solving for both points yields

$$\mathbf{r}_{P\bar{P},i} = \frac{(\mathbf{n}_{M,i} - (\mathbf{n}_{M,i}\cdot\mathbf{n}_{M,i-1})\,\mathbf{n}_{M,i-1})\cdot(\mathbf{r}_{MP,i} - \mathbf{r}_{MP,i-1})}{(\mathbf{n}_{M,i}\cdot\mathbf{n}_{M,i-1})^2 - 1}\mathbf{n}_{M,i} = \frac{(\mathbf{n}_{M,i} - (\mathbf{n}_{M,i}\cdot\mathbf{n}_{M,i-1})\,\mathbf{n}_{M,i-1})\cdot(\mathbf{r}_{MP,i} - \mathbf{r}_{MP,i-1})}{-(\mathbf{n}_{M,i}\times\mathbf{n}_{M,i-1})\cdot(\mathbf{n}_{M,i}\times\mathbf{n}_{M,i-1})}\mathbf{n}_{M,i}\,, \tag{87a}$$

$$\mathbf{r}_{Q\bar{Q},i} = \frac{(\mathbf{n}_{M,i} - (\mathbf{n}_{M,i}\cdot\mathbf{n}_{M,i-1})\,\mathbf{n}_{M,i-1})\cdot(\mathbf{r}_{SQ,i} - \mathbf{r}_{SQ,i-1})}{(\mathbf{n}_{M,i}\cdot\mathbf{n}_{M,i-1})^2 - 1}\mathbf{n}_{M,i} = \frac{(\mathbf{n}_{M,i} - (\mathbf{n}_{M,i}\cdot\mathbf{n}_{M,i-1})\,\mathbf{n}_{M,i-1})\cdot(\mathbf{r}_{SQ,i} - \mathbf{r}_{SQ,i-1})}{-(\mathbf{n}_{M,i}\times\mathbf{n}_{M,i-1})\cdot(\mathbf{n}_{M,i}\times\mathbf{n}_{M,i-1})}\mathbf{n}_{M,i}\,, \tag{87b}$$

where the denominator is transformed into the cross product expressions to avoid numerical problems due to roundoff errors. The connection from $\bar{P}_i$ to $\bar{Q}_i$

$$\mathbf{r}_{\bar{P}\bar{Q},i} = \mathbf{r}_{MS} - \left(\mathbf{r}_{MP,i} + \mathbf{r}_{P\bar{P},i}\right) + \left(\mathbf{r}_{SQ,i} + \mathbf{r}_{Q\bar{Q},i}\right) \tag{88}$$

is taken as next iteration for the normal vector

$$\mathbf{n}_{M,i+1} = \frac{\mathbf{r}_{\bar{P}\bar{Q},i}}{\left\|\mathbf{r}_{\bar{P}\bar{Q},i}\right\|_2}\,. \tag{89}$$

In contrast to the algorithms I and II, no derivatives are required for algorithm III defined in this way; instead, the values of the previous iteration step are used. To initialize this procedure, the first iteration is calculated via Eq. (86).

Algorithm IV is a combination of algorithms III and II: algorithm III used to initialize the iteration. If the scalar product between two successive iterates for the normal vector is above a certain tolerance ($\mathbf{n}_{M,i}\cdot\mathbf{n}_{M,i-1} > 0.99$), the procedure switches to the Newton iteration via Eq. (85).

5.2. Convergence study

A comparison of all four algorithms in terms of robustness and rate of convergence is conducted using the following benchmark model. Two ellipsoids with the generating potential according to Eq. (51) are considered. The semi-axes of the master and of the slave object are a_M, b_M, c_M and a_S, b_S, c_S, respectively. The offset of the slave object is $\mathbf{r}_{MS} = (a_M + \bar{x}_{MS})\mathbf{m}_\mathrm{x} + (b_M + \bar{y}_{MS})\mathbf{m}_\mathrm{y} + (c_M + \bar{z}_{MS})\mathbf{m}_\mathrm{z}$ and its orientation is given by $\mathrm{Q}^{\mathcal{MS}}$. The parameters $a_M, b_M, c_M, a_S, b_S, c_S, \bar{x}_{MS}, \bar{y}_{MS}, \bar{z}_{MS} \in (0, 1)$ and the rotation matrix $\mathrm{Q}^{\mathcal{MS}}$ are generated randomly. By this choice of parameters it is possible, but not very likely, that the objects penetrate each other ($\approx 2.2\,\%$ of the realizations). This way, the distance between the two objects ranges from very small values to the order of magnitude of the semi-axes. A solution is accepted as successful if

$$\left||\tilde{\mathbf{n}}_M\cdot\mathbf{r}_{PQ}(\tilde{\mathbf{n}}_M)| - \sqrt{\mathbf{r}_{PQ}(\tilde{\mathbf{n}}_M)\cdot\mathbf{r}_{PQ}(\tilde{\mathbf{n}}_M)}\right| < \sqrt{\epsilon} \tag{90}$$

and

$$\mathbf{r}_{PQ}(\tilde{\mathbf{n}}_M)\cdot\mathbf{r}_{PQ}(\tilde{\mathbf{n}}_M) < \mathbf{r}_{PQ}(\mathbf{n}_{M,0})\cdot\mathbf{r}_{PQ}(\mathbf{n}_{M,0}) \tag{91}$$

where $\tilde{\mathbf{n}}_M$ is the best result of any of the four algorithms and $\epsilon \approx 2.2\cdot 10^{-16}$ is the machine precision. A set of 10^5 realizations is randomly generated and all algorithms are applied to every realization with an upper limit of 10^3 iterations. To investigate the algorithms' robustness and convergence, two studies are performed with different initializations: study A with $\mathbf{n}_{M,0} = \mathbf{r}_{MS}/\|\mathbf{r}_{MS}\|_2$ and study B with $\mathbf{n}_{M,0}$ = random.

Table 1: Percentage of successful iterations and aspect ratio of failed iterations for realizations with and without penetration for all four algorithms for an upper limit of 10^3 iterations.

		successful iterations		minimum maximum aspect ratio of any failed iteration	
	Algorithm	study A $\mathbf{n}_{M,0} = \mathbf{r}_{MS}/\|\mathbf{r}_{MS}\|_2$	study B $\mathbf{n}_{M,0}$ = random	study A $\mathbf{n}_{M,0} = \mathbf{r}_{MS}/\|\mathbf{r}_{MS}\|_2$	study B $\mathbf{n}_{M,0}$ = random
without penetration	I	55.2 %	16.5 %	1.3	1.0
	II	92.8 %	47.5 %	2.0	1.1
	III	99.9 %	99.7 %	18.2	3.4
	IV	99.2 %	99.1 %	6.2	3.4
with penetration	I	48.9 %	18.4 %	1.5	1.3
	II	77.7 %	47.3 %	1.5	1.2
	III	97.8 %	96.4 %	4.1	3.6
	IV	96.4 %	95.2 %	3.6	2.2

The success rate of both studies are summarized in Table 1. In realizations without penetration which are initialized with the good estimate $\mathbf{n}_{M,0} = \mathbf{r}_{MS}/\|\mathbf{r}_{MS}\|_2$ (study A), algorithm I converges only in about half of the realizations, algorithm II succeeds in over 90 % and algorithms III and IV show a success rate of over 99 %. Algorithm III is the most robust algorithm in this comparison and shows a failure rate of ≈ 0.1 %. Although algorithm IV is initialized by the same procedure until two successive iterates for the normal vector are very similar ($\mathbf{n}_{M,i} \cdot \mathbf{n}_{M,i-1} > 0.99$), it still diverges from the correct solution in some realizations and shows a worse failure rate of ≈ 0.8 %. The performance of algorithms I and II drops significantly in study B with random initialization. Algorithm II succeeds in about half of the realizations which is an expected result since the minimization of the tangential components of $\mathbf{r}_{PQ}$ does not favor convergence to the minimum distance solution over the maximum distance solution. Algorithms III and IV show only very small losses of performance of less than 0.2 %. Algorithm III is again the most robust procedure with a failure rate of less than 0.3 %.

If there is large penetration between both objects, the contact point is no longer well defined by the common normal concept.[12] If there is only small penetration, the common normal concept yields the point of maximum penetration and all may still converge. For realizations with penetration, the success rate is still best for algorithms III and IV, albeit slightly lower in both study A and study B which we attribute to the relatively small number of realizations with large penetration. However, there is a significant drop of ≈ 15 % in the success rate for algorithm II in study A indicating that its performance is particularly sensitive to penetration of the objects; a characteristic that cannot be observed for the other algorithms.

Whenever algorithms III or IV fail to converge to the correct solution, there is either large penetration or the aspect ratio $\max\{a, b, c\}/\min\{a, b, c\}$ of one or both ellipsoids is very large. If the aspect ratio is large, there are lines on the boundary surface with very small curvature (almost straight) where small changes of the normal vector result in large changes of the corresponding boundary point P or Q. Thus the solution in each iteration step is very sensitive to the normal vector and we consider the problem to be badly conditioned. In study A, algorithm III converges for aspect ratios below 18.2, followed by algorithm IV with 6.2; in study B with random initialization, these numbers drop to 3.4. Since the convergence of algorithms I and II is much worse, the minimum aspect ratios are significantly lower. Aspect ratios below 2.0 indicate that the reason for the failure of convergence lies elsewhere.

The necessary number of iterations to achieve a requested accuracy for a certain percentage of all realizations is displayed in Table 2. Algorithm I not only has the lowest success rate, but also requires by far the highest number of iterations to achieve a certain accuracy; it is therefore the worst examined algorithm. Algorithms II and IV require more or less the same number of iterations, while algorithm III requires about twice as many. However, the computation times are difficult to compare, since algorithm III only requires function evaluations, but no derivatives, while algorithm II requires the calculation or evaluation of the analytical Jacobian and algorithm IV is a combination of

[12] The common normal concept is unsuitable if e. g. one object completely interpenetrates the other and exits on the other side.

Table 2: Necessary number of iterations to achieve a requested accuracy for a certain percentage of all realizations.

		Necessary number of iterations to achieve requested accuracy for percentage of all realizations														
		study A $\mathbf{n}_{M,0} = \mathbf{r}_{MS}/\|\mathbf{r}_{MS}\|_2$							study B $\mathbf{n}_{M,0}$ = random						
Algorithm	Accuracy	40%	50%	60%	70%	80%	90%	95%	40%	50%	60%	70%	80%	90%	95%
I	10^{-4}	10	27												
	10^{-6}	15	43												
	10^{-8}	21	59												
	10^{-10}	26	75												
	10^{-12}	32	91												
	10^{-14}	37	108												
II	10^{-4}	3	3	3	3	4	6		8						
	10^{-6}	3	3	4	4	5	7		9						
	10^{-8}	4	4	4	4	5	7		9						
	10^{-10}	4	4	4	5	5	8		9						
	10^{-12}	4	4	5	5	6	8		10						
	10^{-14}	4	5	5	5	6	8		10						
III	10^{-4}	5	5	6	6	7	8	10	6	7	7	8	9	10	12
	10^{-6}	6	7	8	8	9	11	12	8	8	9	9	10	12	14
	10^{-8}	8	8	9	9	10	12	14	9	10	10	11	12	13	15
	10^{-10}	9	9	10	11	11	13	15	10	11	11	12	13	15	17
	10^{-12}	10	10	11	11	12	14	16	11	11	12	13	14	15	17
	10^{-14}	10	11	11	12	13	14	16	12	12	13	13	14	16	18
IV	10^{-4}	3	4	4	4	5	5	6	5	5	5	6	6	7	8
	10^{-6}	4	4	4	5	5	6	7	5	6	6	6	7	8	9
	10^{-8}	4	5	5	5	6	6	7	6	6	6	7	7	8	9
	10^{-10}	5	5	5	5	6	7	7	6	6	7	7	7	8	9
	10^{-12}	5	5	5	6	6	7	8	6	7	7	7	8	9	10
	10^{-14}	5	5	6	6	6	7	8	6	7	7	7	8	9	10

both. Different computation times per iteration step may reduce or further increase this difference, depending on the complexity of the objects' generating potentials and their derivatives. Since a thorough study requires generating potentials of further objects that have not yet been found, a meaningful benchmark and a comparison to other approaches from the literature remain for future work.

In this convergence study with two ellipsoids, algorithm III shows the best performance in terms of robustness and which is measured by the success rate and its dependence on the aspect ratio. As expected, the performance of all algorithms is best if a good initialization (study A) is used. The robustness of algorithm IV is slightly worse than that of algorithm III; the success rate is a little worse, which is probably due to poorer convergence for high aspect ratios, cf. Table 1. Algorithm III requires more iteration steps than algorithm IV, however it is easier to implement and the computation time per iteration step is difficult to compare. Algorithms I and II exhibit a bad success rate and are not discussed further.

6. Case study

The application of the normal parameterization for collision detection in a multibody simulation is demonstrated with a case study of two ellipsoids that are falling into a rectangular box with inclined walls. The focus is on the

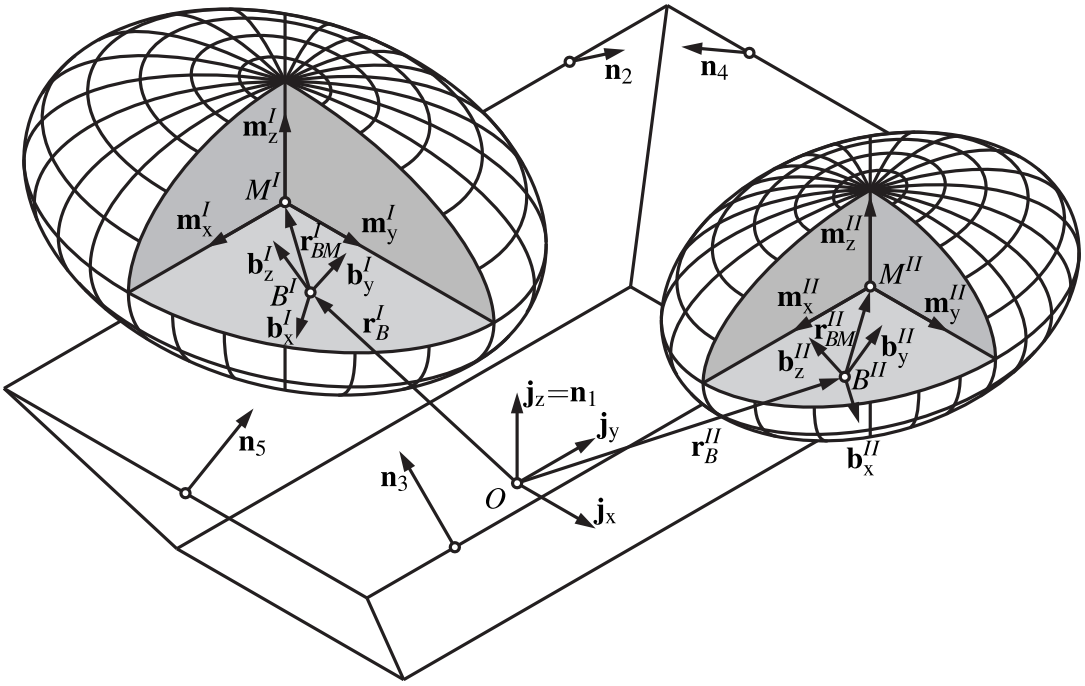

Figure 8: Ellipsoid objects I and II in box with inclined walls.

kinematics of the contact detection problem and the use of the principal curvatures in the interaction force law. The two objects are referenced by the superscripts I and II; if an expression is valid for both objects and this is clear from the context, the superscript is omitted. The following assumptions and simplifications are used: (i) the two objects are ellipsoids with geometrical center M, body-fixed reference frame $\mathcal{M} = \{M, (\mathbf{m}_x, \mathbf{m}_y, \mathbf{m}_z)\}$, semi-axes a, b, c and generating potential via Eq. (51); (ii) the center of mass B and the principal axes of the inertial tensor $(\mathbf{b}_x, \mathbf{b}_y, \mathbf{b}_z)$ do not coincide with frame $\mathcal{M}$ at the geometrical center M; (iii) the objects are falling into a box with flat ground and four flat walls which is fixed in the inertial frame $\mathcal{J} = \{O, (\mathbf{j}_x, \mathbf{j}_y, \mathbf{j}_z)\}$; (iv) the interaction force between any object and the box or between the objects is a combination of an elastic restoring force in normal direction and a dissipative force which depends on the relative velocity.

For both objects the shape of an ellipsoid is chosen, because apart from a sphere it is described by the simplest generating potential and only three parameters have to be specified for each object. The difference between frames $\mathcal{M}$ and $\mathcal{B} = \{B, (\mathbf{b}_x, \mathbf{b}_y, \mathbf{b}_z)\}$ is introduced to illustrate the ease of implementation of the normal parameterization once the generating potential g_M of a geometry with respect to any point M is available. The box consists of five planes with constant normal vectors, which allows a direct calculation of the respective potential contact points. In contrast to a single horizontal plane, the box with inclined walls restricts the possible configuration space and leads to a high number of collisions between the two objects. The model proposed by Flores et al. [41] is used to describe the interaction force in normal direction at every contact point since it requires curvature information like the Hertz contact and at the same time introduces dissipation. For discussions regarding some of the limitations of this model we refer to [42, 43, 44, 45]. The normal force model is combined with a tanh-approximation of Coulomb friction to allow for combined slipping and rolling of the object. This approximation of dry friction is chosen for its simplicity and its favorable numerical properties [51, 52, 53]. The interaction force that follows from this combination of forces in normal and tangential direction is chosen to highlight the use of curvature information and to avoid common problems of rigid contacts, cf. [64]; any dissipation due to drilling or rolling motions is neglected. This simplification is appropriate for the present case study since more physical interaction laws for this type of non-holonomic rolling contact as for example proposed in [42, 46] are much more complicated and distract from the actual focus of this manuscript: the introduction of the normal parameterization and its application for collision detection.

The system under consideration is depicted in Fig. 8. All relationships are specified for object I and can be

transferred analogously to object II. The position and velocity of the object's center of mass B^I relative to the origin O are

$$\mathbf{r}_B^I = x_B^I(t)\,\mathbf{j}_\mathrm{x} + y_B^I(t)\,\mathbf{j}_\mathrm{y} + z_B^I(t)\,\mathbf{j}_\mathrm{z}\,, \tag{92a}$$

$$\mathbf{v}_B^I = \dot{x}_B^I(t)\,\mathbf{j}_\mathrm{x} + \dot{y}_B^I(t)\,\mathbf{j}_\mathrm{y} + \dot{z}_B^I(t)\,\mathbf{j}_\mathrm{z}\,, \tag{92b}$$

and the orientation of frame $\mathcal{B}^I$ relative to the inertial frame $\mathcal{J}$ is described by Tait–Bryan angles $\{\alpha^I(t), \beta^I(t), \gamma^I(t)\}$ which give the rotation matrix $\mathrm{Q}^{\mathcal{JB},I}$ via Eq. (C.1) and the angular velocity $\boldsymbol{\omega}^I$ via Eq. (C.2). Tait-Bryan angles are introduced to derive the equations of motion below as a set of ordinary differential equations in minimal coordinates instead of differential algebraic equations which follow for other parameterization like e.g. Euler parameters; their well known coordinate singularities are avoided by switching between two sets of coordinates as detailed in Appendix C.

The relation between frames $\mathcal{M}^I$ and $\mathcal{B}^I$ is described by the distance $\mathbf{r}_{BM}^I$ and the transformation matrix $\mathrm{Q}^{\mathcal{BM},I}$. The five planes which make up the box are defined by $\mathbf{n}_j \cdot \mathbf{r} = d_j$, $j = 1 \ldots 5$. Object I is subjected to gravity $\mathbf{g} = -g\,\mathbf{j}_\mathrm{z}$ and interaction forces $\mathbf{F}_j^I$ with all planes and $\mathbf{F}_{II}^I$ with object II. The interaction forces $\mathbf{F}_j^I$ act at the (potential) contact points P_j^I which follow directly from Eq. (78) and (79); the (potential) contact point P_{II}^I for the interaction force $\mathbf{F}_{II}^I$ with object II is determined iteratively via algorithm III from Section 5.1. The principal curvatures $\kappa_{1/2,j}^I, \kappa_{1/2,II}^I$ and the corresponding curvature directions $\mathbf{c}_{1/2,j}^I, \mathbf{c}_{1/2,II}^I$ follow directly from Eqs. (26) and (27) and the positions and velocities of all potential contact points are

$$\mathbf{r}_{P,j}^I = \mathbf{r}_B^I + \mathbf{r}_{BM}^I + \mathbf{r}_{MP,j}^I\,, \qquad \mathbf{v}_{P,j}^I = \mathbf{v}_B^I + \boldsymbol{\omega}^I \times \left(\mathbf{r}_{BM}^I + \mathbf{r}_{MP,j}^I\right)\,, \tag{93a}$$

$$\mathbf{r}_{P,II}^I = \mathbf{r}_B^I + \mathbf{r}_{BM}^I + \mathbf{r}_{MP,II}^I\,, \quad \mathbf{v}_{P,II}^I = \mathbf{v}_B^I + \boldsymbol{\omega}^I \times \left(\mathbf{r}_{BM}^I + \mathbf{r}_{MP,II}^I\right)\,. \tag{93b}$$

The normal penetration between object I and plane j or object II and their time derivatives are then

$$\delta_j^I = \mathbf{n}_j \cdot \mathbf{r}_{P,j}^I + d_j\,, \qquad \dot{\delta}_j^I = \mathbf{n}_j \cdot \mathbf{v}_{P,j}^I\,, \tag{94}$$

$$\delta_{II}^I = \mathbf{n}_{II}^I \cdot \left(\mathbf{r}_{P,II}^I - \mathbf{r}_{P,I}^{II}\right)\,, \quad \dot{\delta}_j^I = \mathbf{n}_{II}^I \cdot \left(\mathbf{v}_{P,II}^I - \mathbf{v}_{P,I}^{II}\right)\,, \tag{95}$$

where $\mathbf{n}_{II}^I$ is the outer normal vector of object I at P_{II}^I and $\delta_j^I < 0$ or $\delta_{II}^I < 0$ means that there is no contact between object I and plane j or object II. The Flores et al. contact normal force model via [41, Eq. (44)] is used to calculate a restoring normal forces

$$F_{n,j}^I = \begin{cases} \dfrac{4}{3}\left(\dfrac{1-\nu_I^2}{E_I} + \dfrac{1-\nu_j^2}{E_j}\right)^{-1} \left(\kappa_1^I \kappa_2^I\right)^{-\frac{1}{4}} \left(1 + \dfrac{8(1-c_{r,j}^I)}{5c_{r,j}^I}\dfrac{\dot{\delta}_j^I}{\dot{\delta}_j^{I-}}\right)\left(\delta_j^I\right)^{\frac{3}{2}}\,, & \text{if } \delta_j^I > 0 \text{ and } \dfrac{8(1-c_{r,j}^I)}{5c_{r,j}^I}\dfrac{\dot{\delta}_j^I}{\dot{\delta}_j^{I-}} > -1\,, \\ 0\,, & \text{otherwise,} \end{cases} \tag{96a}$$

$$F_{n,II}^I = \begin{cases} \dfrac{4}{3}\left(\dfrac{1-\nu_I^2}{E_I} + \dfrac{1-\nu_{II}^2}{E_{II}}\right)^{-1} \left(\kappa_1^{I,II} \kappa_2^{I,II}\right)^{-\frac{1}{4}} \left(1 + \dfrac{8(1-c_{r,II}^I)}{5c_{r,II}^I}\dfrac{\dot{\delta}_{II}^I}{\dot{\delta}_{II}^{I-}}\right)\left(\delta_{II}^I\right)^{\frac{3}{2}}\,, & \text{if } \delta_{II}^I > 0 \text{ and } \dfrac{8(1-c_{r,II}^I)}{5c_{r,II}^I}\dfrac{\dot{\delta}_{II}^I}{\dot{\delta}_{II}^{I-}} > -1\,, \\ 0\,, & \text{otherwise.} \end{cases} \tag{96b}$$

This requires the Young's moduli E_I, E_{II}, E_j and Poisson's ratios ν_I, ν_{II}, ν_j of the objects and the j-th plane, the Gaussian curvature $\sqrt{\kappa_1^I \kappa_2^I}$ at P_j^I and the relative Gaussian curvature $\sqrt{\kappa_1^{I,II} \kappa_2^{I,II}}$ via Eq. (C.6) at P_{II}^I and the coefficients of restitution $c_{r,j}^I$, $c_{r,II}^I$ which are defined in Table C.3. The initial impact velocities $\dot{\delta}_j^{I-}$, $\dot{\delta}_{II}^{I-}$ are determined whenever the respective collision occurs. Negative values are set to zero [45]. Additionally, a friction force in tangential direction is introduced as

$$\mathbf{F}_{t,j}^I = \begin{cases} -\dfrac{\mu F_{n,j}^I}{k}\mathbf{v}_{t,j}^I\,, & \text{if } \dfrac{\|\mathbf{v}_{t,j}^I\|}{k} < 10^{-6}\,, \\ -\dfrac{\mu F_{n,j}^I}{\|\mathbf{v}_{t,j}^I\|}\tanh\left(\dfrac{\|\mathbf{v}_{t,j}^I\|}{k}\right)\mathbf{v}_{t,j}^I\,, & \text{otherwise,} \end{cases} \tag{97a}$$

$$\mathbf{F}_{t,II}^I = \begin{cases} -\dfrac{\mu F_{n,II}^I}{k}\mathbf{v}_{t,II}^I\,, & \text{if } \dfrac{\|\mathbf{v}_{t,II}^I\|}{k} < 10^{-6}\,, \\ -\dfrac{\mu F_{n,II}^I}{\|\mathbf{v}_{t,II}^I\|}\tanh\left(\dfrac{\|\mathbf{v}_{t,II}^I\|}{k}\right)\mathbf{v}_{t,II}^I\,, & \text{otherwise,} \end{cases} \tag{97b}$$

with the tangential velocities

$$\mathbf{v}_{t,j}^I = \mathbf{v}_{P,j}^I - (\mathbf{n}_j \cdot \mathbf{v}_{P,j}^I)\mathbf{n}_j\,, \quad \mathbf{v}_{t,II}^I = \mathbf{v}_{P,II}^I - (\mathbf{n}_{II}^I \cdot \mathbf{v}_{P,II}^I)\mathbf{n}_{II}^I\,, \tag{98}$$

the friction coefficient μ and some constant $k \ll 1$.[13] The total interaction forces at P_j and P_{II}^I are

$$\mathbf{F}_{P,j} = F_{n,j}^I\,\mathbf{n}_j + \mathbf{F}_{t,j}^I\,, \quad \mathbf{F}_{P,II} = -F_{n,II}^I\,\mathbf{n}_{II}^I + \mathbf{F}_{t,II}^I\,. \tag{99}$$

The mass and inertia tensor of object I are m^I and $\Theta^I = \Theta_x^I\,\mathbf{b}_\mathrm{x}^I \otimes \mathbf{b}_\mathrm{x}^I + \Theta_y^I\,\mathbf{b}_\mathrm{y}^I \otimes \mathbf{b}_\mathrm{y}^I + \Theta_z^I\,\mathbf{b}_\mathrm{z}^I \otimes \mathbf{b}_\mathrm{z}^I$ and the system is governed by the differential equations

$$\frac{{}^{\mathcal{J}}\mathrm{d}}{\mathrm{d}t}\,\mathbf{v}_B^I = \mathbf{g} + \frac{1}{m^I}\left(\mathbf{F}_{P,II}^I + \sum_{j=1}^{5}\mathbf{F}_{P,j}^I\right)\,, \tag{100a}$$

$$\frac{{}^{\mathcal{B},I}\mathrm{d}}{\mathrm{d}t}\,\boldsymbol{\omega}^I = \left(\Theta^I\right)^{-1}\left(-\boldsymbol{\omega}^I \times (\Theta^I \cdot \boldsymbol{\omega}^I) + \left(\mathbf{r}_{BM}^I + \mathbf{r}_{MP,II}^I - \frac{\delta_{II}^I}{2}\mathbf{n}_{II}^I\right) \times \mathbf{F}_{P,II}^I + \sum_{j=1}^{5}\left(\mathbf{r}_{BM}^I + \mathbf{r}_{MP,j}^I + \frac{\delta_j^I}{2}\mathbf{n}_j\right) \times \mathbf{F}_{P,j}^I\right) \tag{100b}$$

where the operators ${}^{\mathcal{J}}\mathrm{d}/\mathrm{d}t$ and ${}^{\mathcal{B},I}\mathrm{d}/\mathrm{d}t$ define the time derivative of the vector components in frame $\mathcal{J}$ and $\mathcal{B}^I$, respectively. For the moment balance (100b) it is assumed that the contact forces act at half the penetration depth, that is, at the mean value between the points with the common normal on both object boundaries. Using the generalized coordinates $q = [x_B(t), y_B(t), z_B(t), \alpha(t), \beta(t), \gamma(t)]$ for each object, Eqs. (100) can be transformed into a system of ordinary differential equations of first order and solved numerically.

An example implementation of the described system in *Matlab* is provided as supplementary material to this manuscript. The parameters and initial conditions in Appendix C are chosen for the numerical simulation. The young's modulus and Poisson's ratio of steel are used for all objects and planes. Both objects are released above one of the corners of the box with an initial angular velocity. Snapshots of the solution are displayed in Fig. 9; an animation is provided as supplementary material. After the initial drop, the objects bounce inside the box and there are multiple contacts between themselves and with all planes, at times there are several contacts simultaneously. The movement slows down rapidly since energy is dissipated by the contact forces.

The case study demonstrates a possible application of the normal parameterization for multibody simulations. The description of the geometry of any object is independent of its mechanical properties such as the center of mass and the inertia tensor. The collision detection via the common normal concept provides potential contact points with high accuracy, which can be used to describe the interaction forces between two objects. As far as we have observed, there are no artifacts caused by this contact kinematics that lead to unphysical behavior such as an unmodeled energy source (negative damping). Collision detection with a planar counterpart can be explicitly solved and easily implemented; collision detection between two convex objects has to be performed iteratively via algorithm III as described in Section 5.1. This algorithm is implemented in a modular way, where a subroutine is called to evaluate the normal parameterization for the generating potential of each object involved. The collision detection algorithm is therefore insofar independent of the object's geometries that only this subroutine needs to be replaced or updated if a different generating potential is to be specified. The collision detection problem is solved in every time step. Since the selected parameters lead to high contact stiffness, the *Matlab* solver *ode15s*[14] is used for numerical time integration. This does

[13] This friction model is a modification of Coulomb friction to avoid typical numerical problems due to its non-smoothness. For very small velocities—the first case is a linearization for vanishing velocity—this friction model resembles viscous damping. The parameter k is used to define the behavior at very small velocities. This friction model does not allow for a sticking contact.

[14] This is an implicit variable step, variable order method based on numerical differentiation formulas for sets of stiff ordinary differential equations.

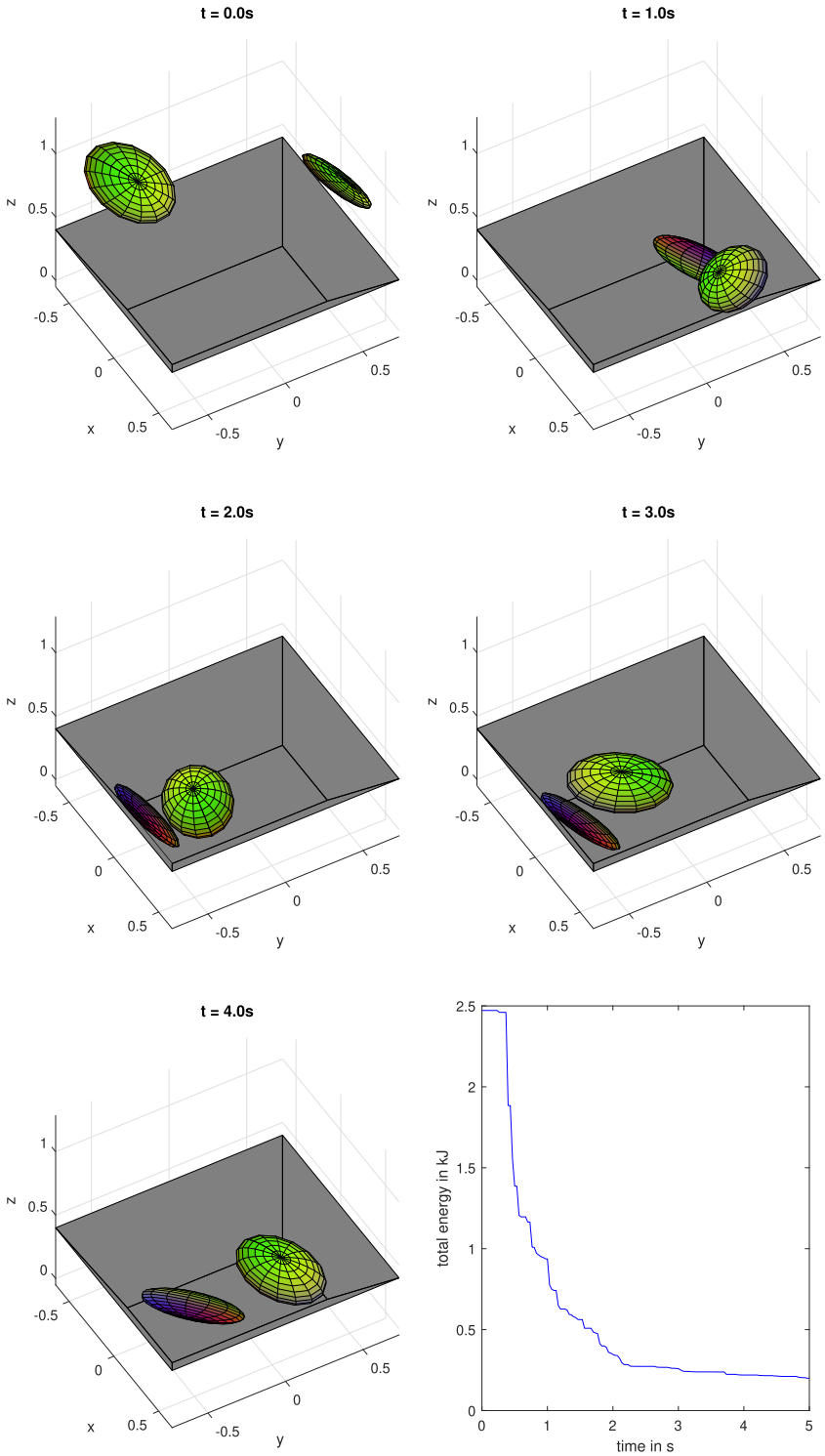

Figure 9: Snapshots of the time simulation of the ellipsoid for $t \in \{0, 1, 2, 3, 4\}$ s and total energy (bottom right).

not allow the exchange of information between different time steps and therefore the collision detection algorithm is always restarted with the direction from center to center. Although sufficient for the demonstration purposes of this case study, an implementation focusing on high efficiency should warm-start the collision detection with the normal vector from the previous time step. Because of this and other limitations of the implementation in *Matlab*, a comparison of different algorithms in terms of efficiency and computation time is not very conclusive, and is therefore omitted.

7. Discussion

The normal parameterization as derived in Sections 2 and 3 is a generalization and extension of a description for two-dimensional and three-dimensional objects which was previously proposed for two-dimensional objects by the authors in [54]. The proper statement of all requirements and assumptions which are necessary to prove different statements for the continuity and differentiability of the boundary line or surface and the additional curvature relationships provide a theoretical base for the use of this new parameterization in any application. While the treatment of the two-dimensional case is very compact and yields clear and compact expressions, the treatment of the three-dimensional case is more extensive due to the coordinate singularities. The coordinate singularities are not an inherent property of the boundary surface but arise rather artificially due to the orientation of the chosen body-fixed reference frame. A further extension or generalization of the presented concept which does not suffer from these artificial singularities is desirable, however, there is no clear and apparent approach to achieve this.

Another challenging problem which has yet to be addressed is the definition of the generating potential for arbitrary geometries. The normal parameterization introduced herein is a general solution that applies to any strictly convex two-dimensional or three-dimensional geometry given its generating potential. The presented results indicate that further generalizations for arbitrary dimensions might be possible, however, this has not been investigated yet. So far, the authors have derived the three-dimensional generating potential for ellipsoids, superquadrics and superellipsoids. The derivation or definition of other generating potentials is paramount for the future use of the normal parameterization in any application. As illustrated in Example 9, the derivation of the generating potential for a given geometry is non-trivial. However, this is partly mitigated by the possibility of using splines, NURBS or other piecewise functions to approximate given geometries, as discussed in Remarks 11 and 22.

The derivation of the normal parameterization by means of rigid body kinematics in Section 4 motivates the application of the presented approach to the problem of collision detection. In fact, the derivation itself relies on the contact of an object with a plane. This is also the simplest case for the collision detection problem, because the normal vector of the object's counterpart is constant. The normal parameterization allows for an explicit calculation of the potential contact point by means of the common normal concept; a property which has not been shown for any other description of two-dimensional or three-dimensional objects which we are aware of. Although the special case where the counterpart is a plane may seem like a major limitation, there is a need for this in certain disciplines. One example is the modeling of foot-ground contact in biomechanics, prosthetics and robotics. Smooth rigid body models for feet are either based on parameterizations that require an iterative solution for collision detection [57] even for this simple case, or they make use of circles/ellipses [65, 66] or spheres/ellipsoids [67, 68] to achieve an explicit and fast solution. With the normal parameterization, a more precise modeling and at the same time an explicit solution is possible, which will allow the use e.g. in real-time capable control systems [65].

However, the general collision detection problem for two objects, neither of which is a plane, cannot be solved explicitly but still requires some iterative procedure. In the literature, this is usually done using a Newton method with an analytical Jacobian [4, 6], whereby with the usual parameterizations two coordinates per object are sought and thus a total of four equations with four unknowns have to be solved. In Section 5, four iteration schemes for collision detection between two objects are examined with respect to implementation effort, robustness and rate of convergence. The literature approach of a Newton method with an analytical Jacobian requires only two equations and two unknowns (algorithm II, Eq. (85)) due to the demand for antiparallelism from the common normal concept. Whether this is advantageous from the point of view of computational effort and time was not investigated, since the number of additions and multiplications strongly depends on the geometry (i.e. which formulas define the parameterization) and the sophistication of the implementation. Instead, algorithm III (Eqs. (87)–(89)) is presented which does not need any derivatives. This iteration scheme is motivated by geometrical relationships of the normal vectors in two

consecutive iteration steps performs better in terms of implementation effort and robustness. However, it usually requires about twice as many iterations as a Newton scheme based on the common normal concept (algorithm II). Since the computation time per iteration is difficult to compare because of the reasons mentioned above, a general statement as to which algorithm is more efficient cannot be made. An approach which combines both procedures (algorithm IV) yields a comparable number of iterations as the Newton scheme but performs slightly worse than the derivative free scheme in terms of robustness. A conclusion as to which of these three approaches performs best in any given application cannot yet be made and requires further research. However, it should be mentioned that the derivative-free method as per algorithm III is only possible with the normal parameterization. This method has a comparatively low implementation effort and is independent of the respective object geometry; thus, it is not necessary to implement new Jacobians for each geometry or combination of geometries, as is the case with the Newton methods commonly used in literature.

The case study in Section 6 illustrates a possible application of the normal parameterization for collision detection in a multibody simulation. The calculation of the potential contact point based on the common normal concept uses the explicit solution for the potential contact point of each object with the plane boundaries of the box. The potential contact points for any collisions between the objects are determined iteratively by the derivative free iteration scheme from Section 5 (algorithm III). Furthermore, the objects' curvatures at any contact point is easily utilized in the normal force model proposed by Flores et al. The contact model can be interchanged with other models which rely on curvature information to describe the interaction between the objects, c.f. [42, 43, 44, 45]. Tait-Bryan angles are used to parameterize the objects' orientations; however, the collision detection problem is independent of the specific parameterization and requires only the representation of the normal direction in the body-fixed frame which is used to define the normal parameterization. Therefore, other parameterizations like Euler parameters or unit quaternions can be used instead of Tait-Bryan angles without any changes to the implementation of the collision detection procedure.

8. Conclusions

The main results presented in the present manuscript are: (i) the normal parameterization for strictly convex two- and three-dimensional geometries; (ii) proofs for many relevant properties such as continuity/differentiability requirements and expressions for the curvature; (iii) offset curves or surfaces and (iv) collision detection algorithms based on the normal parameterization.

The normal parameterization is based on only a few, concise equations: the object's boundary curve is given by Eqs. (2) and (16) and the curvature by Eqs. (6) and (26) in the two- and three-dimensional case, respectively. The implementation of all expressions is straightforward and requires only derivatives up to order three of the (scalar) generating potential. Any application requires only the definition of the generating potential to describe the desired objects. So far, only expressions for (super-)ellipses and (super-)ellipsoids (and their offset curves or surfaces) have been found. The derivation of the generating potential for a given geometry – e. g. superovoids – is non-trivial and requires further research to broaden the applicability of this method. However, it is possible to approximate the generating potential of any strictly convex geometry by splines, NURBS or other piecewise functions (cf. Remarks 11 and 22) which offers a possibility to bypass this problem until further closed form solutions have been derived. In any case, the geometric continuity is given by the requirements in propositions 1 and 13.

The calculation of offset curves or surfaces is quite simple since it requires only the addition of a constant to the generating potential, as outlined in corollaries 7 and 19. This property appears to be useful for applications beyond multibody simulations such as computer aided design and manufacturing.

Collision detection based on the common normal concept can be realized either by a Newton method – ideally based on analytic gradients – or by a derivative-free fixed-point iteration. The latter proves to be more robust in the convergence study above, however, it requires a higher number of iterations to achieve a given accuracy. A special feature of the normal parameterization is that collisions with a plane can be calculated explicitly, whereas this is not possible with any other parameterization method known to the authors. An implementation of collision detection based on the normal parameterization with two objects and five planes is provided. This case study shows no unexpected drawbacks and illustrates the applicability of the presented approach.

The focus of the present manuscript is on the theoretical basis of the normal parameterization and its applicability for collision detection. Both subjects are treated in detail, but some important issues for future research remain: the

normal parameterization for three-dimensional objects suffers from two coordinate singularities due to the choice of spherical coordinates to describe the direction of the outer normal vector; a further extension or generalization of the presented concept which does not suffer from these artificial singularities is a desirable goal.

Four collision detection algorithms are introduced and compared in the presented convergence study, three of which show good performance in terms of robustness and rate of convergence. However, a benchmark study with a comparison to established collision detection algorithms (e. g. [5, 6, 23]) is required before any quantitative assessment of the presented approach's benefits can be made.

The normal parameterization itself appears to be a fundamental result in the area of classical differential geometry. The presented results for $N \in \{2, 3\}$ show that an embedded $N-1$-dimensional manifold in an N-dimensional Euclidean space which encloses a strictly convex set is fully described by its generating potential. This concept is very similar to the natural parameterization of embedded 1-dimensional manifolds in N-dimensional Euclidean space (curves). Further extensions and generalizations of the presented approach as a fundamental concept for analysis in differential geometry is desirable, but exceeds the authors' own expertise.

Appendix A. Notation

The following notation is used throughout the manuscript: vectors are denoted by bold lowercase letters, e. g. $\mathbf{a}$. Reference frames are denoted by capital calligraphic letters, e. g. $\mathcal{I}$. The same lowercase letter denotes the corresponding right-handed orthonormal base vectors

$$\left\{\mathbf{i}_\mathrm{x}, \mathbf{i}_\mathrm{y}, \mathbf{i}_\mathrm{z}\right\} .$$

The decomposition of a vector in the reference frame $\mathcal{I}$ is denoted

$$\mathbf{a} = x^\mathcal{I}\mathbf{i}_\mathrm{x} + y^\mathcal{I}\mathbf{i}_\mathrm{y} + z^\mathcal{I}\mathbf{i}_\mathrm{z} .$$

The rotation tensor from reference frame $\mathcal{J}$ to $\mathcal{I}$ is expressed as

$$\mathrm{Q}^{\mathcal{I}\mathcal{J}} := \sum_p \sum_q Q^{\mathcal{I}\mathcal{J}}_{pq}\, \mathbf{i}_p \otimes \mathbf{j}_q , \quad p, q \in \{\mathrm{x}, \mathrm{y}, \mathrm{z}\}$$

and the corresponding rotation matrix

$$\mathrm{Q}^{\mathcal{I}\mathcal{J}} := \begin{bmatrix} Q^{\mathcal{I}\mathcal{J}}_{\mathrm{xx}} & Q^{\mathcal{I}\mathcal{J}}_{\mathrm{xy}} & Q^{\mathcal{I}\mathcal{J}}_{\mathrm{xz}} \\ Q^{\mathcal{I}\mathcal{J}}_{\mathrm{yx}} & Q^{\mathcal{I}\mathcal{J}}_{\mathrm{yy}} & Q^{\mathcal{I}\mathcal{J}}_{\mathrm{yz}} \\ Q^{\mathcal{I}\mathcal{J}}_{\mathrm{zx}} & Q^{\mathcal{I}\mathcal{J}}_{\mathrm{zy}} & Q^{\mathcal{I}\mathcal{J}}_{\mathrm{zz}} \end{bmatrix}$$

is orthogonal

$$\left(\mathrm{Q}^{\mathcal{I}\mathcal{J}}\right)^{-1} = \left(\mathrm{Q}^{\mathcal{I}\mathcal{J}}\right)^T = \mathrm{Q}^{\mathcal{J}\mathcal{I}} .$$

The derivative of a function with respect to a single argument is denoted by

$$a'(b) := \frac{\mathrm{d}}{\mathrm{d}b} a(b) ,$$

time derivatives are denoted by a dot unless stated otherwise

$$\dot{a} := \frac{\mathrm{d}}{\mathrm{d}t} a ,$$

and partial derivatives by the shorthand

$$\partial_a := \frac{\partial}{\partial a} .$$

The function arctan2—the arctangent with two arguments—is defined as

$$\operatorname{arctan2}(x,y) := \begin{cases} \arctan\left(\frac{y}{x}\right) & \text{for } x > 0 \\ \arctan\left(\frac{y}{x}\right) + \pi & \text{for } x < 0, y > 0 \\ \pm\pi & \text{for } x < 0, y = 0 \\ \arctan\left(\frac{y}{x}\right) - \pi & \text{for } x < 0, y < 0 \\ +\frac{\pi}{2} & \text{for } x = 0, y > 0 \\ -\frac{\pi}{2} & \text{for } x = 0, y < 0\,. \end{cases}$$

Appendix B. Proof of completeness for transformation (66)

The transformation given by Eq. (66) is complete if it allows for rotations of the body around any arbitrary axis (given by a unit vector $\mathbf{a}$) by an arbitrary angle ψ. To show this property, the direction of the rotation axis is defined by spherical coordinates $\{\theta, \varphi\}$ in the inertial frame $\mathcal{I}$

$$\begin{aligned} \mathbf{a} &= \sin(\theta)\cos(\varphi)\,\mathbf{i}_\mathrm{x} + \sin(\theta)\sin(\varphi)\,\mathbf{i}_\mathrm{y} + \cos(\theta)\,\mathbf{i}_\mathrm{z} \\ &=: \mathrm{s}_\theta\mathrm{c}_\varphi\mathbf{i}_\mathrm{x} + \mathrm{s}_\theta\mathrm{s}_\varphi\mathbf{i}_\mathrm{y} + \mathrm{c}_\theta\mathbf{i}_\mathrm{z}\,. \end{aligned} \tag{B.1}$$

Due to the excessive length of the following expressions, the shorthand $\mathrm{s}_\theta := \sin(\theta)$, $\mathrm{c}_\theta := \cos(\theta)$ is used below. The rotation matrix which corresponds to a rotation of the body around this axis by the angle ψ is [21, Eq. (2.24)]

$$\mathrm{Q}^{\mathcal{IB}}(\theta,\varphi,\psi) = \begin{bmatrix} \mathrm{c}_\psi + \mathrm{s}_\theta^2\mathrm{c}_\varphi^2\left(1-\mathrm{c}_\psi\right) & \mathrm{s}_\theta^2\mathrm{s}_\varphi\mathrm{c}_\varphi\left(1-\mathrm{c}_\psi\right) - \mathrm{c}_\theta\mathrm{s}_\psi & \mathrm{s}_\theta\mathrm{c}_\theta\mathrm{c}_\varphi\left(1-\mathrm{c}_\psi\right) + \mathrm{s}_\theta\mathrm{s}_\varphi\mathrm{s}_\psi \\ \mathrm{s}_\theta^2\mathrm{s}_\varphi\mathrm{c}_\varphi\left(1-\mathrm{c}_\psi\right) + \mathrm{c}_\theta\mathrm{s}_\psi & \mathrm{c}_\psi + \mathrm{s}_\theta^2\mathrm{s}_\varphi^2\left(1-\mathrm{c}_\psi\right) & \mathrm{s}_\theta\mathrm{c}_\theta\mathrm{s}_\varphi\left(1-\mathrm{c}_\psi\right) - \mathrm{s}_\theta\mathrm{c}_\varphi\mathrm{s}_\psi \\ \mathrm{s}_\theta\mathrm{c}_\theta\mathrm{c}_\varphi\left(1-\mathrm{c}_\psi\right) - \mathrm{s}_\theta\mathrm{s}_\varphi\mathrm{s}_\psi & \mathrm{s}_\theta\mathrm{c}_\theta\mathrm{s}_\varphi\left(1-\mathrm{c}_\psi\right) + \mathrm{s}_\theta\mathrm{c}_\varphi\mathrm{s}_\psi & \mathrm{c}_\psi + \mathrm{c}_\theta^2\left(1-\mathrm{c}_\psi\right) \end{bmatrix} \tag{B.2}$$

and the transformation via Eq. (66) expressed in the same notation is

$$\mathrm{Q}^{\mathcal{IB}}(\alpha,\beta,\gamma) = \begin{bmatrix} \mathrm{c}_{\alpha/2}^2\mathrm{c}_\gamma - \mathrm{s}_{\alpha/2}^2\mathrm{c}_{2\beta+\gamma} & \mathrm{c}_{\alpha/2}^2\mathrm{s}_\gamma - \mathrm{s}_{\alpha/2}^2\mathrm{s}_{2\beta+\gamma} & \mathrm{s}_\alpha\mathrm{c}_{\beta+\gamma} \\ \mathrm{c}_{\alpha/2}^2\mathrm{s}_\gamma - \mathrm{s}_{\alpha/2}^2\mathrm{s}_{2\beta+\gamma} & \mathrm{c}_{\alpha/2}^2\mathrm{c}_\gamma + \mathrm{s}_{\alpha/2}^2\mathrm{c}_{2\beta+\gamma} & \mathrm{s}_\alpha\mathrm{s}_{\beta+\gamma} \\ -\mathrm{s}_\alpha\mathrm{c}_\beta & -\mathrm{s}_\alpha\mathrm{s}_\beta & \mathrm{c}_\alpha \end{bmatrix}. \tag{B.3}$$

The transformation is complete if there is a triple $\{\alpha,\beta,\gamma\}$ such that $\mathrm{Q}^{\mathcal{IB}}(\alpha,\beta,\gamma) = \mathrm{Q}^{\mathcal{IB}}(\theta,\varphi,\psi)$ for all $\theta \in [0,\pi]$, $\varphi \in [0,2\pi)$, $\psi \in [0,2\pi)$. The comparison of Eqs. (B.2) and (B.3) yields

$$\mathrm{c}_\alpha = \mathrm{c}_\psi + \mathrm{c}_\theta^2\left(1-\mathrm{c}_\psi\right)\,, \tag{B.4a}$$

$$-\mathrm{s}_\alpha\mathrm{s}_\beta = \mathrm{s}_\theta\mathrm{c}_\theta\mathrm{s}_\varphi\left(1-\mathrm{c}_\psi\right) + \mathrm{s}_\theta\mathrm{c}_\varphi\mathrm{s}_\psi =: \mathrm{s}_\theta k_1(\theta,\varphi,\psi)\,, \tag{B.4b}$$

$$-\mathrm{s}_\alpha\mathrm{c}_\beta = \mathrm{s}_\theta\mathrm{c}_\theta\mathrm{c}_\varphi\left(1-\mathrm{c}_\psi\right) - \mathrm{s}_\theta\mathrm{s}_\varphi\mathrm{s}_\psi =: \mathrm{s}_\theta k_2(\theta,\varphi,\psi)\,, \tag{B.4c}$$

$$\mathrm{s}_\alpha\mathrm{s}_{\beta+\gamma} = \mathrm{s}_\theta\mathrm{c}_\theta\mathrm{s}_\varphi\left(1-\mathrm{c}_\psi\right) - \mathrm{s}_\theta\mathrm{c}_\varphi\mathrm{s}_\psi =: \mathrm{s}_\theta k_3(\theta,\varphi,\psi)\,, \tag{B.4d}$$

$$\mathrm{s}_\alpha\mathrm{c}_{\beta+\gamma} = \mathrm{s}_\theta\mathrm{c}_\theta\mathrm{c}_\varphi\left(1-\mathrm{c}_\psi\right) + \mathrm{s}_\theta\mathrm{s}_\varphi\mathrm{s}_\psi =: \mathrm{s}_\theta k_4(\theta,\varphi,\psi) \tag{B.4e}$$

which can be solved for

$$\alpha = \arccos\left(\mathrm{c}_\theta^2 + \mathrm{s}_\theta^2\mathrm{c}_\psi\right)\,, \tag{B.5a}$$

$$\beta = \operatorname{arctan2}\left(-k_2(\theta,\varphi,\psi), -k_1(\theta,\varphi,\psi)\right), \tag{B.5b}$$

$$\begin{aligned} \gamma = \operatorname{arctan2}\big(&k_1(\theta,\varphi,\psi)k_3(\theta,\varphi,\psi) - k_2(\theta,\varphi,\psi)k_4(\theta,\varphi,\psi), \\ &-k_1(\theta,\varphi,\psi)k_4(\theta,\varphi,\psi) - k_2(\theta,\varphi,\psi)k_3(\theta,\varphi,\psi)\big)\,. \end{aligned} \tag{B.5c}$$

This is the direct transformation from Eq. (B.2) to (B.3) for all $\{\theta,\varphi,\psi\}$. □

Appendix C. Implementation details, parameters and initial conditions for the case study

Two sets of Tait–Bryan angles $\{\alpha(t), \beta(t), \gamma(t)\}$ and $\{\bar{\alpha}(t), \bar{\beta}(t), \bar{\gamma}(t)\}$ are used to circumvent the inherent coordinate singularities. The orientation of any object of the parameter study is described by the rotation matrix

$$\begin{aligned} \mathrm{Q}^{\mathcal{IB}} &= \begin{bmatrix} \cos\alpha(t)\cos\beta(t) & \cos\alpha(t)\sin\beta(t)\sin\gamma(t) - \sin\alpha(t)\cos\gamma(t) & \cos\alpha(t)\sin\beta(t)\cos\gamma(t) + \sin\alpha(t)\sin\gamma(t) \\ \sin\alpha(t)\cos\beta(t) & \sin\alpha(t)\sin\beta(t)\sin\gamma(t) + \cos\alpha(t)\cos\gamma(t) & \sin\alpha(t)\sin\beta(t)\cos\gamma(t) - \cos\alpha(t)\sin\gamma(t) \\ -\sin\beta(t) & \cos\beta(t)\sin\gamma(t) & \cos\beta(t)\cos\gamma(t) \end{bmatrix} \\ &= \begin{bmatrix} -\cos\bar{\alpha}(t)\sin\bar{\beta}(t)\cos\bar{\gamma}(t) - \sin\bar{\alpha}(t)\sin\bar{\gamma}(t) & \cos\bar{\alpha}(t)\sin\bar{\beta}(t)\sin\bar{\gamma}(t) - \sin\bar{\alpha}(t)\cos\bar{\gamma}(t) & \cos\bar{\alpha}(t)\cos\bar{\beta}(t) \\ -\sin\bar{\alpha}(t)\sin\bar{\beta}(t)\cos\bar{\gamma}(t) + \cos\bar{\alpha}(t)\sin\bar{\gamma}(t) & \sin\bar{\alpha}(t)\sin\bar{\beta}(t)\sin\bar{\gamma}(t) + \cos\bar{\alpha}(t)\cos\bar{\gamma}(t) & \sin\bar{\alpha}(t)\cos\bar{\beta}(t) \\ -\cos\bar{\beta}(t)\cos\bar{\gamma}(t) & \cos\bar{\beta}(t)\sin\bar{\gamma}(t) & -\sin\bar{\beta}(t) \end{bmatrix} \end{aligned} \tag{C.1}$$

and the angular velocity

$$\begin{aligned} \boldsymbol{\omega} &= \left(-\dot{\alpha}(t)\sin\beta(t) + \dot{\gamma}(t)\right)\mathbf{b}_\mathrm{x} + \left(\dot{\alpha}(t)\cos\beta(t)\sin\gamma(t) + \dot{\beta}(t)\cos\gamma(t)\right)\mathbf{b}_\mathrm{y} + \left(\dot{\alpha}(t)\cos\beta(t)\cos\gamma(t) - \dot{\beta}(t)\sin\gamma(t)\right)\mathbf{b}_\mathrm{z} \\ &= \left(-\dot{\bar{\alpha}}(t)\cos\bar{\beta}(t)\cos\bar{\gamma}(t) + \dot{\bar{\beta}}(t)\sin\bar{\gamma}(t)\right)\mathbf{b}_\mathrm{x} + \left(\dot{\bar{\alpha}}(t)\cos\bar{\beta}(t)\sin\bar{\gamma}(t) + \dot{\bar{\beta}}(t)\cos\bar{\gamma}(t)\right)\mathbf{b}_\mathrm{y} + \left(-\dot{\bar{\alpha}}(t)\sin\bar{\beta}(t) + \dot{\bar{\gamma}}(t)\right)\mathbf{b}_\mathrm{z}\,. \end{aligned} \tag{C.2}$$

The description is switched form one set to the other by the relationships

$$\alpha(t) = \arctan2(-\sin\bar{\alpha}(t)\sin\bar{\beta}(t)\cos\bar{\gamma}(t) + \cos\bar{\alpha}(t)\sin\bar{\gamma}(t), -\cos\bar{\alpha}(t)\sin\bar{\beta}(t)\cos\bar{\gamma}(t) - \sin\bar{\alpha}(t)\sin\bar{\gamma}(t))\,, \tag{C.3a}$$

$$\beta(t) = \arcsin(\cos\bar{\beta}(t)\cos\bar{\gamma}(t))\,, \tag{C.3b}$$

$$\gamma(t) = \arctan2(\cos\bar{\beta}(t)\sin\bar{\gamma}(t), -\sin\bar{\beta}(t))\,, \tag{C.3c}$$

$$\dot{\alpha}(t) = \dot{\bar{\alpha}}(t) + \frac{\dot{\bar{\beta}}(t)\cos\bar{\beta}(t)\cos\bar{\gamma}(t)\sin\bar{\gamma}(t) - \dot{\bar{\gamma}}(t)\sin\bar{\beta}(t)}{1 - \cos^2\bar{\beta}(t)\cos^2\bar{\gamma}(t)}\,, \tag{C.3d}$$

$$\dot{\beta}(t) = -\frac{\dot{\bar{\beta}}(t)\sin\bar{\beta}(t)\cos\bar{\gamma}(t) + \dot{\bar{\gamma}}(t)\cos\bar{\beta}(t)\sin\bar{\gamma}(t)}{\sqrt{1 - \cos^2\bar{\beta}(t)\cos^2\bar{\gamma}(t)}}\,, \tag{C.3e}$$

$$\dot{\gamma}(t) = \frac{\dot{\bar{\beta}}(t)\sin\bar{\gamma}(t) - \dot{\bar{\gamma}}(t)\cos\bar{\beta}(t)\sin\bar{\beta}(t)\cos\bar{\gamma}(t)}{1 - \cos^2\bar{\beta}(t)\cos^2\bar{\gamma}(t)} \tag{C.3f}$$

and

$$\bar{\alpha}(t) = \arctan2(\sin\alpha(t)\sin\beta(t)\cos\gamma(t) - \cos\alpha(t)\sin\gamma(t), \cos\alpha(t)\sin\beta(t)\cos\gamma(t) + \sin\alpha(t)\sin\gamma(t))\,, \tag{C.4a}$$

$$\bar{\beta}(t) = -\arcsin(\cos\beta(t)\cos\gamma(t))\,, \tag{C.4b}$$

$$\bar{\gamma}(t) = \arctan2(\cos\beta(t)\sin\gamma(t), \bar{\beta}(t))\,, \tag{C.4c}$$

$$\dot{\bar{\alpha}}(t) = \dot{\alpha}(t) + \frac{\dot{\beta}(t)\cos\beta(t)\cos\gamma(t)\sin\gamma(t) - \dot{\gamma}(t)\sin\beta(t)}{1 - \cos^2\beta(t)\cos^2\gamma(t)}\,, \tag{C.4d}$$

$$\dot{\bar{\beta}}(t) = \frac{\dot{\beta}(t)\sin\beta(t)\cos\gamma(t) + \dot{\gamma}(t)\cos\beta(t)\sin\gamma(t)}{\sqrt{1 - \cos^2\beta(t)\cos^2\gamma(t)}}\,, \tag{C.4e}$$

$$\dot{\bar{\gamma}}(t) = \frac{-\dot{\beta}(t)\sin\gamma(t) + \dot{\gamma}(t)\cos\beta(t)\sin\beta(t)\cos\gamma(t)}{1 - \cos^2\beta(t)\cos^2\gamma(t)} \tag{C.4f}$$

whenever $\cos\beta(t) < 0.1$ or $\cos\bar{\beta}(t) < 0.1$.

If there is contact between the objects I and II, the normal force component is calculated by an extension of the model proposed by Flores et al., which is itself an extension of the Hertz theory for elastic contacts. In the case of two convex objects, the Hertzian model requires the calculation of the effective curvature $\sqrt{\kappa_1^{I,II}\kappa_2^{I,II}}$ which depends on the principal curvatures κ_1^I, κ_2^I, κ_1^{II} and κ_2^{II} of both objects at the contact point and the relative orientation of the

corresponding principal curvature directions $\mathbf{c}_1^I$, $\mathbf{c}_2^I$, $\mathbf{c}_1^{II}$ and $\mathbf{c}_2^{II}$. A derivation of the necessary relationships is given in [39, Section 4.1, p. 84–85].

The principal curvature directions $\mathbf{c}_1^I$, $\mathbf{c}_2^I$, $\mathbf{c}_1^{II}$ and $\mathbf{c}_2^{II}$ are unique except for their sign. To derive a correct implementation, the signs of object II are defined by

$$\mathbf{c}_1^{II} \leftarrow \operatorname{sign}(\mathbf{c}_1^I \cdot \mathbf{c}_1^{II})\, \mathbf{c}_1^{II} ,$$
$$\mathbf{c}_2^{II} \leftarrow \operatorname{sign}(\mathbf{c}_2^I \cdot \mathbf{c}_2^{II})\, \mathbf{c}_2^{II} .$$

The relative orientation of the principal curvatures is then

$$\vartheta = -\operatorname{sign}(\mathbf{c}_1^I \cdot \mathbf{c}_2^{II}) \arccos(\mathbf{c}_1^I \cdot \mathbf{c}_1^{II}) \tag{C.5}$$

and the principal relative curvatures follow from

$$\left(\kappa_1^{I,II} + \kappa_2^{I,II}\right) = \frac{1}{2}\left(\kappa_1^I + \kappa_2^I + \kappa_1^{II} + \kappa_2^{II}\right) , \tag{C.6a}$$

$$\left|\kappa_1^{I,II} - \kappa_2^{I,II}\right| = \frac{1}{2}\sqrt{\left(\kappa_1^I - \kappa_2^I\right)^2 + \left(\kappa_1^{II} - \kappa_2^{II}\right)^2 + 2\left(\kappa_1^I - \kappa_2^I\right)\left(\kappa_1^{II} - \kappa_2^{II}\right)\cos(2\vartheta)} . \tag{C.6b}$$

References

[1] J. D. Foley, A. van Dam, S. K. Feiner, J. F. Hughes, Computer Graphics: Principles and Practice, 2nd Edition, The Systems Programming Series, Addison-Wesley, Reading, MA, 1996.

[2] M. C. Lin, S. Gottschalk, Collision detection between geometric models: a survey, in: Proc. of IMA Conf. on Mathematics of Surfaces, Vol. 1, San Diego, CA, 1998, pp. 602–608.

[3] R. J. Campbell, P. J. Flynn, A survey of free-form object representation and recognition techniques, Comput. Vis. Image Und. 81 (2) (2001) 166–210. doi:10.1006/cviu.2000.0889.

[4] D. S. Lopes, M. T. Silva, J. A. Ambrósio, P. Flores, A mathematical framework for rigid contact detection between quadric and superquadric surfaces, Multibody Syst. Dyn. 24 (3) (2010) 255–280. doi:10.1007/s11044-010-9220-0.

[5] C. Wellmann, C. Lillie, P. Wriggers, A contact detection algorithm for superellipsoids based on the common-normal concept, Eng. Comp. 25 (5) (2008) 432–442. doi:10.1108/02644400810881374.

[6] A. A. Gonçalves, A. Bernardino, J. Jorge, D. S. Lopes, A benchmark study on accuracy-controlled distance calculation between superellipsoid and superovoid contact geometries, Mech. Mach. Theory 115 (2017) 77–96. doi:10.1016/j.mechmachtheory.2017.04.008.

[7] T. W. Sederberg, D. C. Anderson, R. N. Goldman, Implicit Representation of Parametric Curves and Surfaces, Comput. Vision Graph. 28 (1) (1984) 72–84. doi:10.1016/0734-189X(84)90140-3.

[8] Y. Lai, F. Chen, Implicitizing rational surfaces using moving quadrics constructed from moving planes, J. Symb. Comput. 77 (2016) 127–161. doi:10.1016/j.jsc.2016.02.001.

[9] T. J. R. Hughes, R. L. Taylor, J. L. Sackman, A. Curnier, W. Kanoknukulchai, A finite element method for a class of contact-impact problems, Comput. Method. Appl. M. 8 (3) (1976) 249–276. doi:10.1016/0045-7825(76)90018-9.

[10] F. B. Belgacem, P. Hild, P. Laborde, The Mortar Finite Element Method for Contact Problems, Math. Comput. Model. 28 (4-8) (1998) 263–271. doi:10.1016/s0895-7177(98)00121-6.

[11] P. Wriggers, Computational Contact Mechanics, Springer, Berlin Heidelberg, 2006. doi:10.1007/978-3-540-32609-0.

[12] N. G. Bourago, V. N. Kukudzhanov, A review of contact algorithms, Mech. Solids 40 (1) (2005) 35–71. URL ipmnet.ru/~burago/papers/cont-e.pdf

[13] T. J. R. Hughes, J. A. Cottrell, Y. Bazilevs, Isogeometric analysis: CAD, finite elements, NURBS, exact geometry and mesh refinement, Comput. Method. Appl. M. 194 (39-41) (2005) 4135–4195. doi:10.1016/j.cma.2004.10.008.

[14] J. A. Cottrell, T. J. R. Hughes, Y. Bazilevs, Isogeometric Analysis: Toward Integration of CAD and FEA, Wiley, Chichester, 2009.

[15] L. De Lorenzis, P. Wriggers, T. J. R. Hughes, Isogeometric contact: a review, GAMM-Mitteilungen 37 (1) (2014) 85–123. doi:10.1002/gamm.201410005.

[16] C. Carstensen, O. Scherf, P. Wriggers, Adaptive Finite Elements for Elastic Bodies in Contact, SIAM J. Sci. Comput. 20 (5) (1999) 1605–1626. doi:10.1137/s1064827595295350.

[17] C. Zimmermann, R. A. Sauer, Adaptive local surface refinement based on LR NURBS and its application to contact, Comput. Mech. 60 (6) (2017) 1011–1031. doi:10.1007/s00466-017-1455-7.

[18] A. A. Shabana, Flexible Multibody Dynamics: Review of Past and Recent Developments, Multibody Syst. Dyn. 1 (2) (1997) 189–222. doi:10.1023/a:1009773505418.

[19] O. A. Bauchau, Flexible multibody dynamics, no. 176 in Solid Mechanics and Its Applications, Springer, Dordrecht, 2011. doi:10.1007/978-94-007-0335-3.

[20] B. Simeon, Computational Flexible Multibody Dynamics: A Differential-Algebraic Approach, 1st Edition, Differential-Algebraic Equations Forum, Springer, Berlin Heidelberg, 2013. doi:10.1007/978-3-642-35158-7.

Table C.3: Parameters and initial conditions for case study.

parameter or variable	value	unit	description
g	9.81	$\mathrm{m/s^2}$	gravity
E	210	GPa	Young's modulus (both objects and all planes)
ν	0.3		Poisson's ratio (both objects and all planes)
c_r	0.6		coefficient of restitution (all contacts)
μ	0.2		coefficient of friction (all contacts)
k	10^{-6}		constant in friction model (all contacts)
a^I	0.3	m	$\mathbf{m}^I_{\mathrm{x}}$ semi axis of object I
b^I	0.2	m	$\mathbf{m}^I_{\mathrm{y}}$ semi axis of object I
c^I	0.1	m	$\mathbf{m}^I_{\mathrm{z}}$ semi axis of object I
m^I	200	kg	mass of object I
Θ^I	$2\,\mathbf{b}^I_{\mathrm{x}} \otimes \mathbf{b}^I_{\mathrm{x}} + 4\,\mathbf{b}^I_{\mathrm{y}} \otimes \mathbf{b}^I_{\mathrm{y}} + 5.2\,\mathbf{b}^I_{\mathrm{z}} \otimes \mathbf{b}^I_{\mathrm{z}}$	$\mathrm{kg\,m^2}$	inertia tensor of object I
$\mathbf{r}^I_{BM}$	$0.025\mathbf{b}^I_{\mathrm{z}}$	m	distance from B^I to M^I of object I
$\mathrm{Q}^{\mathcal{BM},I}$	$\begin{bmatrix} \cos(\frac{\pi}{18}) & 0 & -\sin(\frac{\pi}{18}) \\ 0 & 1 & 0 \\ \sin(\frac{\pi}{18}) & 0 & \cos(\frac{\pi}{18}) \end{bmatrix}$		rotation matrix from $\mathcal{M}^I$ to $\mathcal{B}^I$ of object I
a^{II}	0.3	m	$\mathbf{m}^{II}_{\mathrm{x}}$ semi axis of object II
b^{II}	0.05	m	$\mathbf{m}^{II}_{\mathrm{y}}$ semi axis of object II
c^{II}	0.1	m	$\mathbf{m}^{II}_{\mathrm{z}}$ semi axis of object II
m^{II}	50	kg	mass of object II
Θ^{II}	$0.1\,\mathbf{b}^{II}_{\mathrm{x}} \otimes \mathbf{b}^{II}_{\mathrm{x}} + 1\,\mathbf{b}^{II}_{\mathrm{y}} \otimes \mathbf{b}^{II}_{\mathrm{y}} + 0.9\,\mathbf{b}^{II}_{\mathrm{z}} \otimes \mathbf{b}^{II}_{\mathrm{z}}$	$\mathrm{kg\,m^2}$	inertia tensor of object II
$\mathbf{r}^{II}_{BM}$	$0.075\mathbf{b}^{II}_{\mathrm{x}}$	m	distance from B^{II} to M^{II} of object II
$\mathrm{Q}^{\mathcal{BM},II}$	$\begin{bmatrix} \cos(\frac{\pi}{18}) & 0 & \sin(\frac{\pi}{18}) \\ 0 & 1 & 0 \\ -\sin(\frac{\pi}{18}) & 0 & \cos(\frac{\pi}{18}) \end{bmatrix}$		rotation matrix from $\mathcal{M}^{II}$ to $\mathcal{B}^{II}$ of object II
$\mathbf{n}_1$	$\mathbf{j}_{\mathrm{z}}$		normal vector of plane 1
d_1	0	m	distance of plane 1 from origin
$\mathbf{n}_2$	$\frac{\sqrt{2}}{2}\,\mathbf{j}_{\mathrm{x}} + \frac{\sqrt{2}}{2}\,\mathbf{j}_{\mathrm{z}}$		normal vector of plane 2
d_2	$-\frac{\sqrt{2}}{8}$	m	distance of plane 2 from origin
$\mathbf{n}_3$	$-\frac{\sqrt{2}}{2}\,\mathbf{j}_{\mathrm{x}} + \frac{\sqrt{2}}{2}\,\mathbf{j}_{\mathrm{z}}$		normal vector of plane 3
d_3	$-\frac{\sqrt{2}}{8}$	m	distance of plane 3 from origin
$\mathbf{n}_4$	$-\frac{\sqrt{3}}{2}\,\mathbf{j}_{\mathrm{y}} + \frac{1}{2}\,\mathbf{j}_{\mathrm{z}}$		normal vector of plane 4
d_4	$-\frac{\sqrt{3}}{4}$	m	distance of plane 4 from origin
$\mathbf{n}_5$	$\frac{\sqrt{3}}{2}\,\mathbf{j}_{\mathrm{y}} + \frac{1}{2}\,\mathbf{j}_{\mathrm{z}}$		normal vector of plane 5
d_5	$-\frac{\sqrt{3}}{4}$	m	distance of plane 5 from origin
$x^I_B(0), y^I_B(0), z^I_B(0)$	$-\frac{1}{4}, -\frac{1}{2}, 1$	m	initial position of object I
$\dot{x}^I_B(0), \dot{y}^I_B(0), \dot{z}^I_B(0)$	$0, 0, 0$	m/s	initial velocity of object I
$\alpha^I(0), \beta^I(0), \gamma^I(0)$	$\frac{\pi}{3}, \frac{\pi}{4}, \frac{\pi}{5}$	rad	initial orientation of object I
$\dot{\alpha}^I(0), \dot{\beta}^I(0), \dot{\gamma}^I(0)$	$\pi, 0, 0$	rad/s	initial angular velocity of object I
$x^{II}_B(0), y^{II}_B(0), z^{II}_B(0)$	$\frac{1}{4}, \frac{1}{2}, 1$	m	initial position of object II
$\dot{x}^{II}_B(0), \dot{y}^{II}_B(0), \dot{z}^{II}_B(0)$	$0, 0, 0$	m/s	initial velocity of object II
$\alpha^{II}(0), \beta^{II}(0), \gamma^{II}(0)$	$\frac{\pi}{3}, \frac{\pi}{4}, \frac{\pi}{5}$	rad	initial orientation of object II
$\dot{\alpha}^{II}(0), \dot{\beta}^{II}(0), \dot{\gamma}^{II}(0)$	$\pi, 0, 0$	rad/s	initial angular velocity of object II

[21] J. Wittenburg, Dynamics of Multibody Systems, 2nd Edition, Springer-Verlag Berlin, 2008. doi:10.1007/978-3-540-73914-2.
[22] P. A. Cundall, O. D. L. Strack, A discrete numerical model for granular assemblies, Géotechnique 29 (1) (1979) 47–65. doi:10.1680/geot.1979.29.1.47.
[23] E. G. Gilbert, D. W. Johnson, S. S. Keerthi, A fast procedure for computing the distance between complex objects in three-dimensional space, IEEE J. Robotic. Autom. 4 (2) (1988) 193–203. doi:10.1109/56.2083.
[24] B. Mirtich, V-Clip: Fast and robust polyhedral collision detection, ACM T. Graphic. 17 (3) (1998) 177–208. doi:10.1145/285857.285860.
[25] G. van den Bergen, Efficient collision detection of complex deformable models using AABB trees, J. Graphics Tools 2 (4) (1997) 1–13. doi:10.1080/10867651.1997.10487480.
[26] S. Redon, A. Kheddar, S. Coquillart, An algebraic solution to the problem of collision detection for rigid polyhedral objects, in: IEEE Int. Conf. Robot., Vol. 4, 2000, pp. 3733–3738. doi:10.1109/ROBOT.2000.845313.
[27] G. van den Bergen, Proximity Queries and Penetration Depth Computation on 3D Game Objects, in: Game Developers Conference, 2001. URL graphics.stanford.edu/courses/cs468-01-fall/Papers/van-den-bergen.pdf
[28] A. Pournaras, F. Karaoulanis, S. Natsiavas, Dynamics of mechanical systems involving impact and friction using an efficient contact detection algorithm, Int. J. Nonlin. Mech. 94 (2017) 309–322. doi:10.1016/j.ijnonlinmec.2016.08.007.
[29] P. M. Hubbard, Approximating polyhedra with spheres for time-critical collision detection, ACM T. Graphic. 15 (3) (1996) 179–210. doi:10.1145/231731.231732.
[30] J. Ambrósio, Selected Challenges in Realistic Multibody Modeling of Machines and Vehicles, in: C. J. Zahariev E. (Ed.), IUTAM Symposium on Intelligent Multibody Systems – Dynamics, Control, Simulation, Vol. 33 of IUTAM Bookseries, Springer, Cham, 2019, pp. 1–39. doi:10.1007/978-3-030-00527-6_1.
[31] M. Machado, P. Flores, J. Ambrósio, A Lookup-Table-Based Approach for Spatial Analysis of Contact Problems, J. Comput. Nonlinear Dyn. 9 (4) (2014) 041010. doi:10.1115/1.4026894.
[32] J. F. Peters, M. A. Hopkins, R. Kala, R. E. Wahl, A poly-ellipsoid particle for non-spherical discrete element method, Eng. Computation. 26 (6) (2009) 645–657. doi:10.1108/02644400910975441.
[33] S. Zhao, J. Zhao, A poly-superellipsoid-based approach on particle morphology for DEM modeling of granular media, Int. J. Numer. Anal. Met. 43 (13) (2019) 2147–2169. doi:10.1002/nag.2951.
[34] X. Zheng, W. Iglesias, P. Palffy-Muhoray, Distance of closest approach of two arbitrary hard ellipsoids, Phys. Rev. E 79 (5) (2009) 057702. doi:10.1103/PhysRevE.79.057702.
[35] X. Lin, T. Ng, Contact detection algorithms for three-dimensional ellipsoids in discrete element modelling, Int. J. Numer. Anal. Meth. Geomech. 19 (9) (1995) 653–659. doi:10.1002/nag.1610190905.
[36] A. Donev, F. H. Stillinger, P. M. Chaikin, S. Torquato, Unusually Dense Crystal Packings of Ellipsoids, Phys. Rev. Lett. 92 (2004) 255506. doi:10.1103/PhysRevLett.92.255506.
[37] B. Brogliato, Nonsmooth Mechanics, 2nd Edition, Communications and Control Engineering, Springer, London, 1999. doi:10.1007/978-1-4471-0557-2.
[38] H. Hertz, Über die Berührung fester elastischer Körper, J. reine angew. Math. 92 (1882) 156–171. doi:10.1515/crll.1882.92.156.
[39] K. L. Johnson, Contact Mechanics, Cambridge University Press, Cambridge, 1985. doi:10.1017/cbo9781139171731.
[40] K. H. Hunt, F. R. E. Crossley, Coefficient of Restitution Interpreted as Damping in Vibroimpact, J. Appl. Mech. 42 (2) (1975) 440–445. doi:10.1115/1.3423596.
[41] P. Flores, M. Machado, M. T. Silva, J. M. Martins, On the continuous contact force models for soft materials in multibody dynamics, Multibody System Dynamics 25 (3) (2010) 357–375. doi:10.1007/s11044-010-9237-4.
[42] M. Machado, P. Moreira, P. Flores, H. M. Lankarani, Compliant contact force models in multibody dynamics: Evolution of the Hertz contact theory, Mech. Mach. Theory 53 (2012) 99–121. doi:10.1016/j.mechmachtheory.2012.02.010.
[43] J. Alves, N. Peixinho, M. T. da Silva, P. Flores, H. M. Lankarani, A comparative study of the viscoelastic constitutive models for frictionless contact interfaces in solids, Mech. Mach. Theory 85 (2015) 172–188. doi:10.1016/j.mechmachtheory.2014.11.020.
[44] Y. Shen, D. Xiang, X. Wang, L. Jiang, Y. Wei, A contact force model considering constant external forces for impact analysis in multibody dynamics, Multibody Syst. Dyn. 44 (4) (2018) 397–419. doi:10.1007/s11044-018-09638-0.
[45] A. S. Carvalho, J. M. Martins, Exact restitution and generalizations for the Hunt–Crossley contact model, Mech. Mach. Theory 139 (2019) 174–194. doi:10.1016/j.mechmachtheory.2019.03.028.
[46] J. Awrejcewicz, G. Kudra, Rolling resistance modelling in the Celtic stone dynamics, Multibody Syst. Dyn. 45 (2) (2019) 155–167. doi:10.1007/s11044-018-9624-9.
[47] J. Ma, G. Chen, L. Ji, L. Qian, S. Dong, A general methodology to establish the contact force model for complex contacting surfaces, Mech. Syst. Sig. Process. 140 (2020) 106678. doi:10.1016/j.ymssp.2020.106678.
[48] K. Kildashti, K. Dong, B. Samali, An accurate geometric contact force model for super-quadric particles, Comput. Methods Appl. Mech. Eng. 360 (2020) 112774. doi:10.1016/j.cma.2019.112774.
[49] R. D. Mindlin, Compliance of elastic bodies in contact, J. Appl. Mech. 16 (1949) 259–268.
[50] R. D. Mindlin, H. Deresiewicz, Elastic spheres in contact under varying oblique forces, Trans. ASME, J. Appl. Mech. 20 (1953) 327–344.
[51] E. Pennestrì, V. Rossi, P. Salvini, P. P. Valentini, Review and comparison of dry friction force models, Nonlinear Dyn. 83 (4) (2015) 1785–1801. doi:10.1007/s11071-015-2485-3.
[52] F. Marques, P. Flores, J. C. P. Claro, H. M. Lankarani, A survey and comparison of several friction force models for dynamic analysis of multibody mechanical systems, Nonlinear Dyn. 86 (3) (2016) 1407–1443. doi:10.1007/s11071-016-2999-3.
[53] F. Marques, P. Flores, J. C. P. Claro, H. M. Lankarani, Modeling and analysis of friction including rolling effects in multibody dynamics: a review, Multibody Syst. Dyn. 45 (2) (2019) 223–244. doi:10.1007/s11044-018-09640-6.
[54] U. J. Römer, A. Fidlin, W. Seemann, Explicit analytical solutions for two-dimensional contact detection problems between almost arbitrary geometries and straight or circular counterparts, Mech. Mach. Theory 128 (2018) 205–224. doi:10.1016/j.mechmachtheory.2018.05.018.
[55] W. Zhong, A. Yu, X. Liu, Z. Tong, H. Zhang, DEM/CFD-DEM modelling of non-spherical particulate systems: theoretical developments and

applications, Powder Technol. 302 (2016) 108–152. doi:10.1016/j.powtec.2016.07.010.
[56] J. A. Corrales, F. A. Candelas, F. Torres, Safe human–robot interaction based on dynamic sphere-swept line bounding volumes, Robot. Cim-Int. Manuf. 27 (1) (2011) 177–185. doi:10.1016/j.rcim.2010.07.005.
[57] L. Ren, D. Howard, L. Ren, C. Nester, L. Tian, A generic analytical foot rollover model for predicting translational ankle kinematics in gait simulation studies, J. Biomech. 43 (2) (2010) 194–202. doi:10.1016/j.jbiomech.2009.09.027.
[58] D. S. Lopes, R. R. Neptune, J. A. Ambrósio, M. T. Silva, A superellipsoid-plane model for simulating foot-ground contact during human gait, Comp. Meth. Biomech. Biomed. Eng. 19 (9) (2016) 954–963. doi:10.1080/10255842.2015.1081181.
[59] B. A. Barsky, T. D. DeRose, Geometric continuity of parametric curves: three equivalent characterizations, IEEE Comput. Graph. 9 (6) (1989) 60–69. doi:10.1109/38.41470.
[60] B. Pham, Offset curves and surfaces: a brief survey, Comput. Aided Design 24 (4) (1992) 223–229. doi:10.1016/0010-4485(92)90059-J.
[61] T. Maekawa, An overview of offset curves and surfaces, Comput. Aided Design 31 (3) (1999) 165–173. doi:10.1016/S0010-4485(99)00013-5.
[62] R. T. Farouki, Pythagorean-Hodograph Curves: Algebra and Geometry Inseparable, Vol. 1 of Geometry and Computing, Springer Berlin Heidelberg, 2008. doi:10.1007/978-3-540-73398-0.
[63] D. J. Struik, Lectures on Classical Differential Geometry, 2nd Edition, Addison-Wesley, Reading Mass., 1961, 1–104.
[64] D. E. Stewart, Rigid-body dynamics with friction and impact, SIAM Review 42 (1) (2000) 3–39. doi:10.1137/S0036144599360110.
[65] A. E. Martin, R. D. Gregg, Stable, Robust Hybrid Zero Dynamics Control of Powered Lower-Limb Prostheses, IEEE T. Automat. Contr. 62 (8) (2017) 3930–3942. doi:10.1109/tac.2017.2648040.
[66] M. Millard, K. Mombaur, A Quick Turn of Foot: Rigid Foot-Ground Contact Models for Human Motion Prediction, Front. Neurorobotics 13 (2019) 62. doi:10.3389/fnbot.2019.00062.
[67] M. S. Shourijeh, J. McPhee, Foot–ground contact modeling within human gait simulations: from Kelvin–Voigt to hyper-volumetric models, Multibody Syst. Dyn. 35 (4) (2015) 393–407. doi:10.1007/s11044-015-9467-6.
[68] P. Brown, J. McPhee, A 3D ellipsoidal volumetric foot–ground contact model for forward dynamics, Multibody Syst. Dyn. 42 (4) (2017) 447–467. doi:10.1007/s11044-017-9605-4.